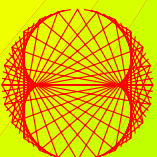


ISSUE 2007

PROGRESS IN PHYSICS

VOLUME 1



ISSN 1555-5534

PROGRESS IN PHYSICS

A quarterly issue scientific journal, registered with the Library of Congress (DC, USA). This journal is peer reviewed and included in the abstracting and indexing coverage of: Mathematical Reviews and MathSciNet (AMS, USA), DOAJ of Lund University (Sweden), Zentralblatt MATH (Germany), Referativnyi Zhurnal VINITI (Russia), etc.

Electronic version of this journal:
<http://www.ptep-online.com>
http://www.geocities.com/ptep_online

To order printed issues of this journal, contact the Editor-in-Chief.

Chief Editor
Dmitri Rabounski
rabounski@ptep-online.com
Associate Editors
Prof. Florentin Smarandache
smarandache@ptep-online.com
Dr. Larissa Borissova
borissova@ptep-online.com
Stephen J. Crothers
crothers@ptep-online.com

Department of Mathematics, University of New Mexico, 200 College Road, Gallup, NM 87301, USA

Copyright © *Progress in Physics*, 2007

All rights reserved. Any part of *Progress in Physics* howsoever used in other publications must include an appropriate citation of this journal.

Authors of articles published in *Progress in Physics* retain their rights to use their own articles in any other publications and in any way they see fit.

This journal is powered by L^AT_EX

A variety of books can be downloaded free from the Digital Library of Science:
<http://www.gallup.unm.edu/~smarandache>

ISSN: 1555-5534 (print)
ISSN: 1555-5615 (online)

Standard Address Number: 297-5092
Printed in the United States of America

JANUARY 2007

VOLUME 1

CONTENTS

P.-M. Robitaille WMAP: A Radiological Analysis	3
P.-M. Robitaille On the Origins of the CMB: Insight from the COBE, WMAP, and Relikt-1 Satellites	19
D. Rabounski The Relativistic Effect of the Deviation between the CMB Temperatures Obtained by the COBE Satellite	24
B. Lehnert Momentum of the Pure Radiation Field	27
S. Marinov New Measurement of the Earth's Absolute Velocity with the Help of the "Coupled Shutters" Experiment	31
A. Khazan Upper Limit in the Periodic Table of Elements	38
F. Smarandache and V. Christianto Less Mundane Explanation of Pioneer Anomaly from Q-Relativity.....	42
W. Tawfik and A. Askar Study of the Matrix Effect on the Plasma Characterization of Heavy Elements in Soil Sediments using LIBS with a Portable Echelle Spectrometer	46
C.E. Navia, C.R.A. Augusto, D.F. Franceschini, M.B. Robba and K.H. Tsui Search for Anisotropic Light Propagation as a Function of Laser Beam Alignment Relative to the Earth's Velocity Vector	53
F. Potter and H.G. Preston Quantization State of Baryonic Mass in Clusters of Galaxies	61
V.A. Panchelyuga, V.A. Kolombet, M.S. Panchelyuga and S.E. Shnoll Experimental Investigations of the Existence of a Local-Time Effect on the Laboratory Scale and the Heterogeneity of Space-Time	64
P.-M. Robitaille A High Temperature Liquid Plasma Model of the Sun	70

Information for Authors and Subscribers

Progress in Physics has been created for publications on advanced studies in theoretical and experimental physics, including related themes from mathematics. All submitted papers should be professional, in good English, containing a brief review of a problem and obtained results.

All submissions should be designed in L^AT_EX format using *Progress in Physics* template. This template can be downloaded from *Progress in Physics* home page <http://www.ptep-online.com>. Abstract and the necessary information about author(s) should be included into the papers. To submit a paper, mail the file(s) to Chief Editor.

All submitted papers should be as brief as possible. Commencing 1st January 2006 we accept brief papers, no larger than 8 typeset journal pages. Short articles are preferable. Papers larger than 8 pages can be considered in exceptional cases (such as discoveries, etc.) to the section *Special Reports* intended for such publications in the journal.

All that has been accepted for the online issue of *Progress in Physics* is printed in the paper version of the journal. To order printed issues, contact Chief Editor.

This journal is non-commercial, academic edition. It is printed from private donations.

SPECIAL REPORT**WMAP: A Radiological Analysis**

Pierre-Marie Robitaille

Dept. of Radiology, The Ohio State University, 130 Means Hall, 1654 Upham Drive, Columbus, Ohio 43210, USA

E-mail: robitaille.1@osu.edu

In this work, results obtained by the WMAP satellite are analyzed by invoking established practices for signal acquisition and processing in nuclear magnetic resonance (NMR) and magnetic resonance imaging (MRI). Dynamic range, image reconstruction, signal to noise, resolution, contrast, and reproducibility are specifically discussed. WMAP images do not meet accepted standards in medical imaging research. WMAP images are obtained by attempting to remove a galactic foreground contamination which is 1,000 times more intense than the desired signal. Unlike water suppression in biological NMR, this is accomplished without the ability to affect the signal at the source and without *a priori* knowledge. Resulting WMAP images have an exceedingly low signal to noise (maximum 1–2) and are heavily governed by data processing. Final WMAP internal linear combination (ILC) images are made from 12 section images. Each of these, in turn, is processed using a separate linear combination of data. The WMAP team extracts cosmological implications from their data, while ignoring that the ILC coefficients do not remain constant from year to year. In contrast to standard practices in medicine, difference images utilized to test reproducibility are presented at substantially reduced resolution. ILC images are not presented for year two and three. Rather, year-1 data is signal averaged in a combined 3-year data set. Proper tests of reproducibility require viewing separate yearly ILC images. Fluctuations in the WMAP images arise from the inability to remove the galactic foreground, and in the significant yearly variations in the foreground itself. Variations in the map outside the galactic plane are significant, preventing any cosmological analysis due to yearly changes. This occurs despite the masking of more than 300 image locations. It will be advanced that any “signal” observed by WMAP is the result of foreground effects, not only from our galaxy, but indeed yearly variations from every galaxy in the Universe. Contrary to published analysis, the argument suggests there are only questionable findings in the anisotropy images, other than those related to image processing, yearly galactic variability, and point sources. Concerns are also raised relative to the validity of assigning brightness temperatures in this setting.

1 Introduction

The WMAP satellite [1] was launched with the intent of measuring the microwave signals present in space. It is widely held that these signals are anisotropic and relay information relative to the creation and formation of the early Universe [1–27]. WMAP has been hailed as providing some of the most important findings in science [2]. Reports by Spergel et. al. [15] and Bennett et. al. [7] are highly cited [28]. The ensemble of WMAP publications [3–26] appears to constitute a phenomenal assortment of data. WMAP is being praised both for its precision and the insight it provides into the earliest stages of the formation of the Universe [1, 2]. NASA and the WMAP team of scientists, representing the premier academic institutions [1], have made numerous claims, most notably stating that their data enables them to visualize what happened in the first trillionth of a second after the Big Bang [27]. From data with a signal to noise just beyond 1, a number of constants is provided relative to the age of the Universe (13.7 ± 0.2 Gyr), the amount of dark

energy ($\sim 73\%$), dark matter ($\sim 22\%$), and baryons density or “real” matter ($\sim 4\%$) [7, 25]. It is surmised that “decoupling” occurred just after the Big Bang (379 ± 8 kyr) at a redshift of 1089 ± 1 . The thickness of the decoupling surface is given as 195 ± 2 , and the total mass-energy in the Universe (1.02 ± 0.02) is also amongst the constants [7, 25].

WMAP does not measure the absolute intensity of any given microwave signal. Rather, it is equipped with antennae whose difference is constantly recorded. Thus, all WMAP data represent difference data. The satellite is positioned at the second Lagrange point of the Sun-Earth system, L2, approximately 1.5 million km from Earth. At this position, the Earth continually shields WMAP from the Sun, as they each complete their orbits. The first year of data collection extended from 10 August 2001 – 9 August 2002, with data release in March 2003. A complete 3-year average data set, spanning 10 August 2001 – 9 August 2004, was released in March 2006.

The WMAP satellite acquires signals at five observational frequencies: 23, 33, 41, 61, and 94 GHz. These are also

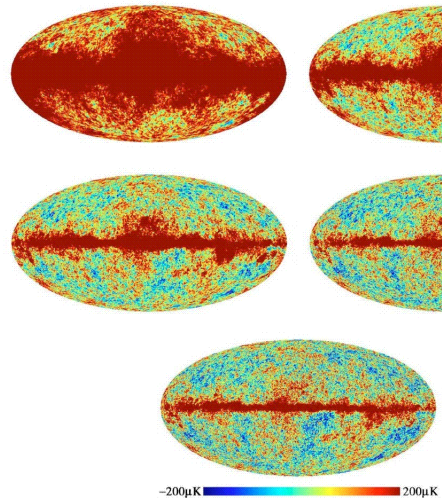


Fig. 1: The five frequency bands observed by the WMAP satellite. Images correspond to 23 GHz (K band, upper left), 33 GHz (Ka band, upper right), 41 GHz (Q band, middle left), 61 GHz (V band, middle right), and 94 GHz (W band, bottom). Reprinted portion of Figure 2 with permission from Tegmark M., de Oliveira-Costa A., Hamilton A.J.S. A high resolution foreground cleaned CMB map from WMAP. *Phys. Rev. D*, 2003, v. 68(12), 123523; <http://link.aps.org/abstract/PRD/v68/e123523>. Copyright (2003) by the American Physical Society.

known as the K, Ka, Q, V, and W bands. Images generated at these bands are displayed in Figure 1. Final anisotropy maps are prepared by combining the signals represented in Figure 1 with particular weighting at 61 GHz. Maps for each year are prepared individually and then combined “for a number of reasons” [23]. Extensive image processing is applied prior to generating the final anisotropy map (see Figure 2). The noise level in the data sets depends on the number of observations at each point. The major hurdle for WMAP is the presence of the strong foreground signal from our galaxy. In a sense, the WMAP team is trying to “look through” the galaxy, as it peers into the Universe.

In recent years, WMAP results have been widely disseminated both in the scientific literature and the popular press. Nonetheless, there are sufficient questions relative to the manner in which the WMAP data is processed and analyzed, to call for careful scrutiny by members of the imaging community. The implications of WMAP are not only financial and scientific but, indeed, have the potential to impact the course of science and human reason for many generations. As a result, images which are the basis of such specific scientific claims must adhere to standard practices in imaging science. Consequently, and given the precision of the constants provided by WMAP, it is appropriate to review the underlying images and subject them to the standards applied in radiological image analysis. These include most notably signal to noise, resolution, reproducibility, and contrast. These four characteristics represent universally accepted

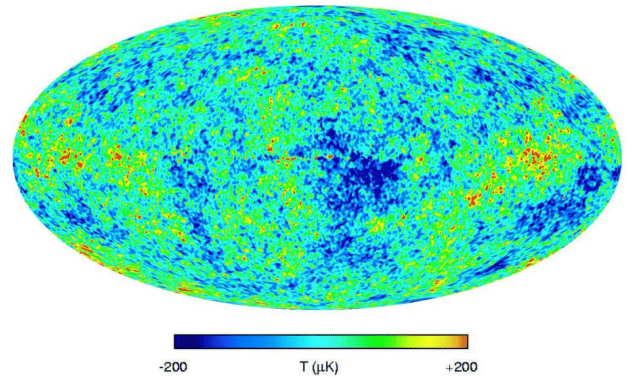


Fig. 2: Cleaned internal linear combination (ILC) map produced by the WMAP team [7]. This image corresponds to Figure 11 in Bennett et. al. [7]. Reproduced with permission of the AAS. Image provided courtesy of the NASA/WMAP team.

measures of image quality. However, before embarking on this exercise, it is important to address dynamic range and the removal of the galactic foreground. In addition, it is useful to review the procedure which the WMAP team employs in image reconstruction.

2 Image analysis

2.1 Dynamic range and the removal of the Galactic foreground

The WMAP satellite acquires its data in five frequency bands. Five images obtained at these bands (K, Ka, Q, V, and W) are displayed in Figure 1 [29]. The galactic foreground dominates this entire series of images. The foreground is seen as a bright red signal across the central portion of each frequency map. Indeed, the center of the galactic foreground, observed by WMAP, exceeds the desired anisotropic signal in brightness by a factor of $\sim 1,000$ [11]. Therefore, the WMAP team is attempting to visualize extremely weak anisotropy in the presence of a much more powerful contaminating signal. This becomes a dynamic range issue analogous to water suppression in biological proton nuclear magnetic resonance (NMR).

Water suppression is an important technique in proton NMR, since most compounds of biochemical interest are typically found dissolved in the aqueous cytosol of the cell. This includes a wide array of proteins, signal messengers, precursors, and metabolic intermediates. Water is roughly 110 molar in protons, whereas the signal of interest to the biochemist might be 1–100 millimolar. In the best case scenario, biological proton NMR, like WMAP, presents a $\sim 1,000$ fold problem in signal removal. In the worst case, factors of 100,000 or more must be achieved. Extensive experience in biological NMR obtained throughout the world has revealed that it is impossible to remove a contaminating signal on these orders of magnitude without either (1) ability

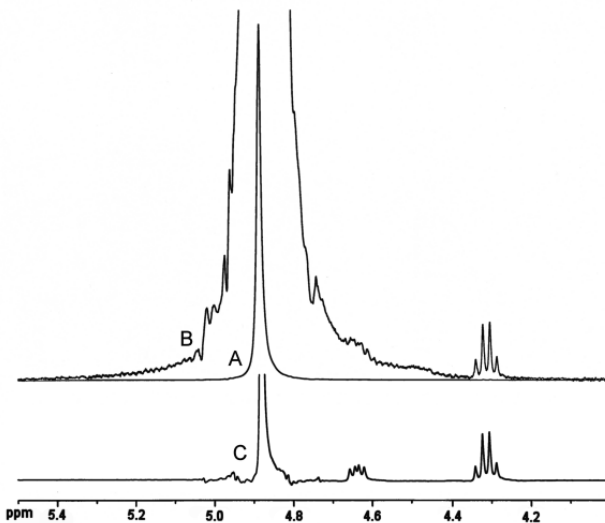


Fig. 3: Proton nuclear magnetic resonance (NMR) spectra acquired from a 0.1 M solution of 0.1 M N-benzoyl-L-arginine ethyl ester hydrochloride in water (A, B). The spectrum is shown in full scale (A). In (B) the vertical axis has been expanded by a factor of 100, such that the resonance lines from the N-benzoyl-L-arginine ethyl ester can be visualized. A ^1H -NMR spectrum acquired from 0.1 M N-benzoyl-L-arginine ethyl ester hydrochloride in deuterium oxide (D_2O) is also displayed (C). Spectra display only the central region of interest (4.0–5.5 ppm). Acquisition parameters are as follows: frequency of observation 400.1324008 MHz, sweep width 32,768 Hz, receiver gain 20, and repetition time 5 seconds. The sample dissolved in D_2O (C) was acquired first using a single acquisition and a 90 degree nutation. A field lock was obtained on the solvent. This was used in adjusting the field homogeneity for both samples. For (A) and (B), 20 acquisitions were utilized to enable phase cycling of the transmitter and receiver. In this case, the nutation angle had to be much less than 90 degrees in order not to destroy the preamplifier. A field lock could not be achieved since D_2O was not present in the sample. These slight differences in acquisition parameters and experimental conditions make no difference to the discussion in the text relative to problems of dynamic range.

to affect the signal at the source, and/or (2) *a priori* knowledge. Unfortunately for WMAP, neither of these conditions can be met in astrophysics.

In NMR, ability to effect signal at the source requires direct manipulation of the sample, either biochemically through substitution, or physically, through specialized spin excitation. Biochemical substitution involves the removal of the protons associated with water, using deuterium oxide (D_2O) as an alternative solvent [30]. Often, the sample is lyophilized [31]. That is, it is frozen and placed under vacuum so that all of the water can be removed through sublimation. The solvent is then replaced by the addition of D_2O . This process can be repeated several times to remove most of the exchangeable protons contained in the sample. The protons are hence replaced by deuterium, which is no longer detectable at the frequency utilized to acquire the

desired proton NMR spectrum. Thus, in order to achieve a factor of 1,000 in suppression, the biochemist, in the laboratory, often invokes a rather dramatic modification of the sample at the source.

In Figure 3, a series of ^1H -NMR spectra is presented. Figure 3A corresponds to a mixture of 0.1 M N-benzoyl-L-arginine ethyl ester hydrochloride in water. Since water is 110 M in protons, this solution constitutes roughly a 1,000 fold excess of water protons versus sample protons. Interestingly, the only signal which can be detected in Figure 3A is that of water at 4.88 ppm. The multiple resonances from the N-benzoyl-L-arginine ethyl ester hydrochloride have about the same intensity as found in the line width. In Figure 3B, the same spectrum is reproduced but, this time, the vertical scale has been expanded 100 times. Now, the resonances from the sample are readily observed. The ratio of the water resonance in Figure 3A or B to the quartet at 4.3 ppm is 670. Note, however, that a doublet pair, located at \sim 4.63 ppm (Figure 3B) is being distorted by the intense resonance line from water. This is easy to assess by examining Figure 3C, wherein a solution of 0.1 M N-benzoyl-L-arginine ethyl ester hydrochloride was reconstituted in 99.8% D_2O . In the D_2O spectrum (C), the ratio of the water resonance to the quartet at 4.3 ppm is 21. In this case, the water line is greatly attenuated, since most of the water protons have been replaced with deuterium. Indeed, substitution of D_2O for water (C) results in a 30 fold drop in the intensity of the water line. With this sample, all of the resonances from the N-benzoyl-L-arginine ethyl ester hydrochloride in the vicinity of the water resonance can be visualized, including the doublet pair, at 4.63 ppm. From this information, the ratio of the water to the doublet pair at 4.63 ppm is \sim 1,500.

Through Figure 3, it is easy to envision the tremendous challenge involved in removing a contaminating signal which dominates the species of interest by \sim 1,000 fold. In Figure 3B, it is readily apparent that the doublet pair at 4.63 ppm is being distorted by the water line. Consequently, the presence of the intense water resonance affects spins which are adjacent, not only co-resonant. The situation is actually much worse for WMAP as the satellite is attempting to visualize signals contained at the same frequency of observation as the galactic foreground signals. In a sense, the WMAP team is trying to see signals directly beneath the water line, not adjacent to it. To further aggravate the situation, the WMAP team is dealing with extremely weak signals, on the same order of magnitude as the noise floor (see below). Note that the obscured resonances at \sim 4.63 ppm in the water spectrum would still have a signal to noise of \sim 5:1, if the water line had not contaminated this region. This can be gathered by comparing Figures 3B and 3C. For WMAP, the signal to noise is less than 2:1, and the signal of interest is located at the same frequency of the contamination.

Relative to dynamic range and removal of a contaminating water signal in NMR however, an alternative to replacing

water with deuterium oxide exists. In fact, it is possible to utilize specialized spin excitation techniques which either exploit the position of the water line in the spectrum [32–36] or invoke gradient and/or multiple quantum selection [37–39]. Indeed, the approaches to water suppression and dynamic range problems in NMR are so numerous that only a few methods need be discussed to adequately provide experimental insight relative to WMAP.

If the experimentalist is not concerned with signals lying at the same frequency of the water resonance, it is sometimes possible to excite the spins in such a manner that the protons co-resonating with water are nulled and other regions of the spectrum are detected [32–36]. This approach is adopted by methods such as presaturation [32], jump-return [33], and other binomial sequences for spin excitation [34–36]. In each case, the spectral region near the water resonance is sacrificed in order to permit the detection of adjacent frequencies. Despite the best efforts, these methods depend on the existence of very narrow water line widths. Water suppression with these methods tends to be limited to factors of ~ 100 . The situation *in-vivo* might be slightly worse given the wider line widths typically observed in this setting. Despite this apparent success, these methods fail to preserve the signal lying “beneath” the water resonance. Such information is lost.

In certain instances, it is also possible to excite the spectrum by applying specialized gradient-based methods and quantum selection for spin excitation. In so doing, advantage is made of the unique quantum environment of the spins. These methods have the advantage that spins, which co-resonate with water, are not lost. As such, water suppression can be achieved while losing little or no chemical information. The most powerful of these methods often have recourse to gradient fields, in addition to RF fields, during spin excitation [37–39]. These approaches have been particularly important in the study of proteins in solution [39]. Using quantum selection, it is not unreasonable to expect spin excitation with factors of 1,000–10,000 or more in water suppression.

Methods which rely on coherence pathway selection, or hetero-nuclear multiple quantum selection, constitute important advances to NMR spectroscopy in general, and protein NMR in particular [39]. In the absence of these methods, modern aqueous proton NMR would be impossible. In fact, over the course of the last 50 years, it has been amply demonstrated that it is simply not possible to acquire any information of interest, near the water resonance in biological NMR, by data processing a spectrum obtained from an aqueous sample without *a priori* water suppression. Yet, the WMAP map team attempts the analogous data processing feat, in trying to remove the foreground galactic signal.

Unlike the situation in astrophysics, it is possible to address dynamic range issues in NMR, since the spectroscopist literally holds the sample in his hands. The required signals

can be selected by directly controlling spin excitation and, therefore, the received signal. Water suppression is addressed prior to signal acquisition, by carefully avoiding the excitation of spins associated with water. The analogous scenario is not possible in astrophysics.

To a smaller extent, water suppression in biological NMR could perhaps be achieved with *a priori* knowledge (i.e. a perfect knowledge of line shapes, intensity, and position). However, such an approach has not yet been successfully implemented in the laboratory. As a result, *a priori* knowledge in NMR is theoretically interesting, but practically unfeasible. This is an even greater limitation in astrophysics where very limited knowledge of the sample exists. The vast experience of NMR scientists demonstrates that the removal of a strong contaminating signal, for the detection of a much weaker underlying signal, is impossible without affecting the signals at the source. Biological NMR has been in existence for over half a century. During most of this time, achieving a factor of 1,000 in signal removal was considered a dramatic achievement, even when combining spin excitation methods with lyophilization. Only in the past 15 years have methods improved, and this solely as a result of gradient-based or multiple-quantum techniques, which provide even more powerful spin selection during excitation [39]. Signal suppression, by a factor of 100, or more, while still viewing the underlying signal, depends on the ability to control the source. This has been verified in numerous laboratories where the sample is known and where the correct answer can be readily ascertained. As such, it is impossible for the WMAP team to remove the galactic foreground given the dynamic range situation between the contaminant and the signal of interest. Attempts to the contrary are futile, as indicated by the need to segment the final images into 12 sections, and alter, from section to section, the linear combination of data, as will be discussed below.

The galactic problem alone is sufficient to bring into question any conclusion relative to anisotropy from both WMAP and COBE. Nonetheless, additional insight can be gained by examining image reconstruction.

2.2 ILC image reconstruction

2.2.1 Combining section images

Despite this discussion relative to NMR, the WMAP team claims that removal of the galactic foreground is possible and therefore proceeds to ILC image generation. As mentioned above, the WMAP satellite obtains its data in five frequency bands (23, 33, 41, 61, and 94 GHz). In order to achieve galactic foreground removal, the WMAP team utilizes a linear combination of data in these bands, essentially adding and subtracting data until a null point is reached. In doing so, the WMAP team is invoking *a priori* knowledge which cannot be confirmed experimentally. Thus, the WMAP team makes the assumption that foreground contamination

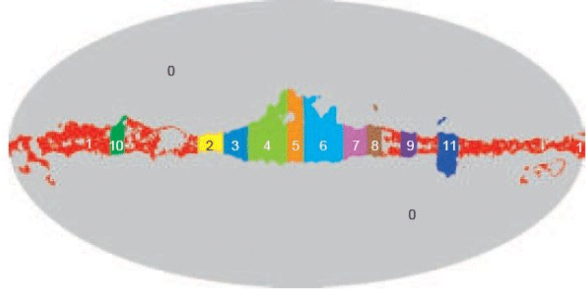


Fig. 4: Illustration of the 12 regions used to generate the ILC maps for year 3 average data. This image corresponds to the upper portion of Figure 8 in Hinshaw et. al. [23]. Reproduced with permission of the AAS. Image provided courtesy of the NASA/WMAP team.

is frequency dependent, while the anisotropy is independent of frequency. This approach, however, is completely unsupported by the experimental data, as will be discussed further below.

Furthermore, galactic foreground removal cannot be achieved with a single linear combination of data. Rather, WMAP achieves its final maps by first generating separately processed section images. Eleven of these regions lie directly in the galactic plane, as shown in Figure 4. Each section is processed individually. The twelve processed section images are then combined and smoothed to generate the final ILC maps.

The WMAP team invokes completely different linear combinations of data to process adjacent regions of the galactic plane. In medical imaging, there is seldom, if ever, the need to process final images in sections. Given this fact, note the processing applied to generate regions 4 and 5 in the 3-year average data (see Figure 4). The coefficients, for section 4, correspond to -0.0781 , 0.0816 , -0.3991 , 0.9667 , and 0.4289 for the K, Ka, Q, V, and W bands, respectively [23]. In sharp contrast, the coefficients for section 5 correspond to 0.1839 , -0.7466 , -0.3923 , 2.4184 , and -0.4635 , for these same bands [23]. The WMAP team alters the ILC weights by regions, used in galactic signal removal, by more than a factor of 100% for the fourth coefficient, despite the adjacent locations of these sections. The same problem exists for several other adjacent sections in the galactic plane [23]. The sole driving force for altering the weight of these coefficients lies in the need to zero the foreground. The selection of individual coefficients is without scientific basis, with the only apparent goal being the attainment of a null point. The full list of ILC coefficients adopted by the WMAP team are reproduced in Table I (reprint of Table 5 in reference [23]). Analysis of this table reveals the tremendous coefficient variability used, from section to section, for zeroing the galactic foreground.

In generating the ILC maps, the WMAP team chose to primarily weigh the V-band. As a result, the coefficients selected tend to reflect this emphasis. However, there is no

Region	K-band	Ka-band	Q-band	V-band	W-band
0	0.1559	-0.8880	0.0297	2.0446	-0.3423
1	-0.0862	-0.4737	0.7809	0.7631	0.0159
2	0.0358	-0.4543	-0.1173	1.7245	-0.1887
3	-0.0807	0.0230	-0.3483	1.3943	0.0118
4	-0.0781	0.0816	-0.3991	0.9667	0.4289
5	0.1839	-0.7466	-0.3923	2.4184	-0.4635
6	-0.0910	0.1644	-0.4983	0.9821	0.4428
7	0.0718	-0.4792	-0.2503	1.9406	-0.2829
8	0.1829	-0.5618	-0.8002	2.8464	-0.6674
9	-0.0250	-0.3195	-0.0728	1.4570	-0.0397
10	0.1740	-0.9532	0.0073	2.7037	-0.9318
11	0.2412	-1.0328	-0.2142	2.5579	-0.5521

Table 1: ILC weights by regions. ILC coefficients used in the analysis of 3-year data by the WMAP team. This table corresponds to Table 5 in Hinshaw et. al. [23]. Utilized courtesy of the NASA/WMAP team.

a priori reason why the weighting could not have emphasized the Q band, for instance. This is especially true since anisotropy is advanced as being frequency independent. Indeed, it is interesting that the Q and W bands have coefficients on the order of -0.4 , while lying in proximity to the V band which is given a weight of 2.4 for region 5.

Nonetheless, the scientifically interesting region in the ILC map corresponds to section 0 (see Figure 4). Thus, problems in removing the galactic foreground could be tolerated, given that the WMAP team has no other alternative. It is the processing utilized for section 0 which is most important. This brings yet another complication. Completely different ILC maps of the Universe would be obtained, if the WMAP team had decided to emphasize a frequency other than the V band. In that case, an altered set of cosmological constants is very likely to be generated, simply as a result of data processing.

In removing the galactic foreground, the WMAP team has assumed that the anisotropy is frequency independent. In reality, it is already clear that an ILC map generated with weighting on the Q-band, for instance, will be dramatically different. The requirement that the signals of interest are frequency independent cannot be met, and has certainly never been proven.

In the first data release, the only real requirement for generating the ILC maps was that the coefficients sum to 1. As such, an infinite number of maps can be generated. There is no single map of the anisotropy, since all maps are equally valid, provided coefficients sum to 1. In this regard, alternative anisotropic maps have been presented [29]. Tegmark et. al. [29] generate a new anisotropy map by permitting

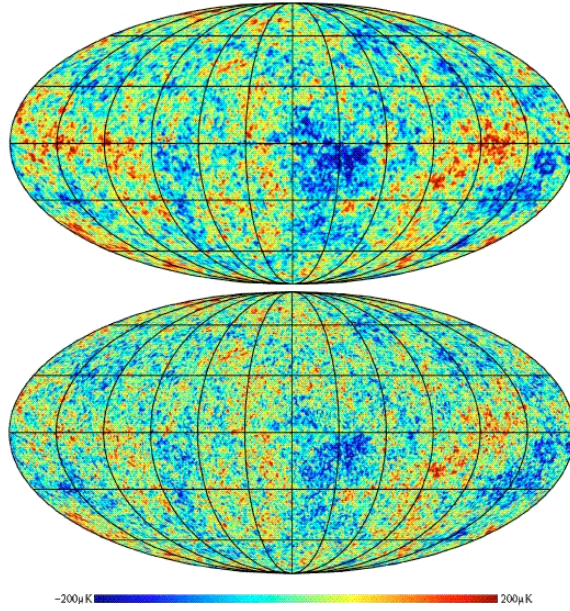


Fig. 5: Cleaned internal linear combination (ILC) anisotropy map produced by the WMAP team (top) and Wiener filtered anisotropy map (bottom) produced by Tegmark et. al. [29]. Reprinted portion of Figure 1 with permission from Tegmark M., de Oliveira-Costa A., Hamilton A.J.S. A high resolution foreground cleaned CMB Map from WMAP. *Phys. Rev. D*, 2003, v. 68(12), 123523; <http://link.aps.org/abstract/PRD/v68/e123523>. Copyright (2003) by the American Physical Society.

the coefficient weighting to depend both on angular scale and on distance to the galactic plane. This approach was substantially different from that implemented by the WMAP team and it reinforces the finding that no single anisotropy map exists. In Figure 5, it is apparent that the map generated by the WMAP team (top) does not agree with the map generated by Tegmark et. al. (bottom) [29].

An infinite number of maps can be generated from the 5 basis sets. There is no unique solution and therefore each map is indistinguishable from noise. There are no findings relative to anisotropy, since there are no features in the maps which could guide astrophysics relative to the true solution.

With the release of the 3-year data set however, the WMAP team claims that they can use mathematical methods to find the maximum likelihood sky map [23]. Unfortunately, there are no means to test the validity of the solution. In this regard, astrophysics is at a significant disadvantage relative to clinical MRI. Thus, the radiological scientist is guided by known anatomy, and by the results of all other imaging modalities focused on the same sample. This is not the case in astrophysics, since no single spectroscopic frequency holds an advantage over any other. There is no “known” signature to guide the choice of coefficients. A map might appear to be favored, however, devoid of secondary experimental verification, its legitimacy can never be established. Alternative methods could produce alternative maximum likeli-

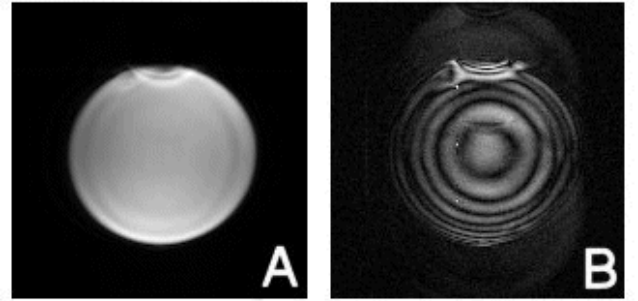


Fig. 6: Ultra High Field 8 Tesla MRI image of an 18 cm ball of mineral oil acquired using a 3-dimentional acquisition. A) Axial slice representing a region contained within the physical space occupied by the 18 cm mineral oil ball. (B) Axial slice through a region located outside the physical space occupied by the ball. Note that the image displayed in (B) should be entirely devoid of signal. The severe image processing artifacts contained in (B) are a manifestation that the processing of powerful signals can result in the generation of weak spurious ghost signals.

hood maps. Another level of testing is being added. Nonetheless, the conclusion remains that an infinite number of maps can be generated since, given sufficient resources, one can generate a number of maximal likelihood approaches with no clear way of excising the “true” solution. Therefore, any discussion relative to the cosmological significance of these results is premature.

2.2.2 Generation of spurious signals

Attempts to remove, by signal processing, a powerful galactic signal will invariably generate unwanted features in the maps, indistinguishable from real findings. The process of removing an intense signal can result in the unexpected creation of many spurious weak ghost signals, at any point in the image plane. Therefore, it is crucial that the signal to noise, in the final image or spectrum of interest, be significant.

In biological NMR, the post-water suppression spectrum typically has good signal to noise. It would not be unusual to achieve 1,000 fold suppression of the water signal and obtain a spectrum with a signal to noise well in excess of 10, or even 100, for the species of interest. This signal to noise is high enough to differentiate it from spurious ghost signals, generated either directly by suppression or through data processing.

In MRI, it is well established that the processing of large signals can lead to spurious signal ghosts throughout an image or a set of images. This is displayed in Figure 6. Figure 6A shows an MRI image of an 18 cm phantom sample containing mineral oil. This image is part of a much larger group of images obtained during a 3D test study. In Figure 6B, a series of signal rings are observed. These rings are spurious ghosts. They were produced by obtaining a 3-dimensional data set on an 18 cm ball containing mineral oil, using an 8 Tesla MRI scanner [40–42]. The signal is acquired

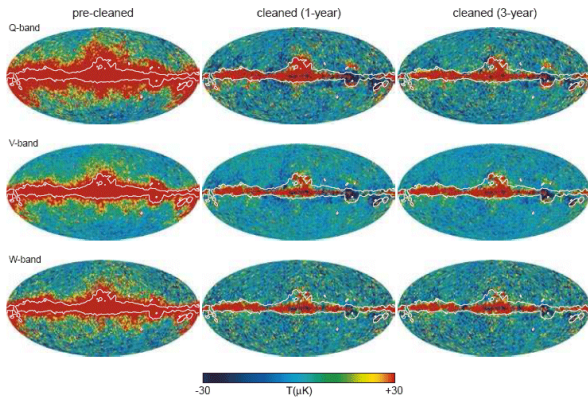


Fig. 7: Illustration of galactic foreground removal for year-1 and for the 3-year average. “Cleaning” is illustrated for the Q, V, and W bands. Similar data are not presented for the K and Ka bands [23]. This image corresponds to Figure 10 in Hinshaw et. al. [7]. Reproduced with permission of the AAS. Image provided courtesy of the NASA/WMAP team.

from the entire ball in the time domain and then Fourier transformed to achieve a set of images in the frequency domain [43]. *The image displayed in Figure 6B corresponds to an imaging slice which lies outside the actual physical space occupied by the ball.* Ideally, this image should be completely black. The spurious signal is a manifestation of a truncation artifact in Fourier transformation during data processing. There should be no signal in this image. However, for the sake of this discussion, it provides an excellent illustration of what can happen when powerful signals must be mathematically manipulated to generate final images.

While the WMAP team is not using simple Fourier transformation to process their images, this lesson nonetheless applies. When mathematically manipulating large signals, weak spurious signals can be created. This phenomenon is common to all image processing, and hence the importance of relatively strong signals of interest once the contaminating signal is removed. This is not the case for WMAP. The contaminating foreground is $\sim 1,000$ times the “signal” of interest. Yet, the final signal to noise is poor.

The WMAP team invokes the “cleaning” of its raw images acquired at the K, Ka, Q, V, and W bands prior to presenting the images for these bands [7]. The affect of “cleaning” is demonstrated in Figure 7. Note how the process of “cleaning” the images appears to remove the galactic foreground for the Q, V, and W bands. Interestingly, similar images are not being presented for cleaning the K and Ka bands. This is precisely because the galactic signal contamination is so significant for these two bands. Indeed, the WMAP team needs to present the data for the K and Ka bands in this same figure, in order to place the galactic signal contamination and the associated “cleaning” in proper perspective.

While the galactic center appears to affect only a central

region of the Q, V, and W bands in the cleaned image, the situation is more complex. In fact, it is impossible to discern if a given signal is truly independent of the galaxy at any location on the image. This is because the process of “cleaning” images, to remove powerful contaminating signals, is never clean. Mathematical manipulation of powerful signals, whose attributes are not fully characterized or understood, will invariably lead to the generation of image ghosts. Through “cleaning”, the WMAP team is taking the risk that it is generating image ghosts. The removal of powerful signals, at certain image locations, can easily be associated with the generation of weak signals at the same (or other) image locations, just as a result of processing. The lesson from Figure 6 applies.

Consequently, the WMAP team is unable to distinguish whether the “features” found in its images are truly of cosmological importance, or whether these features are simply the result of processing (and/or acquiring) a much larger contaminating signal from the galaxy. It is clear, for instance, that K band reveals galactic signal at virtually every point in the sky map (see Figure 1). The same contaminations must be expected in all other bands. That the human eye fails to visualize contamination does not mean that contamination is absent. Because any real signal will be weak, and the contaminating signal is so strong, the WMAP team is unable to distinguish spurious ghosts related to either processing or acquisition from the actual signal of interest. This is true at every image location.

Data processing artifacts tend to be extremely consistent on images. Since similar mathematical methods must be utilized to clean the raw images and zero the galactic foreground, it is highly likely that a significant portion of the maps contains such spurious ghosts. This is especially true given that the WMAP team has chosen to invoke complex mathematical methods for “cleaning” their raw images. That a given image location cannot be positively ascertained to be free of contamination implies that none of the image locations can be validated as free of galactic ghosts on any map. Therein lies the overwhelming complication of dealing with powerful contaminating signals while trying to examine weak ones. Apparent anisotropy must not be generated by processing.

2.2.3 Signal to noise, contrast, and resolution

There is perhaps no more important determinant of image quality than signal to noise. In medicine, signal to noise can directly impact diagnosis. As such, radiological methods which are rich in signal to noise are always sought. If signal to noise is high ($>100:1$), then image quality will almost certainly be outstanding. Methods which have high signal to noise can “burn signal” to generate either contrast, resolution, or shortened exam times. Consequently, signal to noise is paramount. Without it, resolution will remain poor and

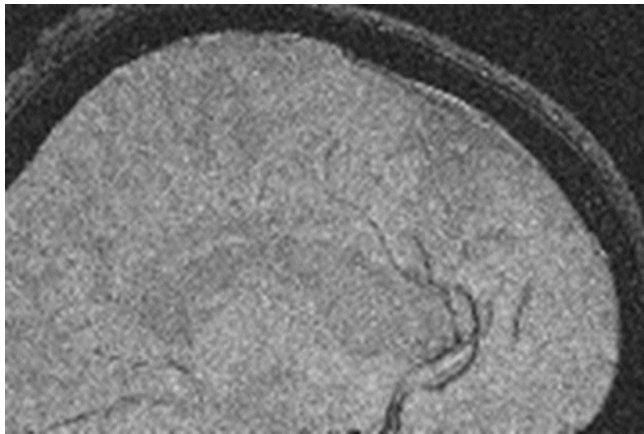


Fig. 8: Section (490×327) of a high resolution sagittal image of the human head acquired at 1.5 Tesla. Acquisition parameters are as follows: acquisition sequence = gradient recalled echo, matrix size = 512×512 , slice thickness = 2 mm, field of view 20 cm \times 20 cm, repetition time = 750 msec, echo time = 17 msec, and nutation angle = 45 degrees.

contrast will rapidly deteriorate. In fact, enhancements in signal to noise were the primary driving force for the introduction of Ultra High Field MRI [40–42].

In order to gain some insight into the importance of signal to noise, one can examine the images displayed in Figures 8 and 9. Figure 8 corresponds to a sagittal section of a human brain, acquired using a 1.5 Tesla MRI scanner. There are more than 15,000 such scanners in existence. In this image, the 1.5 Tesla instrument was brought to the very limits of its performance [43]. The resolution is high (matrix size = 512×512) and the slice thickness is thin (2 mm). At the same time, the nutation angle, echo times, and repetition times are all suboptimal. As a result, this image is of extremely poor clinical quality. The contrast between grey and white matter has disappeared and the signal to noise is ~ 5 .

Figure 9 was acquired with the first UHFMRI scanner [40–42]. This scanner operates at a field strength of 8 Tesla. Note the phenomenal contrast, the delineation of grey and white matter and the appearance of vasculature. Interestingly, this image was acquired with a much larger image resolution (matrix size = $2,000 \times 2,000$) while maintaining nearly the

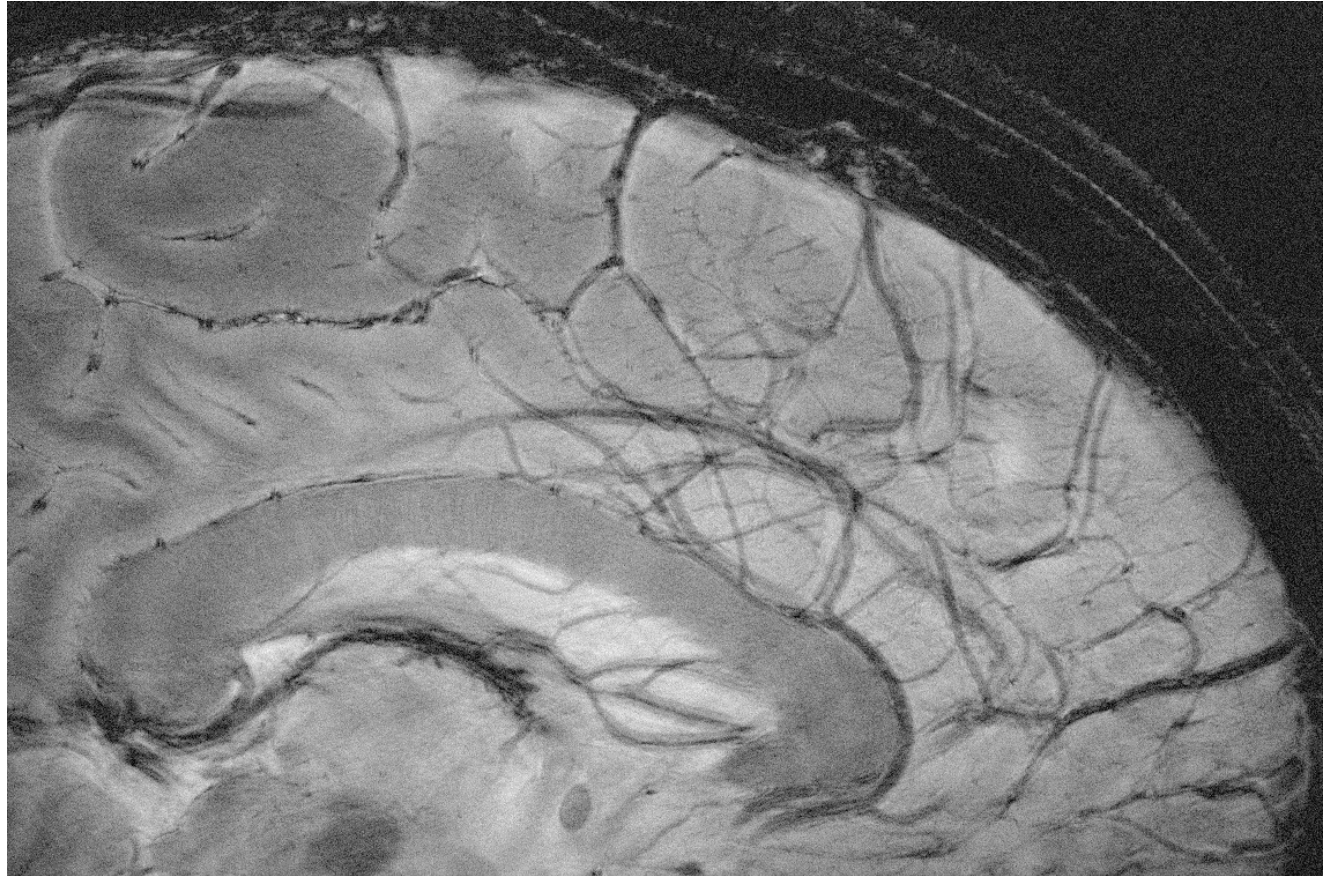


Fig. 9: Section (1139×758) of a high resolution sagittal image of the human head acquired at 8 Tesla. Acquisition parameters are as follows: acquisition sequence = gradient recalled echo, matrix size = $2,000 \times 2,000$, slice thickness = 2 mm, field of view 20 cm \times 20 cm, repetition time = 750 msec, echo time = 17 msec, and nutation angle = 17 degrees. This image corresponds to Figure 3A in Robitaille P.M.L., Abduljalil A.M., Kangarlu A. Ultra high resolution imaging of the human head at 8 Tesla: 2K \times 2K for Y2K. *J Comp. Assist. Tomogr.*, 2000, v. 24, 2–7. Reprinted with permission.

same parameters as found for Figure 8. Despite higher resolution, the image has a signal to noise of ~ 20 . It did take longer to acquire, due to increased phase encoding steps, but the time per pixel remains less than that for Figure 8. Clearly, signal to noise can purchase both contrast and resolution.

Images with high signal to noise also tend to be “reliable”. Namely, their gross features are rarely affected by minor fluctuations, in either the instrument or the sample. High signal to noise images tend to have the quality of stability and reproducibility, attributes which are often lost in low signal to noise images. In fact, the only measure of reliability for a low signal to noise image is reproducibility. It is important to establish that a low signal to noise image does not change from one acquisition to the next.

Figure 10A-C displays three low signal to noise images. In these images, a computer has added random noise, such that the final signal to noise is $\sim 2.5:1$ in each case. Figure 10A corresponds to an axial image of the human head. Its identity is revealed by the presence of signal arising both from the brain and the scalp. The image is relatively uniform in signal, making the assignment simple. Figure 10B corresponds to a photograph of the Moon. The subject can be distinguished from other spherical objects (a baseball, the Sun, etc.) through the gentle change in contrast, produced by craters on the lunar surface. The object is difficult to identify since the shape provides few clues. Figure 10C corresponds to an MRI image of the author’s wrist. In this image, it is increasingly difficult to ascertain the source. The maximal signal to noise remains $\sim 2.5:1$. However, the signal distribution is no longer uniform. Faint features can be seen on the image, but no detail. Inhomogeneous signal distributions often make images more challenging to interpret, particularly when the origin of the sample is not known.

In Figure 11A-C, the images of Figure 10A-C are reproduced, but this time the signal to noise is at least $5:1$. A nearly 10-fold increase in signal to noise for the head image (A) is now associated with increased contrast. The same holds true for the wrist image displayed (C) with a signal to noise of $\sim 40:1$. Thus, the first rule of image contrast is that it is non-existent on low signal to noise images. It takes signal to make contrast. If the images in Figure 11 look so much more appealing, it is because they have higher signal to noise and contrast. It is also interesting that a mere doubling of signal to noise has such a dramatic effect for the Moon image. This highlights that there is also an enormous difference between an image with a $1.5:1$ signal to noise and an image with a $2.5:1$ signal to noise.

Unfortunately, in the WMAP images, the maximum signal to noise is just in excess of 1. This can be ascertained in Figures 12 and 13. Figure 12 displays a map of instrument noise released by NASA for WMAP. The largest signals on this map have a noise power of approximately 70 uK . Figure 12 displays a corresponding map, created by combining the Q and V bands. The galactic plane dominates the figure with

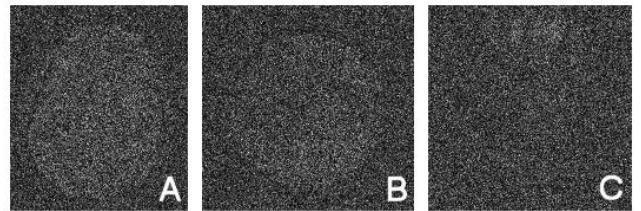


Fig. 10: A set of images generated by adding random noise to the images displayed in Figure 11. A maximum signal to noise of $\sim 2.5:1$ is now illustrated. (A) MRI image of the human head at 1.5 Tesla, (B) photographic image of the Moon, and (C) MRI image of the author’s wrist acquired at 8 Tesla.

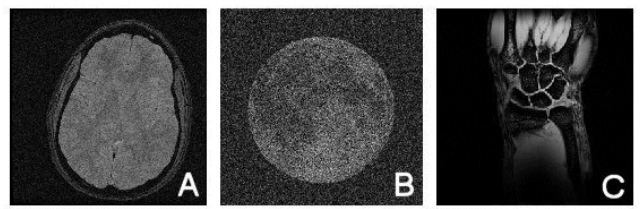


Fig. 11: Images displaying varying signal to noise. (A) MRI image of the human head at 1.5 Tesla with signal to noise $\sim 20:1$, (B) photographic image of the Moon with the signal to noise adjusted to $\sim 5:1$, and (C) MRI image of the human wrist acquired at 8 Tesla with the signal to noise $\sim 40:1$. Note the dramatic effect on image quality for the moon image (B) in simply doubling the signal to noise (see Figure 10B).

signal truncated at the 100 uK level. Outside the galactic plane, few signals, if any, exist at the 100 uK level. As such, by combining the information in Figure 13 with the image in Figure 12, it is clear that the WMAP signal to noise is below $2:1$ and probably below 1.5 . In fact, since these images are obtained by difference methods, the signal to noise at many locations is much less than 1. It is clear that some of the data points on these images have signal values of 0. Therefore, the real signal to noise on the anisotropy maps is somewhere between 0 and 1.5 at all locations. Note, in contrast, that the example images in Figures 10A, B, and C had a maximum signal to noise of $\sim 2.5:1$, well in excess of WMAP and without the presence of a contaminating foreground.

Relative to signal to noise, the WMAP team is unable to confirm that the anisotropic “signal” observed at any given point is not noise. The act of attributing signal characteristics to noise does not in itself create signal. Reproducibility remains the key, especially when signal to noise values are low.

2.2.4 Reproducibility

The presence of low signal to noise on an image is not unusual in science, and many a great discovery has been made through the careful analysis of the faintest signals. In medicine, the tremendous advancements in functional MRI mapping of the brain [44–46] stand perhaps without rival,

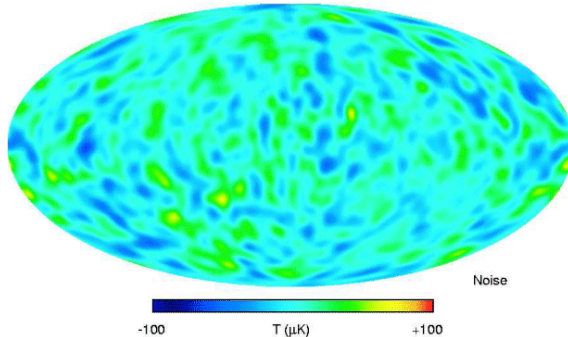


Fig. 12: Map of the instrument noise for WMAP. This image corresponds to the lower portion of Figure 9 in Bennett et. al. [7]. Reproduced with permission of the AAS. Image provided courtesy of the NASA/WMAP team.

relative to lack of signal to noise and the profoundness of the implications. Whenever the signal to noise is low, care must be exercised such that noise is not mistaken for signal. The key to this problem is reproducibility.

In medicine, when an image has poor signal to noise, it is vital that its central features be reproducible.

In fact, the only measure of reliability for a low signal to noise image is reproducibility. The information contained within the image must not change from one acquisition to the next. Correlation between an event and the change in an image are also powerful indicators that the change is real. This principle has been applied extensively in human functional MRI [44–46]. In this case, cognitive tasks, such as visual activation or finger tapping, can be directly correlated to very small changes on the MRI images of the human brain [44–46]. Often, changes on a pixel by pixel basis, with a signal to noise change on the order of 5:1 or even less, can be trusted simply based on correlation. In medicine, whenever a known physiological change (blood flow, blood oxygenation level, and myocardial contraction) can be correlated to radiological changes, even low signal to noise images can yield powerful diagnostic conclusions. Three components in this case act in unison to produce the diagnosis: instrument stability, image reproducibility, and the presence of correlation.

Note, most importantly, that in medicine, when low signal to noise images are used for diagnosis, it is never in the presence of strong overlapping contaminating signal. Moreover, in human functional imaging, a set of control images are acquired to help ensure that all perceived changes are real.

Unfortunately for WMAP, not only are the images obscured by galactic contamination, but they do not appear to be reproducible. In this regard, it is concerning that the WMAP team chooses to alter the ILC coefficients for generating section 0 from year to year. In fact, the coefficients used in year-1 (0.109, -0.684, -0.096, 1.921, and -0.250) are substantially different from those used in presenting a 3-year average (0.1559, -0.8880, 0.0297, 2.0446, and

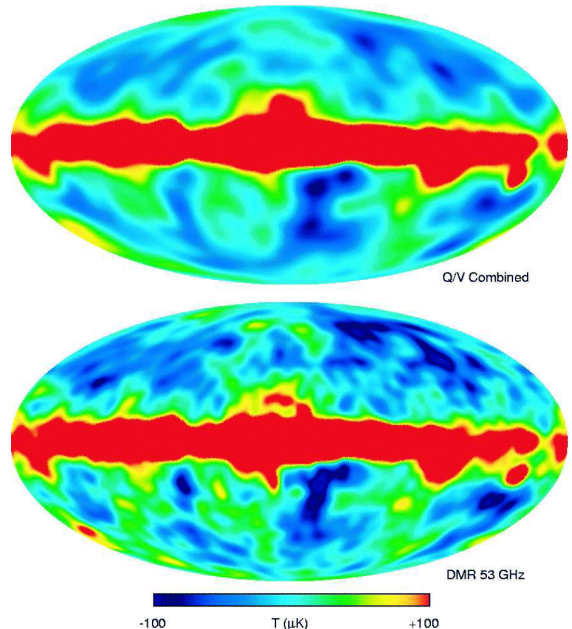


Fig. 13: The 53 GHz map from COBE (bottom) and the combined Q/V map generated by the WMAP team. This Figure corresponds to Figure 8 in Bennett et. al. [7]. Reproduced with permission of the AAS. Image provided courtesy of the NASA/WMAP team.

-0.3423). The coefficient for K band has changed by nearly 50%, while the coefficient for Q band not only changes sign, but decreases in magnitude by a factor of 3. Such changes cannot be simply explained by variations in instrument gain over time. The WMAP team does describe an attempt to find the maximum likelihood map in the 3-year data presentation. This new approach may account for some of the variability. Nonetheless, the WMAP team should have reprocessed the data from all years using this new approach, so that a direct comparison could be made between images processed with identical parameters.

It is also concerning that the WMAP team does not present separate ILC images for years 1, 2, and 3. Rather, after presenting the year-1 ILC image in 2003, they then compare it only to the 3-year average in 2006. However, the 3-year average contains data from the first year. The proper test for reproducibility involves the comparison of each yearly ILC image with one another, without invoking the 3-year average. Ideally, difference ILC images should be taken from year-1 and year-2, year-2 and year-3, and finally from year-1 and year-3. The WMAP team neglects to present these vital comparisons.

Despite these objections, the first year image simply does not agree with the 3-year average. It is true that the images generally agree, but this does not occur on a pixel by pixel, or even a regional basis. This can be readily visualized in the difference images displayed in Figures 14 and 15. In fact, the situation is actually worse than can be easily gathered, since the coefficients used in generating the first year ILC maps

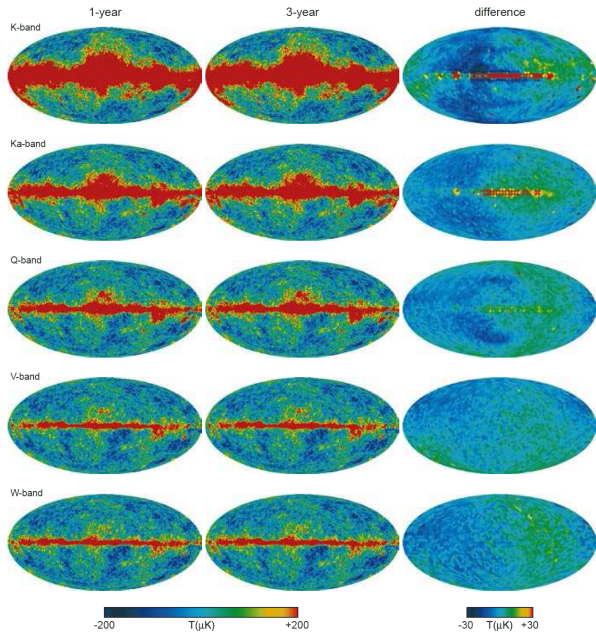


Fig. 14: Comparison of 3-year average data with year-1 data through difference for the K, Ka, Q, V, and W bands of the WMAP satellite. Note that the difference images are shown with reduced resolution contrary to established practices in imaging science. This figure corresponds to Figure 3 in Hinshaw et. al. [23]. Reproduced with permission of the AAS. Image provided courtesy of the NASA/WMAP team.

do not agree with those used for the 3-year average map. The comparison made by the WMAP team in Figure 15 is not valid, since the images were generated using different coefficients.

Perhaps most troubling, the WMAP team chooses to reduce the resolution on its difference images. This approach is known to minimize apparent differences. In imaging, the only resolution which can be claimed is that which can be trusted on difference. As such, if the difference images must be degraded to a pixel resolution of 4 degrees, then the WMAP team cannot claim to have imaged the sky at a 1 degree resolution.

Tremendous variability can be observed in the WMAP data sets. This is apparent by examining the variability found in the galactic foreground. It has been well established in astrophysics that galaxies can contain Active Galactic Nuclei. These have been studied extensively outside the microwave region [47]. These nuclei can vary by an order of magnitude in certain frequency bands [47]. Even in the microwave, it is clear that our own galaxy is highly variable from year to year. This is evidenced by the need to change, from year to year, the coefficients required to null the galactic contribution. The galaxy is highly variable in the microwave relative to the magnitude of any real anisotropy. This is an observation which could be made by examining old data from COBE [48]. Given this state, it is also clear that every galaxy in the

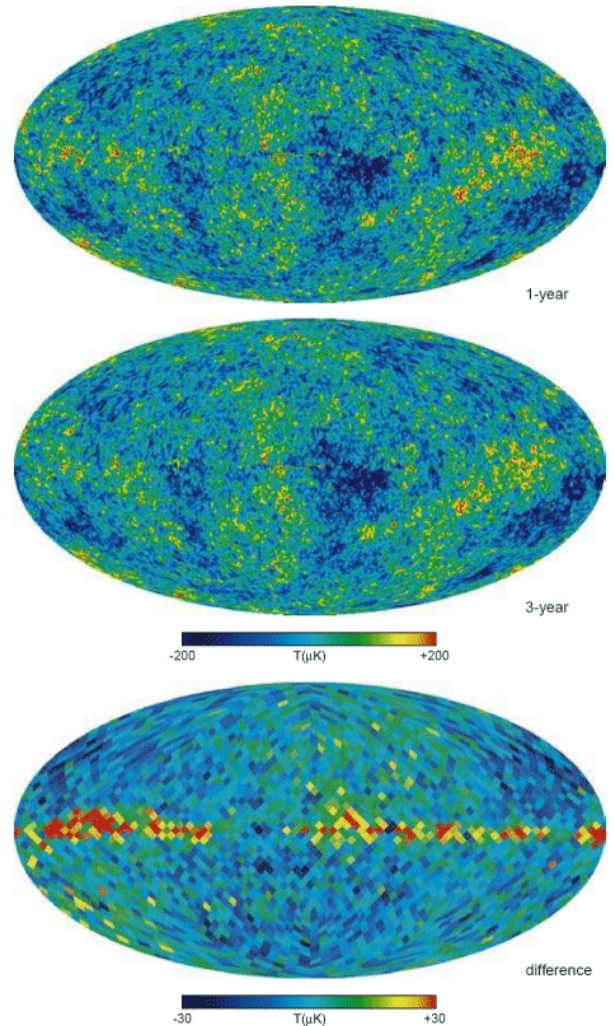


Fig. 15: Comparison of the 3-year average ILC map with the year-1 ILC map. Note that the difference images are shown at reduced resolution contrary to established practices in imaging science. This figure corresponds to Figure 9 in Hinshaw et. al. [23]. Reproduced with permission of the AAS. Image provided courtesy of the NASA/WMAP team.

Universe will also share in this variability in a manner which is completely dissociated from any cosmological implication. Indeed, herein lies another great problem for the cosmologist. It is impossible to visualize, in our lifetime, the true simple galactic variability not only from our galaxy, but from every other galaxy. Even a signal which appears stable over the course of humanity's existence may well be variable.

Consider the case where only 4 pixels vary substantially over the course of the WMAP experiment from year-1 to year-4. From this situation, it can be expected that as many as 1,000 pixels might vary over the course of 1,000 years. Yet, 1,000 years is barely on the cosmological timescale. Over the course of 1,000,000 years, a total of 1,000,000 pixels could be potentially affected. Even 1,000,000 years is just starting to be meaningful relative to cosmology. As a

result, the situation relative to WMAP and COBE is extremely difficult. In reality, in order to have true cosmological meaning, the maps must be temporally stable well beyond what has been determined to date. The situation is much worse than the hypothetical case described above, as significantly more than 4 pixels will vary between year-4 and year-1. The requirements for image stability in cosmology is well beyond the reach of both COBE and WMAP.

2.3 The flat model of the Universe

Bennett et. al. [7] claim that the WMAP results are consistent with a 2-dimensional flat model of the Universe. Clearly, by their intrinsic nature, these images are incapable of supporting any higher order model. WMAP cannot establish the origin of the photons which it detects other than in a directional sense. The satellite is completely unable to differentiate data based on distance to the source. In this respect, WMAP images resemble classic X-rays in medicine. Such images are 2-dimensional and unable to reveal the 3-dimensional nature of the human being. WMAP and X-rays stand in sharp contrast to the CT and MRI systems of today, which are able to provide a true 3-dimensional visualization of the human body. That the flat model of the Universe can be fitted is completely appropriate, given that this data cannot be utilized to model a 3-dimensional Universe.

2.4 The assignment of brightness temperature

Perhaps the most serious concern relative to the Penzias and Wilson, COBE, and WMAP findings involves the assignment of brightness temperatures [49]. The Universe is not in thermal equilibrium with a perfectly absorbing enclosure [49, 50, 51, 52]. As a result, the assignment of these temperatures constitutes a violation of Kirchhoff's Law [50, 52]. It is improper to assign a temperature merely because a spectrum has a thermal appearance. That a spectrum appears thermal does not imply that it was generated by a blackbody [52, 53]. Indeed, the proper application of the laws of Planck [54], Stefan [55], and Wien [56] requires that the emitting sample corresponds to a solid, best approximated on Earth by graphite or soot [50]. It has been advanced [49, 57–59], and it is herein restated, that the monopole signal first detected by Penzias and Wilson, and later confirmed by COBE, will eventually be reassigned to the oceans of the Earth. The brightness temperature does not appear to make any sense precisely because the oceans fail to meet the requirements set forth by Kirchhoff in assigning a temperature [50, 52, 53].

In this regard, the basis of universality in blackbody radiation has come under serious question [52, 53]. Blackbody radiation is not universal. Rather, it is strictly limited to an experimental setting which, on Earth, is best approximated by graphite and soot [52]. That Kirchhoff interchangeably used either an adiabatic enclosure or an isothermal one was a

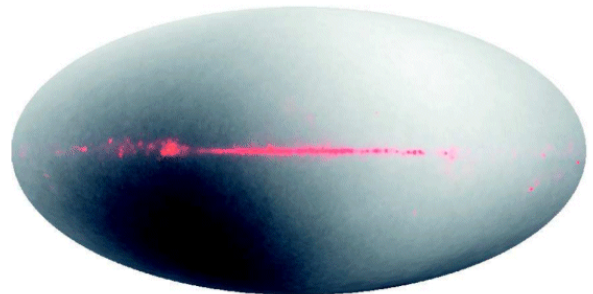


Fig. 16: The microwave dipole observed by the WMAP satellite. This image corresponds to the upper portion of Figure 10 in Bennett et. al. [7]. Reproduced with permission of the AAS. Image provided courtesy of the NASA/WMAP team.

natural extension of his belief in universality. Nonetheless, it appears that the adiabatic case is not valid [52]. Kirchhoff's experiments far from supporting universality, actually constrains blackbody radiation to the perfect absorber [52]. Conditions for assigning a blackbody temperature are even more stringent [52] than previously believed [58]. As such, an adiabatic enclosure is not sufficient [52, 58]. Rather, in order to obtain a proper temperature, the enclosure can only be perfectly absorbing and isothermal. The assignment of these temperatures by the WMAP team constitutes an overextension of the fundamental laws which govern thermal emission, given the lack of universality [52, 53].

2.5 The Dipole Temperature

Despite this discussion, it is nonetheless clear that the WMAP satellite has detected a CMB dipole signal presumably associated with motion of the local group [7, 23]. The dipole signal is shown in Figure 16. The presence of a dipole is thought, by many, as further proof for the presence of the monopole signal at the position of WMAP. The detection of this dipole by WMAP constitutes a finding of importance as it confirms earlier findings, both by the COBE team [60] and by the Soviet Relikt-1 mission [61]. Indeed, the discussion of the dipole is sufficiently important to be treated separately [62].

3 Conclusion

Analysis of data from WMAP exposes several problems which would not be proper in medical imaging. Experience from NMR spectroscopy relative to biological samples reveals that removal of a contaminating signal, which exceeds the signal of interest by up to a factor of 1,000, requires ability to control the sample at the source. This requirement can never be met by the WMAP team. It is impossible to remove this contamination and thereby "see beyond the galaxy". It is also dangerous to mathematically manipulate large signals during image reconstruction, especially when the final images have low signal to noise ratios. The

galactic signal is not stable from year to year, making signal removal a daunting task as seen by the yearly changes in ILC coefficients for regions 1–11. In actuality, the WMAP team must overcome virtually every hurdle known to imaging: foreground contamination and powerful dynamic range issues, low signal to noise, poor contrast, limited sample knowledge, lack of reproducibility, and associated resolution issues. It is clear that the generation of a given anisotropy map depends strictly on the arbitrary weighting of component images. The WMAP team attempts to establish a “most likely” anisotropy map using mathematical tools, but they have no means of verifying the validity of the solution. Another team could easily produce its own map and, though it may be entirely different, it would be equally valid. Figure 5 points to this fact. It remains surprising that separate ILC maps are not presented for years 1, 2, and 3. In addition, the WMAP team does not use the proper tests for reproducibility. Difference images between all three yearly ILC maps should be presented, without lowering the final resolution, and without changing the ILC coefficient from year to year. It is improper to compare images for reproducibility if they are not processed using identical methods. Reproducibility remains a critical issue for the WMAP team. This issue will not be easily overcome given human technology. In order to make cosmological interpretations, the WMAP images must be perfectly stable from year to year. Even fluctuation at the level of a few pixels has dramatic consequences, since the data must be stable on a cosmological timescale. This timescale extends over hundreds, perhaps thousands, or even millions of years. Finally, there are fundamental issues at stake, relative to the application of the laws of Kirchhoff [50], Planck [54], Stefan [55], and Wien [56]. It has not been established that the WMAP team is theoretically justified in assigning these temperatures.

The only significant observations relative to this satellite are related to the existence of a dipole signal [7, 23]. This confirms findings of both the NASA COBE [60], and the Soviet Relik, satellites [61]. The WMAP satellite also highlights that significant variability exists in the point sources and in the galactic foreground. Relative to the Universe, the findings imply isotropy over large scales, not anisotropy. All of the cosmological constants which are presented by the WMAP team are devoid of true meaning, precisely because the images are so unreliable. Given the tremendous dynamic range problems, the inability to remove the galactic foreground, the possibility of generating galactic ghosts through “cleaning”, the lack of signal to noise, the lack of reproducibility, the use of coefficients which fluctuate on a yearly basis, and the problem of monitoring results on a cosmological timescale, attempts to determine cosmological constants from such data fall well outside the bounds of proper image interpretation.

In closing, it may well be appropriate to reflect once again on the words of Max Planck [63]:

“The world is teeming with problems. Wherever man looks, some new problems crops up to meet his eye — in his home life as well as in his business or professional activity, in the realm of economics as well as in the field of technology, in the arts as well as in science. And some problems are very stubborn; they just refuse to let us in peace. Our agonizing thinking of them may sometimes reach such a pitch that our thoughts haunt us throughout the day, and even rob us of sleep at night. And if by lucky chance we succeed in solving a problem, we experience a sense of deliverance, and rejoice over the enrichment of our knowledge. But it is an entirely different story, and an experience annoying as can be, to find after a long time spent in toil and effort, that the problem which has been preying on one’s mind is totally incapable of any solution at all.”

Acknowledgements

The author would like to thank The Ohio State University for ongoing support. Luc Robitaille was responsible for the retrieval and preparation of all figures for the manuscript. The assistance of Professor Robert W. Curley is acknowledged for sample preparation and NMR acquisition required in Figure 3. The members of the Center for Advanced Biomedical Imaging associated with the design and construction of the 8 Tesla UHFMRI system [40–41] are acknowledged for enabling the acquisition and processing of the images displayed in Figures 6, 8, 9, 10, and 11.

*First published online on November 01, 2006
Corrections posted online on December 30, 2006*

References

1. WMAP website, <http://map.gsfc.nasa.gov/>.
2. Seife C. Breakthrough of the year: illuminating the dark Universe. *Science*, 2003, v. 302, 2038–2039.
3. Bennett C.L., Bay M., Halpern M., Hinshaw G., Jackson C., Jarosik N., Kogut A., Limon M., Meyer S.S., Page L., Spergel D.N., Tucker G.S., Wilkinson D.T., Wollack E., Wright E.L. The Microwave Anisotropy Probe mission. *Astrophys. J.*, 2003, v. 583(1), 1–23.
4. Jarosik N., Bennett C.L., Halpern M., Hinshaw G., Kogut A., Limon M., Meyer S.S., Page L., Pospieszcalski M., Spergel D.N., Tucker G.S., Wilkinson D.T., Wollack E., Wright E.L., Zhang Z. Design, implementation and testing of the MAP radiometers. *Astrophys. J. Suppl. Ser.*, 2003, v. 145(2), 413–436.
5. Page L., Jackson C., Barnes C., Bennett C.L., Halpern M., Hinshaw G., Jarosik N., Kogut A., Limon M., Meyer S.S., Spergel D.N., Tucker G.S., Wilkinson D.T., Wollack E., Wright E.L. The optical design and characterization of the

- Wilkinson Microwave Anisotropy Probe. *Astrophys. J.*, 2003, v. 585(1), 566–586.
6. Barnes C., Limon M., Page L., Bennett C.L., Bradley S., Halpern M., Hinshaw G., Jarosik N., Jones W., Kogut A., Meyer S., Motrunich O., Tucker G., Wilkinson D., Wollack E. The MAP satellite feed horns. *Astrophys. J. Suppl. Ser.*, 2002, v. 143(2), 567–576.
 7. Bennett C.L., Halpern M., Hinshaw G., Jarosik N., Kogut A., Limon M., Meyer S.S., Page L., Spergel D.N., Tucker G.S., Wollack E., Wright E.L., Barnes C., Greason M.R., Hill R.S., Komatsu E., Nolta M.R., Odegard N., Peiris H.V., Verde L., Weiland J.L. First-year Wilkinson Microwave Anisotropy Probe (WMAP) observations: preliminary maps and basic results. *Astrophys. J. Suppl. Ser.*, 2003, v. 148(1), 1–27.
 8. Hinshaw G., Barnes C., Bennett C.L., Greason M.R., Halpern M., Hill R.S., Jarosik N., Kogut A., Limon M., Meyer S.S., Odegard N., Page L., Spergel D.N., Tucker G.S., Weiland J.L., Wollack E., Wright E.L. First year Wilkinson Microwave Anisotropy Probe (WMAP) observations: data processing methods and systematic error limits. *Astrophys. J. Suppl. Ser.*, 2003, v. 148(1), 63–95.
 9. Jarosik N., Barnes C., Bennett C.L., Halpern M., Hinshaw G., Kogut A., Limon M., Meyer S.S., Page L., Spergel D.N., Tucker G.S., Weiland J.L., Wollack E., Wright E.L. First year Wilkinson Microwave Anisotropy Probe (WMAP) observations: on-orbit radiometer characterization. *Astrophys. J. Suppl. Ser.*, 2003, v. 148(1), 29–37.
 10. Page L., Barnes C., Hinshaw G., Spergel D.N., Weiland J.L., Wollack E., Bennett C.L., Halpern M., Jarosik N., Kogut A., Limon M., Meyer S.S., Tucker G.S., Wright E.L. First year Wilkinson Microwave Anisotropy Probe (WMAP) observations: beam profiles and window functions. *Astrophys. J. Suppl. Ser.*, 2003, v. 148(1), 39–50.
 11. Barnes C., Hill R.S., Hinshaw G., Page L., Bennett C.L., Halpern M., Jarosik N., Kogut A., Limon M., Meyer S.S., Tucker G.S., Wollack E., Wright E.L. First year Wilkinson Microwave Anisotropy Probe (WMAP) observations: galactic signal contamination from sidelobe pickup. *Astrophys. J. Suppl. Ser.*, 2003, v. 148(1), 51–62.
 12. Bennett C.L., Hill R.S., Hinshaw G., Nolta M.R., Odegard N., Page L., Spergel D.N., Weiland J.L., Wright E.L., Halpern M., Jarosik N., Kogut A., Limon M., Meyer S.S., Tucker G.S., Wollack E. First year Wilkinson Microwave Anisotropy Probe (WMAP) observations: foreground emission. *Astrophys. J. Suppl. Ser.*, 2003, v. 148(1), 97–117.
 13. Hinshaw G., Spergel D.N., Verde L., Hill R.S., Meyer S.S., Barnes C., Bennett C.L., Halpern M., Jarosik N., Kogut A., Komatsu E., Limon M., Page L., Tucker G.S., Weiland J.L., Wollack E., Wright E.L. First year Wilkinson Microwave Anisotropy Probe (WMAP) observations: the angular power spectrum. *Astrophys. J. Suppl. Ser.*, 2003, v. 148(1), 135–159.
 14. Kogut A., Spergel D.N., Barnes C., Bennett C.L., Halpern M., Hinshaw G., Jarosik N., Limon M., Meyer S.S., Page L., Tucker G.S., Wollack E., Wright E.L. First year Wilkinson Microwave Anisotropy Probe (WMAP) observations: temperature-polarization correlation. *Astrophys. J. Suppl. Ser.*, 2003, v. 148(1), 161–173.
 15. Spergel D.N., Verde L., Peiris H.V., Komatsu E., Nolta M.R., Bennett C.L., Halpern M., Hinshaw G., Jarosik N., Kogut A., Limon M., Meyer S.S., Page L., Tucker G.S., Weiland J.L., Wollack E., Wright E.L. First year Wilkinson Microwave Anisotropy Probe (WMAP) observations: determination of cosmological parameters. *Astrophys. J. Suppl. Ser.*, 2003, v. 148, 175–194.
 16. Verde L., Peiris H.V., Spergel D.N., Nolta M.R., Bennett C.L., Halpern M., Hinshaw G., Jarosik N., Kogut A., Limon M., Meyer S.S., Page L., Tucker G.S., Wollack E., Wright E.L. First year Wilkinson Microwave Anisotropy Probe (WMAP) observations: parameter estimation methodology. *Astrophys. J. Suppl. Ser.*, 2003, v. 148(1), 195–211.
 17. Peiris H.V., Komatsu E., Verde L., Spergel D.N., Bennett C.L., Halpern M., Hinshaw G., Jarosik N., Kogut A., Limon M., Meyer S.S., Page L., Tucker G.S., Wollack E., Wright E.L. First year Wilkinson Microwave Anisotropy Probe (WMAP) observations: implications for inflation. *Astrophys. J. Suppl. Ser.*, 2003, v. 148(1), 213–231.
 18. Page L., Nolta M.R., Barnes C., Bennett C.L., Halpern M., Hinshaw G., Jarosik N., Kogut A., Limon M., Meyer S.S., Peiris H.V., Spergel D.N., Tucker G.S., Wollack E., Wright E.L. First year Wilkinson Microwave Anisotropy Probe (WMAP) observations: interpretation of the TT and TE angular power spectrum peaks. *Astrophys. J. Suppl. Ser.*, 2003, v. 148(1), 233–241.
 19. Komatsu E., Kogut A., Nolta M.R., Bennett C.L., Halpern M., Hinshaw G., Jarosik N., Limon M., Meyer S.S., Page L., Spergel D.N., Tucker G.S., Verde L., Wollack E., Wright E.L. First year Wilkinson Microwave Anisotropy Probe (WMAP) observations: tests of Gaussianity. *Astrophys. J. Suppl. Ser.*, 2003, v. 148(1), 119–134.
 20. Barnes C., Bennett C.L., Greason M.R., Halpern M., Hill R.S., Hinshaw G., Jarosik N., Kogut A., Komatsu E., Landsman D., Limon M., Meyer S.S., Nolta M.R., Odegard N., Page L., Peiris H.V., Spergel D.N., Tucker G.S., Verde L., Weiland J.L., Wollack E., Wright E.L. First year Wilkinson Microwave Anisotropy Probe (WMAP) observations: explanatory supplement. http://lambda.gsfc.nasa.gov/product/map/pub_papers/firstyear/supplement/WMAP_supplement.pdf
 21. Nolta M.R., Wright E.L., Page L., Bennett C.L., Halpern M., Hinshaw G., Jarosik N., Kogut A., Limon M., Meyer S.S., Spergel D.N., Tucker G.S., Wollack E. First year Wilkinson Microwave Anisotropy Probe observations: dark energy induced correlation with radio sources. *Astrophys. J.*, 2004, v. 608(1), 10–15.
 22. Jarosik N., Barnes C., Greason M.R., Hill R.S., Nolta M.R., Odegard N., Weiland J.L., Bean R., Bennett C.L., Dore O., Halpern M., Hinshaw G., Kogut A., Komatsu E., Limon M., Meyer S.S., Page L., Spergel D.N., Tucker G.S., Wollack E., Wright E.L. Three-year Wilkinson Microwave Anisotropy Probe (WMAP) observations: beam profiles, data processing, radiometer characterization and systematic error limits. *Astrophys. J.*, 2006, submitted.
 23. Hinshaw G., Nolta M.R., Bennett C.L., Bean R., Dore O., Greason M.R., Halpern M., Hill R.S., Jarosik N., Kogut A., Komatsu E., Limon M., Odegard N., Meyer S.S., Page L.,

- Peiris H.V., Spergel D.N., Tucker G.S., Verde L., Weiland J.L., Wollack E., Wright E.L. Three-year Wilkinson Microwave Anisotropy Probe (WMAP) observations: temperature analysis. *Astrophys. J.*, 2006, submitted.
24. Page L., Hinshaw G., Komatsu E., Nolta M.R., Spergel D.N., Bennett C.L., Barnes C., Bean R., Dore O., Halpern M., Hill R.S., Jarosik N., Kogut A., Limon M., Meyer S.S., Odegard N., Peiris H.V., Tucker G.S., Verde L., Weiland J.L., Wollack E., Wright E.L. Three-year Wilkinson Microwave Anisotropy Probe (WMAP) observations: polarization analysis. *Astrophys. J.*, 2006, submitted.
25. Spergel D.N., Bean R., Dore O., Nolta M.R., Bennett C.L., Hinshaw G., Jarosik N., Komatsu E., Page L., Peiris H.V., Verde L., Barnes C., Halpern M., Hill R.S., Kogut A., Limon M., Meyer S.S., Odegard N., Tucker G.S., Weiland J.L., Wollack E., Wright E.L. Three-year Wilkinson Microwave Anisotropy Probe (WMAP) observations: implications for cosmology. *Astrophys. J.*, 2006, submitted.
26. Barnes C., Bean R., Bennett C.L., Dore O., Greason M.R., Halpern M., Hill R.S., Hinshaw G., Jarosik N., Kogut A., Komatsu E., Landsman D., Limon M., Meyer S.S., Nolta M.R., Odegard N., Page L., Peiris H.V., Spergel D.N., Tucker G.S., Verde L., Weiland J.L., Wollack E., Wright E.L. Three-year Wilkinson Microwave Anisotropy Probe (WMAP) observations: three year explanatory supplement. http://map.gsfc.nasa.gov/m_mm/pub_papers/supplement/wmap_3yr_supplement.pdf
27. NASA, new satellite data on Universe's first trillionth second. WMAP Press Release. http://map.gsfc.nasa.gov/m_or/PressRelease_03_06.html.
28. In-cites. "Super hot" papers in science published since 2003. <http://www.in-cites.com/hotpapers/shp/1-50.html>.
29. Tegmark M., de Oliveira-Costa A., Hamilton A.J.S. A high resolution foreground cleaned CMB map from WMAP. *Phys. Rev. D*, 2003, v. 68(12), 123523.
30. Robitaille P.M.L., Scott R.D., Wang J., Metzler D.E. Schiff bases and geminal diamines derived from pyridoxal 5'-phosphate and diamines. *J. Am. Chem. Soc.*, 1989, v. 111, 3034–3040.
31. Robyt J.F., White B.J. Biochemical techniques: theory and practice. Brooks/Cole Publishing Company, Monterey, CA, 1987, p. 261–262.
32. Schaefer J. Selective saturation of Carbon-13 lines in Carbon-13 Fourier transform NMR experiments. *J. Magn. Reson.*, 1972, v. 6, 670–671.
33. Plateau P., Guerrier M. Exchangeable proton NMR without baseline distortion, using new strong pulse sequences. *J. Am. Chem. Soc.*, 1982, v. 104, 7310–7311.
34. Redfield A.G., Kunz S.D., Ralph E.K. Dynamic range in Fourier transform proton magnetic resonance. *J. Magn. Reson.*, 1975, v. 19, 114–117.
35. Sklenar V., Starcuk Z. 1-2-1 pulse train: a new effective method of selective excitation for proton NMR in water. *J. Magn. Reson.*, 1983, v. 54, 146–148.
36. Turner D.L. Binomial solvent suppression. *J. Magn. Reson.*, 1983, v. 54, 146–148.
37. Hurd R.E. Gradient enhanced spectroscopy. *J. Magn. Reson.*, 1990, v. 87(2), 422–428.
38. Moonen C.T.W., van Zijl P.C.M. Highly effective water suppression for in-vivo proton NMR-spectroscopy (DRYSTEAM). *J. Magn. Reson.*, 1990, v. 88(1), 28–41.
39. Cavanagh J., Fairbrother J.W., Palmer III A.G., Skelton N.J. Protein NMR spectroscopy: principles and practice. Academic Press, New York, 1995.
40. Robitaille P.M.L., Abduljalil A.M., Kangarlu A., Zhang X., Yu Y., Burgess R., Bair S., Noa P., Yang L., Zhu H., Palmer B., Jiang Z., Chakeres D.M., Spigos D. Human magnetic resonance imaging at eight Tesla. *NMR Biomed.*, 1998, v. 11, 263–265.
41. Robitaille P.M.L., Abduljalil A.M., Kangarlu A. Ultra high resolution imaging of the human head at 8 Tesla: 2K × 2K for Y2K. *J Comp. Assist. Tomogr.*, 2000, v. 24, 2–7.
42. Robitaille P.M.L., Berliner L.J. (eds). Biological magnetic resonance: ultra high field magnetic resonance imaging. Springer, New York, 2006.
43. Liang Z.P., Lauterbur P.C. Principles of magnetic resonance imaging: a signal processing perspective. IEEE Press, New York, 2000.
44. Belliveau J.W., Kennedy Jr. D.N., McKinstry R.C., Buchbinder B.R., Weisskoff R.M., Cohen M.S., Vevea J.M., Brady T.J., Rosen B.R. Functional mapping of the human visual cortex by magnetic resonance imaging. *Science*, 1991, v. 254(5032), 716–9.
45. Ogawa S., Tank D.W., Menon R., Ellermann J.M., Kim S.G., Merkle H., Ugurbil K. Intrinsic signal changes accompanying sensory stimulation: functional brain mapping with magnetic resonance imaging. *Proc. Natl. Acad. Sci. USA*, 1992, v. 89(13), 5951–5.
46. Bandettini P.A., Jesmanowicz A., Wong E.C., Hyde J.S. Processing strategies for time-course data sets in functional MRI of the human brain. *Magn. Reson. Med.*, 1993, v. 30(2), 161–73.
47. Gaskell C.M., Klimek E.S. Variability of active galactic nuclei from the optical to X-Ray regions. *Astronom. Astrophys. Trans.*, 2003, v. 22(4–5), 661–679.
48. COBE web site, <http://lambda.gsfc.nasa.gov/product/cobe/>.
49. Robitaille P.M.L. NMR and the age of the Universe. *American Physical Society Centennial Meeting*, BC19.14, March 21, 1999.
50. Kirchhoff G. Ueber das Verhältnis zwischen dem Emissionsvermögen und dem Absorptionsvermögen der Körper für Wärme und Licht. *Annalen der Physik*, 1860, v. 109, 275–301.
51. Planck M. The theory of heat radiation. Philadelphia, PA., P. Blakiston's Son, 1914.
52. Robitaille P.M.L. On the validity of Kirchhoff's law of thermal emission. *IEEE Trans. Plasma Sci.*, 2003, v. 31(6), 1263–1267.
53. Robitaille P.M.L. An analysis of universality in blackbody radiation. *Progr. in Phys.*, 2006, v. 2, 22–23.
54. Planck M. Ueber das Gesetz der Energieverteilung im Normal-Spectrum. *Annalen der Physik*, 1901, v. 4, 553–563.

55. Stefan J. Ueber die Beziehung zwischen der Wärmestrahlung und der Temperatur. *Sitzungsberichte der mathematisch-naturwissenschaftlichen Classe der kaiserlichen Akademie der Wissenschaften*, Wien 1879, v. 79, 391–428.
 56. Wien W. Ueber die Energieverteilung in Emissionspektrum eines schwarzen Körpers. *Ann. Phys.*, 1896, v. 58, 662–669.
 57. Robitaille P.M.L. The MAP satellite: a powerful lesson in thermal physics. *Spring Meeting of the American Physical Society Northwest Section*, F4.004, May 26, 2001.
 58. Robitaille P.M.L. The collapse of the Big Bang and the gaseous Sun. *New York Times*, March 17, 2002.
 59. Robitaille P.M.L. WMAP: an alternative explanation for the dipole. *Fall Meeting of the American Physical Society Ohio Section*, E2.0001, 2006.
 60. Fixsen D.L., Gheng E.S., Gales J.M., Mather J.C., Shafer R.A., Wright E.L. The Cosmic Microwave Background spectrum from the full COBE FIRAS data set. *Astrophys. J.*, 1996, v. 473, 576–587.
 61. Klypin A.A., Strukov I.A., Skulachev D.P. The Relikt missions: results and prospects for detection of the Microwave Background Anisotropy. *Mon. Not. Astr. Soc.*, 1992, v. 258, 71–81.
 62. Robitaille P.M.L. On the origins of the CMB: insight from the COBE, WMAP and Relikt-1 satellites. *Progr. in Phys.*, 2007, v. 1, 19–23.
 63. Planck M. Scientific autobiography. Philosophical Library, New York, 1949.
-

On the Origins of the CMB: Insight from the COBE, WMAP, and Relikt-1 Satellites

Pierre-Marie Robitaille

Dept. of Radiology, The Ohio State University, 130 Means Hall, 1654 Upham Drive, Columbus, Ohio 43210, USA
E-mail: robitaille.1@osu.edu

The powerful “Cosmic Microwave Background (CMB)” signal currently associated with the origins of the Universe is examined from a historical perspective and relative to the experimental context in which it was measured. Results from the COBE satellite are reviewed, with particular emphasis on the systematic error observed in determining the CMB temperature. The nature of the microwave signal emanating from the oceans is also discussed. From this analysis, it is demonstrated that it is improper for the COBE team to model the Earth as a 285 K blackbody source. The assignment of temperatures to objects that fail to meet the requirements set forth in Kirchhoff’s law constitutes a serious overextension of the laws of thermal emission. Using this evidence, and the general rule that powerful signals are associated with proximal sources, the CMB monopole signal is reassigned to the oceans. In turn, through the analysis of COBE, WMAP, and Relikt-1 data, the dipole signal is attributed to motion through a much weaker microwave field present both at the position of the Earth and at the second Lagrange point.

1 Introduction

More than 40 years have elapsed since Penzias and Wilson first reported the existence of a thermal signal in the microwave region of the electromagnetic spectrum [1]. This measurement of the “Cosmic Microwave Background (CMB)” has been viewed as one of the most important in the history of science. Cosmology is now inextricably linked to its validity. Given this realization, it remains interesting that the logical steps first made by Penzias and Wilson [1] have not come under more considered review.

Penzias and Wilson [1] made the assumption that their signal was thermal in origin and inferred that the source could be treated as an ideal blackbody [2]. Without acknowledging the strict requirements involved in setting a blackbody temperature [2–4], they made recourse to the laws of thermal radiation, obtaining a temperature of 3.5 ± 1.0 K [1]. Although the cosmos can never meet the requirements for enclosure set forth by Kirchhoff [2], Dicke et. al. [5] would ultimately assign the signal to the average temperature of the Universe. Penzias and Wilson were thought to have discovered the “CMB”, a powerful signal bathing everything.

The COBE satellite [6–12] provided the most important confirmation of the thermal nature of the “CMB” [1]. This satellite is positioned at an elevation of ~ 900 km above sea level. COBE also reaffirmed the presence of a dipole signal presumably associated with motion of the local group. The dipole signature had been clearly observed by the Soviet Relikt-1 satellite [13], nearly 10 years earlier. Eventually, the WMAP satellite would affirm the existence of the dipole signal [14–16].

2 COBE and the assignment of temperatures

2.1 The “CMB” monopole

In acquiring the “CMB” signal [1], COBE produced a nearly perfect spectrum [11]. The signal to noise from the FIRAS instrument is exceedingly high. The error bars constitute a small fraction of the linewidth and must be expanded, by a factor of 400, to be visualized [11]. The validity of the absolute temperature was not questioned. The source responsible was thought to be at ~ 3 K. Soon, the “CMB” became the central experimental proof for the Big Bang [17].

It has always been understood, in communications, that powerful signals imply proximal sources. This practical knowledge was neglected [1, 5]. Yet, concerns should have lingered over the amount of power found in the “CMB” [1, 11]. In addition, the experimental justification, for setting blackbody temperatures, was overlooked. The belief, that blackbody radiation was universal [4], enabled the dismissal of all laboratory experiments relative to its nature [3].

The experimental [3] and theoretical [4] basis of universality has now been brought into question. Blackbody radiation is not universal in nature [4], but, rather, is strictly limited to a physical setting best approached by graphite and soot on Earth [3]. A spectrum, like the “CMB” signal [11], may well appear to be thermal, but the temperature will not be valid unless the requirements set forth in Kirchhoff’s experiment are strictly followed [3].

The Planckian equation [18] remains detached from the physical world. Thermal emission is explained mathematically [4], without regard to the physical setting. Blackbody radiation is the only process in physics wherein the setting,

transition species, and energy levels are devoid of physical meaning [3, 4]. In large part, this is a result of the erroneous belief in universality [3, 4]. Given universality, temperatures were set without the inconvenience of laboratory constraints.

2.2 The “CMB” dipole

In addition to the “CMB” monopole, the COBE satellite reports a dipole signature associated with motion [7], confirming Relikt-1 findings [13]. The WMAP satellite has also detected this dipole signal [19]. The dipole is thought to reflect a doppler phenomenon associated with motion of the local group. Based on COBE measurements, the dipole has an amplitude of 3.353 ± 0.024 mK in a direction $(l, b) = (264.26^\circ \pm 0.33^\circ, 48.22^\circ \pm 0.13^\circ)$, where l is the Galactic longitude and b , the latitude [15]. A nearly identical value, of 3.346 ± 0.017 mK in a direction $(l, b) = (263.85^\circ \pm 0.1^\circ, 48.25^\circ \pm 0.04^\circ)$, has been reported by the WMAP team [15]. Interestingly, the COBE satellite was able to determine a dipole value both from the DMR and the FIRAS instruments [6, 7]. The WMAP satellite is equipped solely with differential radiometers, and measures the dipole in a manner similar to the DMR on COBE [6, 14].

3 An alternative assignment for the “CMB” signals

3.1 Assignment of the monopole

During flight, the COBE satellite experienced an anomaly. “Most of the occurrences were in the High Frequency Region known as the South Atlantic Anomaly” [8]. Since the anomaly was produced over the Atlantic, it is interesting that the “CMB” results are devoid of interfering oceanic signals. The COBE team describes thermal instabilities when the limb of the Earth appears above the shield of the satellite. Data acquired during such events are discarded, but the COBE shield is not adequate to guard the instrumentation from the effects of being immersed in a scattered oceanic signal.

From the days of Penzias and Wilson [1], the Earth has not been considered as a powerful contaminating source for the “CMB”. The COBE team believes that the Earth can be modeled as a circular source of emission, with a radius of $\sim 61^\circ$ and a mean temperature of 285 K [9]. All scattering of microwave signals, by the atmosphere, is neglected. Whether the Penzias and Wilson signal [1] is measured from the ground, using balloons, or from COBE, the monopole signature is noticeably clean. However, based on the extent of the oceanic surface, and the known behavior of the oceans in the microwave, it is inappropriate to model the Earth as a 285 K source [21].

Water is a good absorber of microwave power. This forms the basis of practical microwave applications. In addition, submarine communications, at microwave frequencies,

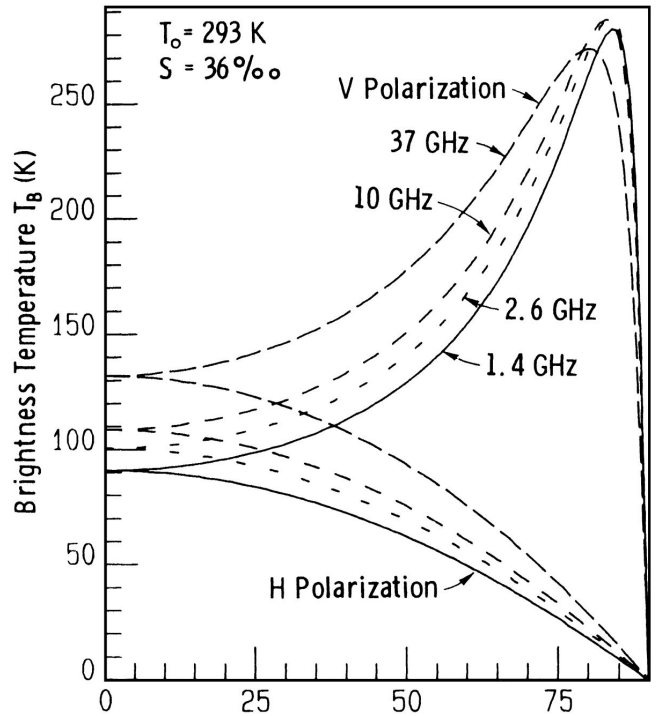


Fig. 1: Brightness temperature of a specular sea surface at 1.4, 2.6, 10, and 37 GHz. Note that when the angle of incidence approaches 90° , the brightness temperature of both the horizontal and vertical components falls to 0 K. As a result, the limb of the Earth appears as a source at nearly 0 K relative to COBE. The assumption that the Earth can be treated as a 285 K source is not valid. Reproduced by permission Figure 11.45 from F. T. Ulaby, R. K. Moore, A. K. Funk. Microwave remote sensing active and passive. — Volume 2: Radar remote sensing and surface scattering emission theory. Norwood (MA), Artech House, Inc., 1982. Copyright by Artech House, Inc., 1982.

are not possible while submerged, indicating powerful absorption. The oceans may be good absorbers of microwave power, but they are certainly not equal emitters. This is because liquids can never be in compliance with Kirchhoff's law [3, 20]. Liquids attempt to reach thermal equilibrium through conduction, thermal radiation, and convection. In fact, Planck has warned that objects, which sustain convection currents, can never be treated as blackbodies [20]. Nonetheless, it is unreasonable to believe that the oceans will be microwave silent on emission [21].

The behavior of oceanic emissions in the microwave is not simple (see Figure 1), depending significantly on the angle of observation [21]. The oceans cannot be treated as a blackbody source simply based on this fact [3]. Note that the brightness temperature of the oceans is dependent on the angle of incidence. Brightness temperatures with a 0° angle of incidence are less than 130 K over the frequency range spanning 1.4–37 GHz. For the vertical polarization, the brightness temperature increases to ~ 270 K, as the angle of incidence is raised from 0° to $\sim 75^\circ$. The brightness tempe-

rature of the vertical polarization then precipitously drops to 0 K. For the horizontal polarization, the brightness temperature falls gradually from 100 to 0 K, as the incidence angle is increased from 0° to 90°. The situation relative to oceanic emission in the microwave is much more complex than currently assumed by the COBE team [21].

When these facts are combined with atmospheric scattering, concerns linger that the measured “CMB” signal is devoid of Earthly interference. It would have been reassuring if the “CMB” experiments were being contaminated by an oceanic signal whose contributions could not be easily suppressed. Yet, the Penzias and Wilson signal [1, 11] was devoid of external interference. Conversely, oceanographic studies reveal that the seas can produce signals with a brightness temperature near 0 K, as demonstrated in Figure 1. Given the power observed in the monopole [1, 11], it is reasonable that the oceans cannot produce interference in the measurements since, in reality, *they constitute the source of the “CMB”* [22–25].

3.2 Assignment of the dipole

It is currently believed that the dipole signal is being produced by motion of the Relikt-1, COBE, or WMAP satellites through a powerful “CMB” monopole field ascribed to the Universe. However, a second situation exists. The satellites could be flowing through a field much weaker than that detected on Earth. In this scenario, the strong monopole field detected on Earth does not exist at the position of WMAP [59]. Using the data available, it should be possible to distinguish between these two alternatives.

3.3 Absolute measurements and error bars in the COBE satellite

The source of Penzias and Wilson signal [1] and its assignment to the “CMB” may be resolvable from Earth. In the first scenario, discussed in section 3.2, the contribution to the dipole arises strictly from the “CMB” monopole, thought to be of cosmic origin. In the second scenario, the “CMB” temperature would reflect two effects: (1) the motion of the Earth through the weak microwave field also present at the position of WMAP, and (2) the additional effect from the monopole generated by the Earth. In this case, when viewed from COBE, the “CMB” temperature measured by FIRAS, and direct calibration, would not necessarily agree with that determined through visualization of the dipole.

Using the FIRAS instrument, COBE initially reports the “CMB” monopole temperature as 2.730 ± 0.001 K [11]. This temperature should have been extremely reliable, since the FIRAS data have tremendous signal to noise [11]. Moreover, FIRAS was equipped with an external calibrator [8]. In Fixsen et al. [11] the “CMB” temperature obtained from the dipole is first reported as 2.717 ± 0.003 K. These uncertainties are at the 1σ level. “By choosing the monopole tempera-

ture as the point to evaluate $dB\nu/dT$ ”, the COBE team “has forced the dipole temperature to be that of the monopole” [7]. Despite this fact, the value of the “CMB” temperature, from the dipole measurement, is significantly lower than the value obtained from the monopole. The difference between these two numbers remains highly significant, even at the 99% confidence level. Considering the signal to noise using FIRAS, and the magnitude of the associated dipole, it is interesting that any systematic error exists. Such a dramatic divergence should not have been dismissed, especially since these two numbers might be expected to differ in the second scenario.

The COBE team also presents another method of assigning the “CMB” temperature, based on frequency calibration, using the CO and C⁺ lines [11]. This third method yields a temperature of 2.7255 ± 0.0009 K [11]. This value rests on factors outside the “CMB” and the dipole. While appearing to be even more precise, this value may be more prone to error and less accurate. The key determinations remain those from FIRAS, with external calibration, and from the dipole.

In Fixsen et. al [11], the COBE team recognizes that the “CMB” temperatures derived, from the monopole and from the dipole, are irreconcilable. They attribute the difference to systematic errors. In order to address this issue, the error bars on the dipole measure are arbitrarily raised to 0.007 [11]. All statistical significance is removed to account for systematic error arising from the galactic cut [11]. The inequality in these two numbers was later reexamined. In Mather et al. [12], the absolute value of the “CMB” temperature assigned using FIRAS, and the external calibrator, is shifted to 2.725 ± 0.002 K (2σ ; 95% confidence interval). The change is attributed to systematic errors in the calibrator [12]. Yet, in Fixsen et al. [11], the FIRAS measure was thought to be accurate to within 1 mK, based on pre-flight calibration. The new value for the “CMB” temperature, provided by FIRAS, of 2.725 ± 0.002 K (2σ ; 95% confidence interval), is now statistically different from the original value, of 2.730 ± 0.001 K (1σ), reported by the same instrument [11, 12].

The COBE FIRAS data has excellent signal to noise. Thus, it is troubling that a significant recalibration must be completed, nearly 10 years after launch. In the end, the prudent approach is to consider that the “CMB” temperatures, obtained from the monopole (2.730 ± 0.001 K at 1σ) and the dipole (2.717 ± 0.003 K at 1σ), are indeed significantly different, as initially reported. It is inappropriate to make so many adjustments for “systematic errors”, and thereby remove a highly significant difference between two numbers, long after completion of an experiment, especially given that COBE remains in orbit.

If the “CMB” signal truly originates for the Universe, the “CMB” temperatures evaluated, from the dipole and from FIRAS, with external calibration, must be identical. However, the values might be expected to be different in the second scenario, wherein the “CMB” arises from the Earth

and a much weaker field is present in the Universe. As a result, it appears that the COBE satellite provides the first evidence that the “CMB” monopole does indeed arise from the Earth. The systematic error, first detected by COBE in the dipole evaluation of the “CMB” temperature [11], may be, in actuality, the critical proof.

The European Space Agency is now in the final stages of preparation for launching the PLANCK satellite [26]. This satellite is also equipped to scan the sky in the microwave band. Unlike WMAP, the PLANCK instruments are not differential. Consequently, this satellite should be able to finally establish that the Penzias and Wilson signal [1] does indeed arise from the Earth. Once positioned at L2, PLANCK will fail to detect the monopole signal [1]. Instead, its instrument will report only the galactic signal, the variable sources, and the weak noisy background currently attributed to anisotropy.

4 Conclusions

When Penzias and Wilson used thermodynamic principles to set a temperature of 3.5 K, they did not consider the phases of matter [1]. The signal did not change with the seasons [1], and the Earth was not at ~ 3 K, so Dicke et al. [5] surmised that it originated from the Universe. A powerful spectrum was present, but the concept that the receiver must be close to the source was not considered. They believed, much like Planck [20], that the laws of thermal emission [18, 27, 28] were universally applicable. Yet, Kirchhoff’s law states that, for a blackbody, the temperature must be determined in the presence of thermal equilibrium, within an enclosure [2–4]. The Universe can never meet this requirement.

The oceans of the Earth cannot be treated as blackbodies, as demonstrated in Figure 1. The possibility should be considered that they are emitting at an apparent temperature, T_{app} , such that $T_{app} = T/\alpha$, where T corresponds to the real temperature and α is ~ 100 . Alpha may have a slight temperature or salinity dependence, since the Penzias and Wilson signal [1, 11] reflects a single spectrum. It is advanced that the apparent temperature, T_{app} , discussed above, corresponds to the ~ 3 K signature previously assigned to the Cosmos. Through this simple introduction of α and T_{app} , the laws of Planck [18], Wien [27], and Stefan [28] can be reformulated for our oceans. This is the case, even if the oceans can produce additional emissions, in the infrared band, or elsewhere. The inclusion of an apparent temperature solves a problem, but the temperature is no longer real. Condensed matter physics may benefit in dissecting the lattice behavior responsible for oceanic emissions. In doing so, they may discover the importance in thinking, like Planck [18], of physical oscillators [25].

In regard to the interaction of the oceanic monopole signal, produced by the Earth, and the dipole signal, produced

by motion through a weak microwave field of external origin, further insight may require the application of General Relativity [29].

It remains true that the temperature of the Universe can never be measured. That is a limitation given to us by Kirchhoff’s law [2–4]. The enclosure required by Kirchhoff, during the experimental characterization of blackbody radiation, cannot be removed. At the same time, Kirchhoff’s belief in universality is incorrect [3]. Indeed, this simple error will ultimately be viewed as the central oversight relative to the assignment of the Penzias and Wilson signal [1]. Kirchhoff erred 140 years ago relative to universality [3], and science failed to realize the profound implications [30]. There continues to be a lack of understanding relative to the fundamental experiments, which resulted in the laws of thermal radiation in general [18, 27, 28], and the complicating nature of liquids in particular.

Dedication

This work is dedicated to the memory of Charles-Auguste Robitaille.

First published online on November 01, 2006

References

1. Penzias A.A., Wilson R.W. A measurement of excess antenna temperature at 4080 Mc/s. *Astrophys. J.* 1965, v. 1, 419–421.
2. Kirchhoff G. Ueber das Verhältnis zwischen dem Emissionsvermögen und dem absorptionsvermögen der Körper für Waeme und Licht. *Annalen der Physik*, 1860, v. 109, 275–301.
3. Robitaille P.M.L. On the validity of Kirchhoff’s law of thermal emission. *IEEE Trans. Plasma Sci.*, 2003, v. 31(6), 1263–1267.
4. Robitaille P.M.L. An analysis of universality in blackbody radiation. *Progr. in Phys.*, 2006, v. 2, 22–23.
5. Dicke R.H., Peebles P.J.E., Roll P.G., and Wilkinson D.T. Cosmic black-body radiation. *Astrophys. J.* 1965, v. 1, 414–419.
6. COBE web site, <http://lambda.gsfc.nasa.gov/product/cobe/>.
7. Fixsen D.J., Cheng E.S., Cottingham D.A., Eplee R.E., Isaacman R.B., Mather J.C., Meyer S.S., Noerdlinger P.D., Shafer R.A., Weiss R., Wright E.L., Bennett C.L., Boggess N.W., Kellsall T., Moseley S.H., Silverberg R.F., Smoot G.F., Wilkinson D.T. Cosmic Microwave Dipole spectrum measured by the COBE FIRAS Instrument. *Astroph. J.*, 1994, v. 420, 445–449.
8. Fixsen D.J., Cheng E.S., Cottingham D.A., Eplee R.E., Hewagama T., Isaacman R.B., Jensen K.A., Mather J.C., Massa D.L., Meyer S.S., Noerdlinger P.D., Read S.M., Rosen L.P., Shafer R.A., Trenholme A.R., Weiss R., Bennett C.L., Boggess N.W., Wilkinson D.T., Wright E.L. Calibration of the COBE FIRAS instrument. *Astrophys. J.*, 1994, v. 420, 457–473.
9. Bennett C.L., Kogut A., Hinshaw G., Banday A.J., Wright E.L., Gorski K.M., Wilkinson D.T., Weiss R., Smoot G.F., Meyer S.S., Mather J.C., Lubin P., Loewenstein K., Lineweaver C., Keegstra P., Kaita E., Jackson P.D., Cheng E.S.

- Cosmic temperature fluctuations from two years of COBE differential microwave radiometers observations. *Astrophys. J.*, 1994, v. 436, 423–442.
10. Kogut A., Smoot G.F., Bennett C.L., Wright E.L., Aymon J., de Amici G., Hinshaw G., Jackson P.D., Kaita E., Keegstra P., Lineweaver C., Loewenstein K., Rokke L., Tenorio L., Boggess N.W., Cheng E.S., Gulkis S., Hauser M.G., Janssen M.A., Kelsall T., Mather J.C., Meyer S., Moseley S.H., Murdock T.L., Shafer R.A., Silverberg R.F., Weiss R., Wilkinson D.T. COBE differential microwave radiometers — preliminary systematic error analysis. *Astrophys. J.*, 1992, v. 401, 1–18.
 11. Fixsen D.L., Gheng E.S., Gales J.M., Mather J.C., Shafer R.A., Wright E.L. The Cosmic Microwave Background spectrum from the full COBE FIRAS data set. *Astrophys. J.*, 1996, v. 473, 576–587.
 12. Mather J.C., Fixsen D.J., Shafer R.A., Mosier C., Wilkinson D.T. Calibrator design for the COBE Far-Infrared Absolute Spectrophotometer (FIRAS). *Astrophys. J.*, 1999, v. 512, 511–520.
 13. Klypin A.A., Strukov I.A., Skulachev D.P. The Relikt missions: results and prospects for detection of the Microwave Background Anisotropy. *Mon. Not. Astr. Soc.*, 1992, v. 258, 71–81.
 14. WMAP website, <http://map.gsfc.nasa.gov/>.
 15. Bennett C.L., Halpern M., Hinshaw G., Jarosik N., Kogut A., Limon M., Meyer S.S., Page L., Spergel D.N., Tucker G.S., Wollack E., Wright E.L., Barnes C., Greason M.R., Hill R.S., Komatsu E., Nolta M.R., Odegard N., Peiris H.V., Verde L., Weiland J.L. First-year Wilkinson Microwave Anisotropy Probe (WMAP) observations: preliminary maps and basic results. *Astrophys. J. Suppl.*, 2003, v. 148(1), 1–27.
 16. Hinshaw G., Nolta M.R., Bennett C.L., Bean R., Dore O., Greason M.R., Halpern M., Hill R.S., Jarosik N., Kogut A., Komatsu E., Limon M., Odegard N., Meyer S.S., Page L., Peiris H.V., Spergel D.N., Tucker G.S., Verde L., Weiland J.L., Wollack E., Wright E.L. Three-year Wilkinson Microwave Anisotropy Probe (WMAP) observations: temperature analysis. *Astrophys. J.*, 2006, submitted.
 17. Berger A. An introduction to the International Symposium George Lemaître. In: *The Big Bang and George Lemaître*, D. Reidel Publishing Company, Dordrecht, 1984, p. vii–xiv.
 18. Planck M. Ueber das Gesetz der energieverteilung in Normalspectrum. *Annalen der Physik*, 1901, v. 4, 553–563.
 19. Robitaille P.M.L. WMAP: a radiological analysis. *Progr. in Phys.*, 2007, v. 1, 3–18.
 20. Planck M. The theory of heat radiation. Philadelphia, PA., P. Blakiston's Son, 1914.
 21. Ulaby F.T., Moore R.K., Fung A.K. Microwave remote sensing active and passive — Volume 2: Radar remote sensing and surface scattering and emission theory. London, Addison-Wesley Publishing Company, 1982, p. 880–884.
 22. Robitaille P.M.L. NMR and the Age of the Universe. *American Physical Society Centennial Meeting*, BC19.14, March 21, 1999.
 23. Robitaille P.M.L. The MAP satellite: a powerful lesson in thermal physics. *Spring Meeting of the American Physical Society Northwest Section*, F4.004, May 26, 2001.
 24. Robitaille P.M.L. The collapse of the Big Bang and the gaseous Sun. *New York Times*, March 17, 2002.
 25. Robitaille P.M.L. WMAP: an alternative explanation for the dipole. *Fall Meeting of the American Physical Society Ohio Section*, E2.0001, 2006.
 26. PLANCK website, <http://www.rssd.esa.int/index.php?project=PLANCK&page=index>.
 27. Wien W. Ueber die Energieverteilung in Emissionspektrum eines schwarzen Körpers. *Ann. Phys.*, 1896, v. 58, 662–669.
 28. Stefan J. Ueber die Beziehung zwischen der Wärmestrahlung und der Temperatur. *Sitzungsberichte der mathematisch-naturwissenschaftlichen Classe der kaiserlichen Akademie der Wissenschaften*, Wien 1879, v. 79, 391–428.
 29. Rabounski D. The relativistic effect of the deviation between the CMB temperatures obtained by the COBE satellite *Progr. in Phys.*, 2007, v. 1, 24–26.
 30. Robitaille P.M.L. The Solar photosphere: evidence for condensed matter. *Progr. in Phys.*, 2006, v. 2, 17–21.

The Relativistic Effect of the Deviation between the CMB Temperatures Obtained by the COBE Satellite

Dmitri Rabounski

E-mail: rabounski@yahoo.com

The Far-Infrared Absolute Spectrophotometer (FIRAS) on the COBE satellite, gives different temperatures of the Cosmic Microwave Background. This deviation has a theoretical explanation in the Doppler effect on the dipole (weak) component of the radiation, the true microwave background of the Universe that moves at 365 km/sec, if the monopole (strong) component of the radiation is due to the Earth. Owing to the Doppler effect, the dipole radiation temperature (determined by the 1st derivative of the monopole) is lower than the monopole radiation temperature, with a value equal to the observed deviation. By this theory, the WMAP and PLANCK satellites, targeting the L2 point in the Sun-Earth-Moon system, should be insensitive to the monopole radiation. In contrast to the launched WMAP satellite, the PLANCK satellite will have on board absolute instruments which will not be able to detect the measured temperature of the Cosmic Microwave Background. That the monopole (strong) component of the observed Cosmic Microwave Background is generated by the Earth is given a complete theoretical proof herein.

The COBE satellite, launched in 1989, has on board two instruments targeting the temperature of the Cosmic Microwave Background (CMB), namely the Far-Infrared Absolute Spectrophotometer (FIRAS) and the Differential Microwave Radiometer (DMR). FIRAS, having just a single channel for a signal, is sensitive to both the strong (monopole) and weak (dipole) components of the Background Radiation, and measures the general temperature in the Background without distinction between the monopole and dipole components of the field. The DMR has another construction: having a few channels for a signal, the DMR recognizes only the difference between the signals in the channels, and so gives just a difference between the temperature of the Background in the different directions. In other words, the DMR is sensitive to only the weak (dipole) component of the field that provides a possibility of direct search for its anisotropy [1].

The WMAP satellite launched in 2001 has on board only differential instruments working similarly to the DMR on COBE, so its data accounts only for the weak (dipole) component of the Background [2].

The anisotropy in the Background measured by the differential instruments is actually the same: DMR at COBE registered the anisotropy 3.353 ± 0.024 mK, while WMAP gave 3.346 ± 0.017 mK. The main direction of the anisotropy, by COBE, is $l = 264.26^\circ \pm 0.33^\circ$, $b = 48.22^\circ \pm 0.13^\circ$ (l is the Galactic longitude, b is the Galactic latitude). WMAP gives $l = 263.85^\circ \pm 0.1^\circ$, $b = 48.25^\circ \pm 0.04^\circ$ [3].

The absolute temperature of the Background initially obtained from the direct measurement by FIRAS

$$T_{\text{FIRAS}} = T_0 = 2.730 \pm 0.001 \text{ K},$$

is the undifferentiated temperature of the monopole and dipole components of the field. However, the COBE team also

extracted the absolute temperature from the 1st derivative of the monopole, which was interpreted as the actual temperature of the dipole component of the field. They obtained another numerical value [4]

$$T = 2.717 \pm 0.003 \text{ K},$$

so the average deviation $\Delta T = 0.013$ K between these two results is a dozen times bigger than the measurement precision. So we have a minimal relative deviation between the CMB temperature by FIRAS from the monopole and from the 1st derivative of the monopole

$$\Delta T/T_0 = 0.33\% \text{ at } 1\sigma,$$

$$\Delta T/T_0 = 0.18\% \text{ at } 2\sigma,$$

which is small number, but is significantly not zero. So the CMB temperature measured by FIRAS from the monopole and its 1st derivative aren't the same. This is a systematic deviation with many years of the COBE observations. The COBE team attempted to explain the deviation as systematic errors in the calibration of the instruments. However, as pointed out by Robitaille [5], so large an increase of σ supposed by the COBE team is unlikely for the FIRAS instrument, which has excellent signal to noise ratio. The systematic deviation shouldn't be removed from the consideration.

As pointed out by Robitaille [5], this systematic deviation has no chance of being explained by anything other than the fact that the monopole and dipole components of the Background have *different origins*. He has elucidated the similarity of the Cosmic Microwave Background Radiation with radiation of Earth origin. He supposed that the monopole field has a different origin to that of the dipole, and is due to the Earth, not the whole Universe. According to

Robitaille [5, 6], the monopole (strong) field, is nothing but that generated by Earth objects (mostly oceans) and moves, in common with the Earth, with respect to the dipole (weak) field which is the real microwave background of the Universe.

Robitaille's claim, obtained from purely experimental analysis, can be easily checked by the relativistic effects which should appear in the COBE measurements, if the monopole field moves, in common with the Earth, with respect to the dipole field related to the whole Universe.

It follows from the measurement that the COBE satellite, in unison with the Earth, moves relative to the Cosmic Microwave Background with a velocity of 365 ± 18 km/sec [7]. DMR is sensitive to only the dipole field, so we are sure of the velocity with respect to the dipole field.

If the monopole field is due to the Earth, the COBE satellite is at rest with respect to the monopole field, but moves, in common with the Earth, at 365 ± 18 km/sec relative to the dipole field which is the true microwave background of the Universe. In such a case, two kinds of relativistic effects should appear for COBE: (1) the effects caused by the relative motion with respect to the dipole field (the Doppler effect and the effect of Special Relativity); (2) the effects caused by the physical properties of the local space of the COBE-bound observer, such as the presence of the Earth's gravitational field, and also the space rotation due to the daily rotation of the Earth (the effects of General Relativity).

By the Doppler effect, the temperature T of a radiation, the source of which moves with a velocity v at an angle θ relative to the direction from the observer to the source, differs from the same radiation's temperature T_0 measured when its source is at rest: $T = \frac{T_0}{1 + \frac{v}{c} \cos \theta}$. Assuming that the source of the dipole radiation moves with $v = 365 \pm 18$ km/sec away from the observer and the Earth (the monopole radiation source), we obtain

$$\frac{\Delta T}{T_0} = \frac{T_0 - T}{T_0} = \frac{v}{c} = 0.12\% \pm 0.006\%$$

i.e., due to the Doppler effect, the dipole radiation temperature T (measured by the 1st derivative of the monopole) should be 0.12% smaller than the monopole radiation temperature T_0 (measured by FIRAS).

This theoretical result is very close to the 0.18% registered at 2σ . In the real situation, this coincidence can be accounted for if one takes into account that fact that the COBE team provided different data for the dipole-measured temperature [5]. So the relativistic lowering of the Cosmic Microwave Background temperature due to the Doppler effect on its dipole component, the source of which moves away from the Earth (the source of the monopole), is in good agreement with that observed by COBE.

Now consider the effect of Special Relativity. It is well known [8], that the temperature T of radiation, the source of

which moves relative to the observer with a velocity v , is: $T = T_0 \sqrt{1 - \frac{v^2}{c^2}}$. With $v = 365$ km/sec we obtain the relativistic lowering of the observed temperature of the dipole radiation due to the Special Relativity effect

$$\frac{\Delta T}{T_0} = \frac{T_0 - T}{T_0} = 7.4 \times 10^{-7} = 0.000074\%,$$

that is inconsequentially small for $\frac{\Delta T}{T_0} = 0.12\%$ produced by the Doppler effect, and really registered by COBE. So there is no essential rôle played by Special Relativity in the relativistic lowering of the dipole radiation temperature.

The effects of General Relativity can also be examined. By General Relativity, if the monopole radiation is due to the Earth, it is affected by the gravitation and rotation of the Earth's space so that the temperature of the monopole radiation is as well higher than the dipole radiation far away from the Earth. It has been obtained that the temperature deviation between the monopole and dipole radiations expects to be $\sim 10^{-8}\%$.

The effects caused by the COBE satellite itself (its own mass and spin), were a few orders smaller than the above effects caused by the Earth. The values are also inconsequentially small for 0.12% produced by the Doppler effect, and observed by COBE. So General Relativity's rôle in the relativistic lowering of the dipole radiation temperature is infinitesimal.

The General Relativity effects are bulky for deduction and calculation. For this reason the calculations for these effects are not presented in this paper.

We therefore conclude that:

The different temperature of the Cosmic Microwave Background measured by the FIRAS instrument of COBE has a theoretical explanation in the Doppler effect on the dipole (weak) component of the radiation, the true microwave background of the Universe that moves away at 365 km/sec from the monopole (strong) component of the radiation due to the Earth. Owing to the Doppler effect, the CMB radiation temperature, measured by the 1st derivative of its monopole component, is lower than the monopole radiation temperature directly measured by FIRAS. This important finding can be referred to as **a relativistic effect of the deviation between the temperature of the monopole and dipole components of the Cosmic Microwave Background**.

The calculation herein provides the theoretical proof of the assertion that the monopole component of the Cosmic Microwave Background is due to the Earth. If so, the WMAP satellite, located far away from the Earth, at the Lagrange 2 (L2) point in the Earth-Moon system, should be insensitive to the monopole radiation. Its instruments should register only the dipole radiation from the Universe. Therefore, the absolute and differential instruments located at the L2 point

should manifest no difference in the measured temperature of the radiation.

The WMAP satellite, unfortunately, has on board only the differential instruments (working like the DMR on COBE). However the PLANCK satellite, which will soon be launched, has on board absolute instruments. PLANCK will also be located at the L2 point, so its absolute instruments should be unable to register any signal from the monopole origination (from the Earth). This is in contrast to COBE, located near the Earth.

The above theoretical calculation and the measurement by COBE are the complete theoretical and experimental proofs of the assertion that the monopole (strong) component of the Cosmic Microwave Background is derived from the Earth, while the dipole (weak) component is the true microwave background of the Universe relative to which the Earth moves with a velocity of 365 km/sec. Due to the theoretical and experimental proofs, we expect to have a profoundly altered understanding of the Cosmic Microwave Background.

I am very thankful to Professor Pierre-Marie Robitaille who turned my attention to the systematic deviation in the Cosmic Microwave Background temperature by the FIRAS instrument on the COBE satellite, and spent much time to explain to me the details of the experiment.

*First published online on November 01, 2006
Corrections posted online on December 30, 2006*

References

1. Boggess N.W., et al. The COBE mission: its design and performance two years after launch. *Astrophys. J.*, 1992, v. 397, 420–429. v. 397, 420–429.
2. Bennett C.L., et al. The Microwave Anisotropy Probe mission. *Astrophys. J.*, 2003, v. 583(1), 1–23.
3. Bennett C.L., et al. First-year Wilkinson Microwave Anisotropy Probe (WMAP) observations: preliminary maps and basic results. *Astrophys. J. Suppl. Ser.*, 2003, v. 148(1), 1–27.
4. Fixsen D.J., et al. The Cosmic Microwave Background spectrum from the full COBE FIRAS data set. *Astrophys. J.*, 1996, v. 473, 576–587.
5. Robitaille P.-M. On the origins of the CMB: insight from the COBE, WMAP and Relikt-1 satellites. *Progress in Physics*, 2007, v. 1, 19–23.
6. Robitaille P.-M. WMAP: a radiological analysis. *Progress in Physics*, 2007, v. 1, 3–18.
7. Smoot G.F., et al. Preliminary results from the COBE differential microwave interferometers: large angular scale isotropy of the Cosmic Microwave Background. *Astrophys. J.*, 1991, v. 371, L1–L5.
8. Tolman R.C. The theory of the relativity of motion. University of California Press, Berkeley, 1917 (reprinted by Dover Phoenix Editions, 2004).

Momentum of the Pure Radiation Field

Bo Lehnert

*Alfvén Laboratory, Royal Institute of Technology, S-10044, Stockholm, Sweden
E-mail: Bo.Lehnert@ee.kth.se*

The local momentum equation of the pure radiation field is considered in terms of an earlier elaborated and revised electromagnetic theory. In this equation the contribution from the volume force is found to vanish in rectangular geometry, and to become nonzero but negligible in cylindrical geometry. Consequently the radiated momentum is due to the Poynting vector only, as in conventional electrodynamics. It results in physically relevant properties of a photon model having an angular momentum (spin). The Poynting vector concept is further compared to the quantized momentum concept for a free particle, as represented by a spatial gradient operator acting on the wave function. However, this latter otherwise successful concept leads to difficulties in the physical interpretation of known and expected photon properties such as the spin, the negligible loss of transverse momentum across a bounding surface, and the Lorentz invariance.

1 Introduction

In the original and current presentation of Quantum Electrodynamics, the Poynting vector forms a basis for the quantized momentum of the pure radiation field [1, 2]. Thereby Maxwell's equations with a vanishing electric field divergence in the vacuum state are used to determine the electromagnetic field strengths and their potentials which, in their turn, are expressed by sets of quantized plane waves.

In the deduction of the Schrödinger equation, the quantized momentum for a free particle with mass has on the other hand been represented by an operator acting on the wave function and including a spatial gradient [1].

Since the individual photon can appear both as a wave and as a particle, the question may be raised whether its momentum should be represented by the Poynting vector concept, or by the spatial gradient operator concept. This question is discussed and illustrated in the present paper, in terms of a revised electromagnetic theory described in a recent review [3]. A summary of the basic equations of the theory is presented in Section 2, followed by two simple examples in Section 3 on a slab-shaped dense photon beam and on an axisymmetric model of the individual photon. A comparison between the two momentum concepts is finally made in Section 4.

2 Basic equations of the revised theory

The zero-point-energy of the vacuum state, its related electromagnetic vacuum fluctuations, the Casimir effect, and the electron-positron pair formation out of the vacuum support the hypothesis of a local electric charge density and an associated nonzero electric field divergence in such a state. On account of this, a Lorentz and gauge invariant theory has been elaborated, the details of which are given elsewhere

[3–8]. The basic equations for the electric and magnetic fields \mathbf{E} and \mathbf{B} become

$$\text{curl } \mathbf{B} / \mu_0 = \epsilon_0 (\text{div } \mathbf{E}) \mathbf{C} + \epsilon_0 \partial \mathbf{E} / \partial t, \quad (1)$$

$$\text{curl } \mathbf{E} = -\partial \mathbf{B} / \partial t, \quad (2)$$

$$\text{div } \mathbf{E} = \bar{\rho} / \epsilon_0. \quad (3)$$

Here $\bar{\rho}$ is the local electric charge density in the vacuum, ϵ_0 and μ_0 are the conventional dielectric constant and magnetic permeability of the vacuum, $c^2 = 1/\mu_0 \epsilon_0$, and $\mathbf{C}^2 = c^2$ results from the Lorentz invariance where \mathbf{C} has the character of a velocity vector. Combination of equations (1) and (2) yields the extended wave equation

$$\left(\frac{\partial^2}{\partial t^2} - c^2 \nabla^2 \right) \mathbf{E} + \left(c^2 \nabla + \mathbf{C} \frac{\partial}{\partial t} \right) (\text{div } \mathbf{E}) = 0 \quad (4)$$

for the electric field, and the associated relation

$$\left(\frac{\partial}{\partial t} + \mathbf{C} \cdot \nabla \right) (\text{div } \mathbf{E}) = 0 \quad (5)$$

provided that $\text{div } \mathbf{C} = 0$ which is an adopted restriction henceforth.

Using known vector identities, the basic equations (1), (2), and (3) result in the local momentum equation

$$\text{div}^2 \mathbf{S} = \mathbf{f} + \frac{\partial}{\partial t} \mathbf{g}, \quad (6)$$

where ${}^2 \mathbf{S}$ is the electromagnetic stress tensor,

$$\mathbf{f} = \bar{\rho} \mathbf{E}' \quad \mathbf{E}' = \mathbf{E} + \mathbf{C} \times \mathbf{B} \quad (7)$$

is the local volume force density, and

$$\mathbf{g} = \epsilon_0 \mathbf{E} \times \mathbf{B} = \frac{1}{c^2} \mathbf{S} \quad (8)$$

can be interpreted as a local electromagnetic momentum density of the radiation field, with \mathbf{S} standing for the Poynting vector. Likewise a local energy equation

$$-\operatorname{div} \mathbf{S} = \bar{\rho} \mathbf{E} \cdot \mathbf{C} + \frac{1}{2} \epsilon_0 \frac{\partial}{\partial t} (\mathbf{E}^2 + c^2 \mathbf{B}^2) \quad (9)$$

is obtained. It is here to be observed that equations (6) and (9) are rearranged relations which do not provide more information than the original basic equations.

In the examples to be considered here, a velocity vector of the form

$$\mathbf{C} = c(0, \cos \alpha, \sin \alpha) \quad (10)$$

is adopted, either in a rectangular frame (x, y, z) or in a cylindrical frame (r, φ, z) . All field quantities are assumed to vary with t and z as $\exp[i(-\omega t + kz)]$ where ω and k are the corresponding frequency and wave number of an elementary normal mode. Equation (5) then results in the dispersion relation

$$\omega = kv \quad v = c(\sin \alpha). \quad (11)$$

In order not to get in conflict with observations, such as those due to the Michelson-Morley experiments, the analysis is restricted to the condition

$$0 < \cos \alpha \equiv \delta \ll 1. \quad (12)$$

With a smallness parameter $\delta \leq 10^{-4}$, the difference between v and c would become less than a change in the eight decimal of c .

3 Normal modes in slab-shaped and axisymmetric geometries

The first example is given by a slab-shaped dense light beam. The beam propagates in the z -direction of a rectangular frame (x, y, z) , has a core region defined by $-a < x < a$, and two narrow boundary regions at $-b < x < -a$ and $a < x < b$. Within the core there is a homogeneous conventional electromagnetic wave field. This field is matched to the electromagnetic field in the inhomogeneous boundary regions as shown elsewhere [3, 8]. The analysis is here restricted to these regions within which the inhomogeneity in the x -direction requires the revised field equations to be used. In an analogous beam of circular cross-section, the source of angular momentum becomes localized to a corresponding inhomogeneous boundary region [3, 8].

The wave equation (4) now results in the relations

$$E_x = -(i/k\delta^2) \frac{\partial E_z}{\partial x}, \quad (13)$$

$$E_y = -(\sin \alpha) E_z / \delta, \quad (14)$$

where the field E_z plays the rôle of a generating function for the components E_x and E_y . From equation (2) the magnetic

field components become

$$B_x = -E_y / c(\sin \alpha), \quad (15)$$

$$B_y = E_x / c(\sin \alpha) + \frac{i}{k c(\sin \alpha)} \frac{\partial E_z}{\partial x} = (\sin \alpha) E_x / c, \quad (16)$$

$$B_z = -\frac{i}{k c(\sin \alpha)} \frac{\partial E_y}{\partial x} = -\delta E_x / c. \quad (17)$$

Insertion of relations (13)–(17) into the expression (7) for the volume force then yields $\mathbf{E}' = 0$.

Further turning to the momentum density (8) of the radiation field, relations (13)–(17) give

$$g_x = 0, \quad (18)$$

$$g_y = \delta \epsilon_0 [E_x^2 + E_y^2 / (\sin \alpha)^2] / c, \quad (19)$$

$$g_z = \epsilon_0 [E_x^2 + E_y^2 / (\sin \alpha)^2] / c. \quad (20)$$

Finally the power term in the energy equation (9) vanishes because relations (10), (13), and (14) combine to

$$\mathbf{E} \cdot \mathbf{C} = 0. \quad (21)$$

This example thus demonstrates the following features:

- The volume force density \mathbf{f} vanishes in rectangular geometry.
- The momentum density \mathbf{g} of the radiation field has a primary component g_z in the direction of propagation.
- There is a secondary component g_y of the order δ , directed along the boundary and being perpendicular to the direction of propagation. This component corresponds to that which generates angular momentum (spin) in cylindrical geometry.
- There is a vanishing component g_x and no momentum is flowing across the boundary of the beam.
- The local power term in the energy equation vanishes.

The second example concerns an axisymmetric model of the individual photon. A wave or a wave packet of preserved and limited geometrical shape and undamped motion in a defined direction has then to be taken as a starting point. This leads to cylindrical geometry with propagation along z in a frame (r, φ, z) . From earlier deductions based on equations (1)–(5), the electric and magnetic field components of an elementary normal mode then become [3–6]

$$E_r = -i g_0 R_5 / \theta, \quad (22)$$

$$E_\varphi = g_0 \delta (\sin \alpha) R_3, \quad (23)$$

$$E_z = g_0 \delta^2 R_4 \quad (24)$$

and

$$B_r = -E_\varphi / c(\sin \alpha) = -g_0 \delta R_3 / c, \quad (25)$$

$$B_\varphi = E_r (\sin \alpha) / c = -i g_0 (\sin \alpha) R_5 / \theta c, \quad (26)$$

$$B_z = -i g_0 \delta R_8 / \theta c. \quad (27)$$

Here we have introduced $g_0 = G_0/\delta^2$ where G_0 is the characteristic amplitude of a normalized generating function G , $\theta = kr_0$ with r_0 as a characteristic radial length, and

$$R_3 = \rho^2 DG \quad R_4 = 1 - R_3 \quad (28)$$

$$R_5 = \frac{\partial}{\partial \rho} R_4 \quad R_8 = \left(\frac{\partial}{\partial \rho} + \frac{1}{\rho} \right) R_3 \quad (29)$$

with $\rho = r/r_0$ and the operator D given by

$$D = \frac{\partial^2}{\partial \rho^2} + \frac{1}{\rho} \frac{\partial}{\partial \rho} - \theta^2 \delta^2. \quad (30)$$

For the electric field \mathbf{E}' the components now reduce to

$$E'_r = -ig_0 \delta^2 (R_5 + R_8) / \theta \quad (31)$$

$$E'_\varphi = 0, \quad (32)$$

$$E'_z = g_0 \delta^2 (R_3 + R_4) \quad (33)$$

and the momentum components of the radiation field are given by

$$cg_r/\epsilon_0 g_0^2 = i\delta^2 (\sin \alpha) (R_4 R_5 - R_3 R_8) / \theta, \quad (34)$$

$$cg_\varphi/\epsilon_0 g_0^2 = \delta R_5 R_8 / \theta^2 - \delta^3 R_3 R_4, \quad (35)$$

$$cg_z/\epsilon_0 g_0^2 = -(\sin \alpha) R_5^2 / \theta^2 + \delta^2 (\sin \alpha) R_3^2. \quad (36)$$

Finally the power term in the energy equation (9) becomes

$$\bar{\rho} \mathbf{E} \cdot \mathbf{C} = \delta^2 \bar{\rho} c g_0 (\sin \alpha) (R_3 + R_4) \quad (37)$$

thus being of second order in the parameter δ .

To the first order in δ the axisymmetric geometry then has features being analogous to those of the slab-shaped geometry:

- There is a negligible contribution from the volume force density \mathbf{f} , as well as from the radial component g_r of the radiation field.
- A secondary component g_φ of order δ gives rise to a spin of the photon model [3].
- The power term in the energy equation is negligible.

A corresponding analysis of a non-axisymmetric photon model with periodic φ -dependence and screw-shaped geometry leads to similar results [7].

The total(net) electric charge and magnetic moment of the present photon models have finally been shown to vanish through spatial integration [5–7].

4 Comparison between the momentum concepts

In the spatial gradient concept the momentum is represented by the operator

$$\mathbf{p} = -i\hbar \nabla. \quad (38)$$

For the normal modes being considered here, the corre-

sponding axial component reduces to

$$p_z = \hbar k = h/\lambda = h\nu/c \quad (39)$$

which in conventional theory becomes related to a photon of energy $h\nu$, moving along z at the velocity c of light.

A comparison between the concepts of equations (8) and (38) is now made in respect to the remaining components being perpendicular to the direction of propagation, as well as in respect to the related question about Lorentz invariance.

4.1 The transverse component directed across a confining boundary

As compared to the axial component g_z , the momentum density \mathbf{g} has a vanishing component g_x in slab-shaped geometry, and a nonzero but negligible component g_r in axisymmetric geometry. The corresponding relations between the momentum p_z and the components p_x and p_r are in a first approximation represented by

$$|p_x/p_z| \cong \lambda/2\pi L_x, \quad |p_r/p_z| \cong \lambda/2\pi L_r \quad (40)$$

with L_x and L_r as corresponding characteristic lengths. Then the transverse components p_x and p_r cannot generally be neglected. This becomes questionable from the physical point of view when considering individual photons and light beams which have no transverse losses of momentum.

4.2 The transverse component directed along a confining boundary

With vanishing derivatives $\partial/\partial y$ or $\partial/\partial \varphi$, along a boundary in rectangular geometry or around the axis in cylindrical geometry, there are components g_y and g_φ being related to a nonzero spin. This behaviour differs from that of the momentum \mathbf{p} for which the components p_y and p_φ vanish, as well as the spin. Such a behaviour appears to lack physical explanation.

When there are nonvanishing derivatives $\partial/\partial y$ and $\partial/\partial \varphi$, the concepts of \mathbf{g} and \mathbf{p} both result in transverse components along a boundary, but being of different forms.

4.3 The Lorentz invariance

In the present revised Lorentz invariant theory on the photon model, there is a component of the momentum \mathbf{g} around the axis. This provides a spin, at the expense of the axial velocity of propagation. The latter then has to become slightly less than c , as required by the dispersion relation (11).

With the definition (38) of the momentum \mathbf{p} , there is a different situation. Thus equation (39) is in conventional theory consistent with an individual photon that moves at the full velocity c along the axial direction. But for the same photon also to possess a nonzero spin, it should have an additional transverse momentum p_φ , with an associated

velocity v_ϕ which circulates around the z -axis. For a radiation field within the volume of the photon to be considered as a self-consistent entity, the total local velocity then becomes equal to $(c^2 + v_\phi^2)^{1/2} > c$. This would represent a superluminal field configuration not being Lorentz invariant.

5 Conclusions

As expressed in terms of the present revised electromagnetic theory, the momentum concept of the pure radiation field appears to be physically relevant. The corresponding volume force density thus vanishes in rectangular geometry and is nonzero but negligible in cylindrical geometry. The momentum density is represented by the Poynting vector, as in conventional theory. Thereby its transverse components become consistent with the spin of the photon, and with a negligible loss of transverse momentum across a bounding surface.

The spatial gradient operator concept for the quantized momentum of a free particle with mass has earlier been used with success in the Schrödinger equation. However, when applying this concept to the free radiation field of the individual photon or of dense light beams, the obtained results differ from those based on the Poynting vector, and are in some cases difficult to interpret from the physical point of view. This discrepancy requires further investigation.

In this connection it should finally be mentioned that the present axisymmetric photon model [3, 6] is radially polarized. The core of a dense light beam being treated earlier [8] consists on the other hand of a linearly polarized conventional electromagnetic wave, with a boundary region having a radial gradient and leading to a spin of the beam considered as an entity.

The theory of this latter model can as well be applied to the limit of an individual photon with a linearly polarized core, a boundary region of finite radial extension, and a nonzero spin. It should thereby be kept in mind that such a model concerns the internal structure of a single photon, and therefore does not deal with the entangled quantum states of two interacting photons.

References

1. Schiff L. I. Quantum Mechanics. McGraw-Hill Book Comp. Inc., New York, 1949, Ch. XIV, Ch. II.
2. Heitler W. The quantum theory of radiation. Third edition. Clarendon Press, Oxford, 1954, Ch. II.
3. Lehnert B. Photon physics of revised electromagnetics. *Progress in Physics*, 2006, v. 2, 78–85.
4. Lehnert B., Roy S. Extended electromagnetic theory. World Scientific Publishers, Singapore, 1998.
5. Lehnert B. Optical effects of an extended electromagnetic theory. In: *Advances in Chemical Physics*, v. 119, Edited by M. W. Evans, I. Prigogine, and S. A. Rice, John Wiley and Sons, Inc., New York, 2001, 1–77.
6. Lehnert B. Photon wave and particle concepts of an extended electromagnetic theory. *Physica Scripta*, 2002, v. 66, 105–113.
7. Lehnert B. Screw-shaped light in extended electromagnetics. *Physica Scripta*, 2005, v. 72, 359–365.
8. Lehnert B. Boundary conditions and spin of a dense light beam. *Physica Scripta*, 2006, v. 74, 139–144.

New Measurement of the Earth's Absolute Velocity with the Help of the “Coupled Shutters” Experiment

Stefan Marinov*

Submitted by Erwin Schneeberger, e-mail: office@erwinschneeberger.com

An account is given of a new execution of my “coupled shutters” experiment. This time the following definite figures for the Earth’s absolute velocity have been obtained: magnitude 360 ± 40 km/sec with equatorial coordinates of the apex $\delta = -24^\circ \pm 7^\circ$, $\alpha = 12.5^\text{h} \pm 1^\text{h}$ (for February 1984).

1 Introduction

I carried out the “coupled shutters” experiment for the first time in 1979 in Brussels [1, 2]. The precision achieved with that first experiment was not sufficient for accurately determining the Earth’s absolute velocity. Thus with that experiment I could only establish that this velocity was not greater than 3,000 km/sec. The “coupled shutters” experiment is relatively very simple and cheap [1, 2], however no scientist in the world has repeated it. The general opinion expressed in numerous letters to me, in referees’ comments on my papers, and in speeches at various space-time conferences which I attended or organized [3] is that my experiments are very sophisticated and difficult to execute. The unique discussion *in the press* on the technical aspects of my experiments is made by Chambers [4]. Here I should like to cite the comments of my anonymous *Foundations of Physics* referee sent to me by the editor, Prof. van der Merwe, on the 23 June 1983:

I was informed by (name deleted) of the Department of the Air Force, Air Force Office of Scientific Research, Bolling Air Force Base, that Dr. Marinov’s ex-

periments were to be repeated by the Joint Institute for Laboratory Astrophysics. On inquiry, I learnt that JILA is not carrying out the experiments, because preliminary engineering studies had indicated that it lay beyond the expertise of the laboratory to achieve the mechanical tolerances needed to ensure a valid result.

After presenting my objections that the fact that JILA in the USA is unable to repeat my experiments cannot be considered as a ground for the rejection of my papers on the measurement of absolute velocity, Prof. van der Merwe sent me on the 24 January 1984 the following “second report” of the same referee:

It is with regret that I cannot change my recommendation regarding Dr. Marinov’s papers. In trying to justify the validity of his experimental work, Dr. Marinov highlights the points which cause the rest of the community so much concern. He states, “If I in a second-hand workshop in a fortnight for USD 500 achieve the necessary accuracy, then, I suppose, JILA can achieve it too.” I know of no one in the precision measurement community who believes that measurements of the quality claimed by Dr. Marinov could be realized under such conditions and in so short a time. It will take very much more than this to change the direction of physics. I suspect that even scientists working in the most reputable laboratories in the U.S. or the world, would encounter great opposition in attempting to publish results as revolutionary as those claimed by Dr. Marinov.

In this paper I present an account of the measurement of the laboratory’s absolute velocity, executed by me in Graz with the help of a new configuration of my “coupled shutters” experiment. Now the apparatus was built not in seven days but in four. As the work was “black” (a mechanician in a university workshop did it after working hours and I paid him “in the hand”), the apparatus was built predominantly over the weekend and cost 12,000 Shillings (USD 1000.-). The driving motor was taken from an old washing-machine and cost nothing.

As no scientific laboratory was inclined to offer me hospitality and the possibility to use a laser source and labora-

*Stefan Marinov (1931–1997), a Bulgarian born experimental and theoretical physicist who invented a new and highly original method to measure the anisotropy of the observable velocity of light (the “coupled shutters” experiment). He reported on the results of his experiment in a few short papers published in the peer-reviewed journals (*Physics Letters*, *General Relativity and Gravitation*, *Foundations of Physics*, etc.). After his formal education, Stefan Marinov worked from 1960 to 1974 with the research staff and also as an Assistant Professor, at the Faculty of Physics, Sofia University. Whilst there he devised and set up his first “coupled shutters” experiment and with it detected an anisotropy in the observed velocity of light. His life in Bulgaria was difficult: he was jailed in 1966/1967, 1974, and 1977, by the Bulgarian communist regime, for inappropriate “political thinking”. In 1977 Marinov was deported from Bulgaria as a “political dissident”. After a few years in Belgium, the USA, and Italy, he continued his research in Graz, Austria, which became his home until his tragic death in 1997. Despite the significant attention drawn to his experiment in the 1980’s (many papers discussing his experiment were published in *Nature* and other journals), no other scientists attempted to repeat it. On the other hand, the experiment is simple, cheap, and can be easily repeated in any well-equipped physics laboratory. We therefore publish this detailed description of the experiment, as given by Marinov himself in *Deutsche Physik*, in 1992. The editors hope that this posthumous publication encourages and assists scientists who would like to repeat and enhance the “coupled shutters” experiment. (This paper was submitted by courtesy of Erwin Schneeberger, who was a close friend of Dr. Marinov, at Graz.)

tory mirrors, my first intention was to use as a light source, the Sun. As I earn my bread and money for continuing the scientific research, working as a groom and sleeping in a stall in a small village near Graz, I carried out the experiment in the apartment of my girl-friend. The sensitivity which I obtained with Sun's light (a perfect source of homogeneous parallel light) was good, but there were two inconveniences: (1) The motion of the Sun is considerable during the time when one makes the reversal of the axle and one cannot be sure whether the observed effect is due to the delay times of the light pulses or to the Sun's motion; (2) One can perform measurements only for a couple of hours about noon and thus there is no possibility to obtain a 24-hour "sinusoid" (explanation of the measuring procedure follows). On the other hand, at fast rotation of the axle the holed rotating disks became two sirens, so that when my apparatus began to whistle the neighbors knocked on the door, asking in dismay: "Fliegt schon der Russe über Wien?" (Is Ivan already flying over Vienna?). After a couple of altercations, my girl-friend threw out of her apartment not only my apparatus but also me.

Later, however, I found a possibility to execute the experiment in a laboratory (Fig. 1). The scheme of the experiment, its theoretical background and measuring procedure, are exactly the same as for the Brussels variation [1, 2]. Since the description is extremely simple and short, I shall also give it here, noting that the mounting of the laser and of the mirrors on the laboratory table lasted two hours.

But first, following the example of *Nature* which gives interesting quotations from its editions many years ago, I should like to also give one similarly:

If it were possible to measure with sufficient accuracy the velocity of light without returning the ray to its starting point, the problem of measuring the first power of the relative velocity of the Earth with respect to the aether would be solved. This may not be as hopeless as might appear at first sight, since the difficulties are entirely mechanical and may possibly be surmounted in the course of time.

The names of the authors are Michelson and Morley, the year of publication is 1887. This is the paper in which Michelson and Morley give their account of the historical experiment for "measurement" of the two-way light velocity. The paper was published in two journals: *The Philosophical Magazine* and *American Journal of Science*. After giving this general opinion, Michelson and Morley proposed an experiment which is almost the same as my deviant "coupled mirrors" experiment [5, 6, 2]. They proposed to use a bridge method with two selenium cells where the null instrument is a telephone. I must emphasize that I could not succeed in finding a single paper or book treating the historic Michelson-Morley experiment, where information on their one-way proposal should be given. Let me note that in the Michelson-Morley experiment one compares the two-way light velocity

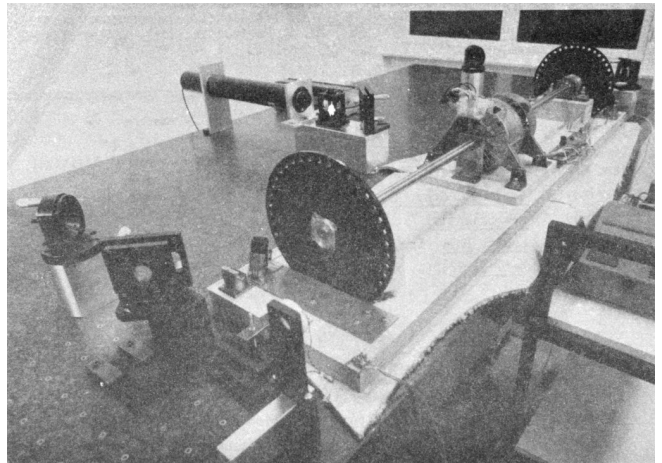


Fig. 1: The Graz "coupled shutters" experiment during preliminary measurements in the air of the laboratory; when performing measurements in vacuum the laser was mounted in parallel with the axle and the regulator for motor's velocity (to be seen between the motor and the far disk) was taken outside the evacuated space. At the left corner of the apparatus' plate one sees the socket for one of the reflecting mirrors for the case that Sun's light should be used (the socket of the other reflecting mirror is at the far right corner). The mechanician spent considerable time (and I lost money) for mastering the *adjustable* reflecting mirrors for Sun's light which have not been used in the laser arrangement, so that the price of the actually used apparatus had to be less than the half.

in two mutually perpendicular directions, but one cannot measure its value.

2 Theory of the "coupled shutters" experiment

A rotating axle driven by an electromotor, located exactly at the middle of the axle, has two holed discs at its extremities. The distance from the centres of the holes to the centre of the axle is R and the distance between the discs is d . Light from a laser is divided by a semi-transparent prism and the two beams are directed by a couple of adjustable mirrors, to the opposite ends of the rotating axle, so that the beams can pass through the discs' holes in mutually opposite directions. Any of the beams, after being chopped by the near disc and "detected" by the far disc, illuminates a photocell. By means of a galvanometer one measures the difference in the currents generated by both photocells. If covering one of the cells, one measures the current produced by the other cell.

One arranges the position of the laser beam with respect to the discs' holes in such a manner that when the axle is at rest the light of the laser which passes through the near hole illuminates *half* of the far hole. One then sets the axle in rotation, gradually increasing its speed. Since the light pulses cut by the near holes have a transit time in order to reach the far holes, with the increase of the rate of rotation less and less light will pass through the far holes, when the distant holes "escape" from the light beam positions, and,

conversely, more and more light will pass through the far holes, when the distant holes “enter” into the light beam positions. For brevity I shall call the first kind of far holes “escaping” and the second kind of far holes “entering”.

If one assumes that the holes as well as the beams’ cross-sections are rectangular and the illuminations homogeneous, then the current I_{hom} produced by either of the photocells will be proportional to the breadth b of the light spot measured on the surface of the photocell when the axle is rotating, i.e., $I_{hom} \sim b$. When the rotational rate of the axle increases by ΔN , the breadth of the light beam passing through the “escaping” holes will become $b - \Delta b$, while the breadth of the light beam passing through “entering” holes will become $b + \Delta b$, and the produced currents will become $I_{hom} - \Delta I \sim b - \Delta b$, $I_{hom} + \Delta I \sim b + \Delta b$. Thus

$$\Delta b = b \frac{\Delta I}{I_{hom}}, \quad (1)$$

where ΔI is the *half* of the *change* in the *difference of the currents* produced by the photocells.

One rotates the axle first with $\frac{\Delta N}{2}$ counter-clockwise and then with $\frac{\Delta N}{2}$ clockwise, that corresponds to a change ΔN in the rate of rotation. Since

$$\Delta b = (d/c) \pi \Delta N R, \quad (2)$$

for the one-way velocity of light one obtains

$$c = \frac{2\pi \Delta N R d}{b} \frac{I_{hom}}{\Delta I} \quad (3)$$

In my experiment the holes, as well as the light beams, were circular, not rectangular. Consequently, instead of the measured light spot’s breadth, one has to take a certain *slightly different* “effective” breadth. As the breadth b can never be measured accurately, the discussion of the difference between real breadth and “effective” breadth is senseless. Much more important, however, was the fact that the illumination in the beams’ cross-sections was not homogeneous: at the centre it was maximum and at the periphery minimum. Thus the simplified relation (1) did not correspond to reality if under I_{hom} one would understand the measured current. I shall give here a certain amelioration of formula (1), which was omitted in Ref. [1], because of a fear that the presumed referee would consider my analysis as an “artificial speculation” in a search “to adapt the observed values to the theoretical formula”. Now I am no more afraid of the referee. The illumination will be assumed to increase *linearly* from zero on the periphery of the light beam to a maximum at its center where the beam is “cut” by the holes’ rims. The *real* current I which one measures is proportional to a certain *middle* illumination across the whole light beam, while the *real* current ΔI is proportional to the *maximum* illumination at the centre of the light beam. On the other hand, one must take into account that when the holes let the light beam fall

on the photocell, first light comes from the peripheral parts and at the end from the central parts. When half of the beam has illuminated the photocell, the “left” part of the beam begins to disappear and its “right” part begins to appear, the breadth remaining always *half* of the beam. Then the holes’ rims begin to extinguish first the central parts of the beam and at the end the peripheral parts. Here, for simplicity, I suppose that the cross-sections of the beams and of the holes are the same (in reality the former were smaller than the latter). Thus during the first one-third of the time of illumination the “left” half of the light beam appears, during the second one-third of the time of illumination the “left” half goes over to the “right” half, and during the last one-third of the time of illumination the “right” half disappears. Consequently, the *real* current, I , produced by the photocell will be related to the *idealized* current, I_{hom} , corresponding to a *homogeneous illumination with the central intensity and generated by a light spot having the half-breadth of the measured one*, by the following connection

$$I = \frac{1}{2} \int_0^1 I_{hom} x \left(\frac{2}{3} - \frac{x}{3} \right) dx = \frac{I_{hom}}{6} \left(x^2 - \frac{x^3}{3} \right) \Big|_0^1 = \frac{I_{hom}}{9}. \quad (4)$$

In this formula $I_{hom}dx$ is the current produced by a strip with breadth dx of the light beam; at the periphery of the beam (where $x=0$) the produced current is zero and at the centre (where $x=1$) it is $I_{hom}dx$. The current $I_{hom}dx$ is produced (i.e. the corresponding photons strike the photocell) during time $\frac{2}{3} - \frac{x}{3}$; for the periphery of the beam this time is $\frac{2}{3} - \frac{0}{3} = \frac{2}{3}$ and for the centre of the beam this time is $\frac{2}{3} - \frac{1}{3} = \frac{1}{3}$. The factor $\frac{1}{2}$ before the integral is present because the *measured* breadth of the light spot over the photocell is *twice* its *working* breadth. Putting (4) into (3), one obtains

$$c = \frac{2\pi \Delta N R d}{b} \frac{9I}{\Delta I}. \quad (5)$$

According to my absolute space-time theory [2, 6, 7] (and according to anybody who is acquainted *even superficially* with the experimental evidence accumulated by humanity), if the *absolute velocity’s component* of the laboratory along the direction of light propagation is v , then the velocity of light is $c - v$ along the propagation direction and $c + v$ against. For these two cases formula (5) is to be replaced by the following two

$$c - v = \frac{2\pi \Delta N R d}{b} \frac{9I}{\Delta I + \delta I}, \quad (6)$$

$$c + v = \frac{2\pi \Delta N R d}{b} \frac{9I}{\Delta I - \delta I},$$

where $\Delta I + \delta I$ and $\Delta I - \delta I$ are the changes of the currents generated by the photocells when the rate of rotation changes

by ΔN . Dividing the second formula (6) by the first one, one obtains

$$v = \left(\frac{\delta I}{\Delta I} \right) c. \quad (7)$$

Thus the measuring method consists of the following: One changes the rotational rate by ΔN and measures the change in the current of either of the photocells, which is $\Delta I \simeq \Delta I \pm \delta I$; then one measures the difference of these two changes which is $2\delta I$. I made both these measurements by a differential method with the same galvanometer, applying to it the difference of the outputs of both photocells. To measure $2\Delta I$ I made the far holes for one of the beam “escaping” and for the other “entering”. To measure $2\delta I$ I made all far holes “escaping” (or all “entering”).

3 Measurement of c

In the Graz variation of my “coupled-shutters” experiment I had: $d = 120$ cm, $R = 12$ cm. The light source was an Ar laser, the photocells were silicon photocollectors, and the measuring instrument was an Austrian “Norma” galvanometer. I measured $I = 21$ mA (i.e., $I_{hom} = 189$ mA) at a rotational rate of 200 rev/sec. Changing the rotation from clockwise to counter-clockwise, i.e., with $\Delta N = 400$ rev/sec, I measured $\Delta I = 52.5 \mu\text{A}$ (i.e., the measured change in the difference current at “escaping” and “entering” far holes was $2\Delta I = 105 \mu\text{A}$). I evaluated a breadth of the light spot $b = -4.3 \pm 0.9$ mm and thus I obtained $c = (3.0 \pm 0.6) \times 10^8$ m/sec, where error is taken as only the error in the estimation of b , because the “weights” of the errors introduced by the measurement of d , R , ΔN , I , ΔI were much smaller. I repeat, the breadth b cannot be measured exactly as the peripheries of the light spot are not sharp. As a matter of fact, I chose such a breadth in the possible uncertainty range of ± 1 mm, so that the exact value of c to be obtained. I wish once more to emphasize that the theory for the measurement of c is built on the assumption of rectangular holes and light beams cross-sections and linear increase of the illumination from the periphery to the center. These simplified assumptions do not correspond to the more complicated real situation. Let me state clearly: The “coupled shutters” experiment is not to be used for an *exact* measurement of c . It is, however, to be used for sufficiently accurate measurement of the variations of c due to the absolute velocity of the laboratory when, during the different hours of the day, the axis of the apparatus takes different orientations in absolute space due to the daily rotation of the Earth (or if one would be able to place the set-up on a rotating platform). The reader will see this now.

4 Measurement of v

The measurement of c is an *absolute*, while the measurement of v is a *relative*, taking the velocity of light c as known.

According to formula (7) one has to measure only two difference currents: $2\Delta I$ (at “escaping” and “entering” far holes) and $2\delta I$ (at “escaping” or “entering” far holes). The measurement in the air of the laboratory had two important inconveniences: (1) Dust in the air led to very big fluctuations in the measured current differences and I had to use a big condenser in parallel with the galvanometer’s entrance, making the apparatus very sluggish; (2) The shrill of the holed disks at high rotational rate could lead to the same gloomy result as when executing the experiment in the apartment of my girlfriend. Thus I covered the whole set-up with a metal cover and evacuated the air by using an oil pump (this amelioration cost an additional 9,000 Shilling, i.e. USD 700,-). The performance of the experiment in vacuum has also the advantage that those people who wish to save at any price the false dogma of the constancy of the velocity of light, cannot raise the objection that the observed effect is due to temperature disturbances.

The measurement of ΔI is a simple problem as the effect is *huge*. Moreover all existing physical schools cannot raise objections against the theory presented above. However, the measurement of δI which is with three orders lower than ΔI has certain peculiarities which must be well understood. When changing the rotation from clockwise to counter-clockwise, the current produced by the one photocell changes, say, from I_1 to $I_1 + \Delta I_1 + \delta I_1$ and of the other photocell from, say, I_2 to $I_2 + \Delta I_2 - \delta I_2$. One makes I_1 to be equal to I_2 , changing the light beam positions by manipulating the reflecting mirrors micrometrically. One can with difficulty obtain an exact compensation, so that the galvanometer shows a certain residual current I' . The current change ΔI_1 will be equal to the current change ΔI_2 only if the experiment is *entirely symmetric*. But it is difficult to achieve a complete symmetry (and, of course, I could not achieve it in my experiment). There are the following disturbances: On the one hand, the distribution of the light intensities in the cross-sections of both beams and the forms of the beams are not exactly the same; thus the covering of the same geometrical parts of both beams when changing the rotation of the axle does not lead to equal changes in the light intensities of both beams and, consequently, to $\Delta I_1 = \Delta I_2$. On the other hand, although the photocells were taken from a unique Sun collector cut in two pieces, even if the changes in the illuminations should be equal, the produced currents may become different (the current gain at the different points of the photocells is not the same, the internal resistances of the cells are not equal, etc. etc.). Thus after changing the rotational rate from clockwise to counter-clockwise, I measured certain current I'' , but $I'' - I'$ was *not* equal to $2\delta I$, as it *must be* for an entirely symmetric setup. However, measuring the difference $I'' - I'$ during different hours of the day, I established that it was “sinusoidally modulated”. This “sinusoidal modulation” was due to the absolute velocity v . All critics of my “rotating axle” experiments vociferate

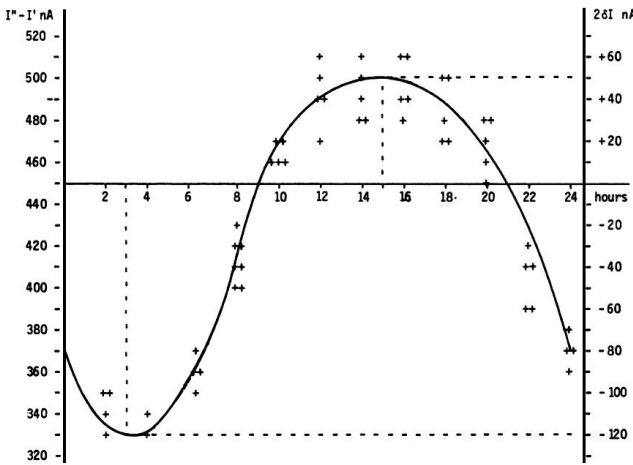


Fig. 2: Measurement of $2\delta I$. The points give the measurements at the even hours for the days from the 9th to the 13th February 1984.

mostly against the vibrations of the axle, asserting that these vibrations will mar the whole measurement. Meanwhile the axle caused me *absolutely no troubles*. When measuring in vacuum the axis of the apparatus pointed north/south.

I measured the “sinusoidal modulation” over 5 days, from the 9th to the 13th February 1984. As I did the experiment alone, I could not cover all 24 hours of every day. The results of the measurements are presented in Fig. 2. The most sensible scale unit of the galvanometer was 10 nA and the fluctuations were never bigger than 20 nA. The daytime hours are on the abscissa and the current differences on the left ordinate. After plotting the registered values of $I'' - I'$ and drawing the best fit curve, the “null line” (i.e., the abscissa) is drawn at such a “height” that the curve has to cut *equal* parts of the abscissa (of any 12 hours). Then on the right ordinate the current $2\delta I$ is taken positive upwards from the null line and negative downwards. Since $105 \mu\text{A}$ corresponds to a velocity 300,000 km/sec, $10 \mu\text{A}$ will correspond approximately to 30 km/sec. Considering the fluctuations of the galvanometer as a unique source of errors, I took $\pm 30 \text{ km/sec}$ as the uncertainty error in the measurement of v .

When $2\delta I$ has maximum or minimum the Earth’s absolute velocity lies in the plane of the laboratory’s meridian (Fig. 3). The velocity components pointing to the north are taken positive and those pointing to the south negative. I always denote by v_a the component whose algebraic value is smaller. When both light beams pass through “escaping” holes, then, in the case that the absolute velocity component points to the north, the “north” photocell produces less current than the “south” photocell (with respect to the case when the absolute velocity component is perpendicular to the axis of the apparatus), while in the case that the absolute velocity component points to the south, the “north” photocell produces more current. If the light beams pass through “entering” holes, all is vice versa. Let me note that for the case

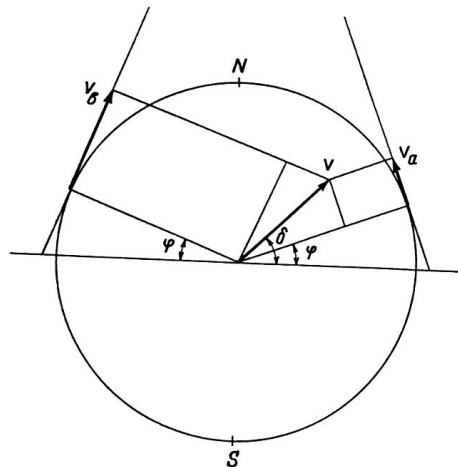


Fig. 3: The Earth and its absolute velocity at the two moments when the laboratory meridian lies in the velocity’s plane.

shown in Fig. 3 (which does not correspond to the real situation, as in reality v_a is negative) both velocity components point to the north and both v_a and v_b are positive. In this case the “variation curve” no longer has the character of a “sinusoid”; it has 4 extrema (for 24 hours) and the “null line” must be drawn tangentially to the lowest minimum.

As can be seen from Fig. 3, the two components of the Earth’s absolute velocity in the horizontal plane of the laboratory, v_a and v_b , are connected with the magnitude v of the absolute velocity by the following relations

$$v_a = v \sin(\delta - \phi), \quad v_b = v \sin(\delta + \phi), \quad (8)$$

where ϕ is the latitude of the laboratory and δ is the declination of the velocity’s apex. From these one obtains

$$v = \frac{\{v_a^2 + v_b^2 - 2v_a v_b (\cos^2 \phi - \sin^2 \phi)\}^{\frac{1}{2}}}{2 \sin \phi \cos \phi}, \quad (9)$$

$$\tan \delta = \frac{v_b + v_a}{v_b - v_a} \tan \phi.$$

Obviously the apex of v points to the meridian of v_a . Thus the right ascension α of the apex equaled the local sidereal time of registration of v_a . From Fig. 2 it is to be seen that this moment can be determined with an accuracy of $\pm 1^\text{h}$. Thus it was enough to calculate (with an inaccuracy not larger than $\pm 5 \text{ min}$) the sidereal time t_{si} for the meridian where the local time is the same as the standard time t_{st} of registration, taking into account that the sidereal time at a middle midnight is as follows:

22 September	—	0^h	23 March	—	12^h
22 October	—	2^h	23 April	—	14^h
22 November	—	4^h	23 May	—	16^h
22 December	—	6^h	22 June	—	18^h
21 January	—	8^h	23 July	—	20^h
21 February	—	10^h	22 August	—	22^h

The graph in Figure 2 shows that on the 11th February (the middle day of observation) I registered in Graz ($\phi = 47^\circ$, $\delta = 15^\circ 26'$) the following components of the absolute velocity at the following hours (for $2(\delta I)_a = -120\text{nA}$, and $2(\delta I)_b = 50\text{nA}$)

$$\begin{aligned} v_a &= -342 \pm 30 \text{ km/sec}, \quad (t_{st})_a = 3^{\text{h}} \pm 1^{\text{h}}, \\ v_b &= +143 \pm 30 \text{ km/sec}, \quad (t_{st})_b = 15^{\text{h}} \pm 1^{\text{h}}, \end{aligned} \quad (10)$$

and formulae (9) give

$$\begin{aligned} v &= 362 \pm 40 \text{ km/sec}, \\ \delta &= -24^\circ \pm 7^\circ, \quad \alpha = (t_{si})_a = 12.5^{\text{h}} \pm 1^{\text{h}}. \end{aligned} \quad (11)$$

where the errors are calculated supposing $\phi = 45^\circ$.

The local sidereal time for the observation of v_a (i.e., the right ascension of the absolute velocity's apex) was calculated in the following manner: As for any day the sidereal time increases by 4^{m} (with respect to the solar time), the sidereal time at midnight on the 11th February (which follows 21 days after midnight on the 21 January) was $8^{\text{h}} + 1^{\text{h}} 24^{\text{m}} = 9^{\text{h}} 24^{\text{m}}$. At 3^{h} middle European (i.e., Graz) time on the 11th February the local sidereal time on the 15th meridian was $9^{\text{h}} 24^{\text{m}} + 3^{\text{h}} = 12^{\text{h}} 24^{\text{m}}$. On the Graz meridian the local sidereal time was $12^{\text{h}} 24^{\text{m}} + 2^{\text{m}} = 12^{\text{h}} 26^{\text{m}} \simeq 12.5^{\text{h}}$.

Important remark. I now establish that when calculating the local sidereal time of observation of v_a for my interferometric "coupled mirrors" experiment [2, 6, 8, 9], I made a very *unpleasant error*. As Sofia ($\lambda = 23^\circ 21'$) lies westwards from the middle zonal meridian ($\lambda = 30^\circ$), I had to *subtract* the difference of $6^\circ 39'$, which corresponds to 27^{m} , from the local sidereal time of the zonal meridian. Instead of doing this, I *wrongly added*. Thus the numbers given by me are to be corrected as follows:

Observation:	Wrongly calculated:	To be corrected to:
12 July 1975	$(t_{si})_a = 14^{\text{h}} 23^{\text{m}}$	$(t_{si})_a = 13^{\text{h}} 30^{\text{m}}$
11 January 1976	$(t_{si})_a = 14^{\text{h}} 11^{\text{m}}$	$(t_{si})_a = 13^{\text{h}} 17^{\text{m}}$
Right ascension of the apex of the Sun's absolute velocity	$\alpha = 14^{\text{h}} 17^{\text{m}}$	$\alpha = 13^{\text{h}} 23^{\text{m}}$

I beg the persons who will refer to the measurement of the Sun's absolute velocity determined by me in 1975/76 to cite *always* the corrected figures given here and not the wrongly calculated figures presented in [2, 6, 8, 9, 10, 11] and in some others of my papers.

5 Conclusions

Comparing the figures obtained now by the Graz variation of my "coupled shutters" experiment with the figures obtained some ten years ago in Sofia by the interferometric "coupled



Fig. 4: February 1984. Explaining the essence of the "coupled shutters" experiment. My fingers show the ways in which both light beams go from the one perforated disk to the other. One can see on the photograph only a small part of the laser producing the initial light beam which is split by the semitransparent mirror seen in the photograph. The reflected beam goes to the left, while the refracted beam, after a reflection on the mirror seen in the photograph, goes to the right. Between the perforated disks, these two beams proceed in the opposite directions. The person who gave me a possibility to carry out my "coupled shutters" experiment in his laboratory took from me the solemn promise that I shall never say where have I carried it out. To my question, why is he so afraid, the answer was: "I do not wish one day to be poisoned by certain special services."

"mirrors" experiment, one sees that within the limits of the supposed errors they overlap. Indeed, on the 11 January 1976 I registered in Sofia the following figures

$$\begin{aligned} v &= 327 \pm 20 \text{ km/sec}, \\ \delta &= -21^\circ \pm 4^\circ, \quad \alpha = 13^{\text{h}} 17^{\text{m}} \pm 20^{\text{m}}. \end{aligned} \quad (12)$$

As for the time of one month the figures do not change significantly, one can compare directly the figures (11) with the figures (12). The declinations are the same. As the Graz measurements were done every two hours, the registration of the right ascension was not exact enough and the difference of about one hour is not substantial. I wish to point only to the difference between the magnitudes which is 35 km/sec. I have the intuitive feeling that the figures obtained in Sofia are more near to reality. The reason is that *I profoundly believe in the mystique of the numbers*, and my Sofia measurements led to the magic number 300 km/sec for the Sun's absolute velocity (which number is to be considered together with 300,000 km/sec for light velocity and 30 km/sec for the Earth's orbital velocity). The Graz measurement destroys

this mystic harmony.

The presented account on the Graz “coupled shutters” experiment shows that the experiment is *childishly simple*, as I always asserted [1, 2]. If the scientific community refuses to accept my measurements for so many years and nobody tries to repeat them, the answer can be found in the following words of one of my *best physical and moral teachers*:

Terrible is the power which an authority exerts over the world.

Albert Einstein

I wish to add in closing that with a letter of the 29 December 1983 I informed the Nobel committee that I am ready at any time to bring (for my account) the “coupled shutters” experiment to Stockholm and to demonstrate the registration of the Earth’s absolute motion. With a letter of 28 January 1984 Dr. B. Nagel of the Physics Nobel committee informed me that my letter had been received.

References

1. Marinov S. Measurement of the one-way speed of light and the Earth’s absolute velocity. *Speculations in Science and Technology*, 1980, v. 3, 57; *Proc. 2nd Marcel Grossmann Meeting on General Relativity*, Trieste, 5–11 July, 1979, North-Holland, Amsterdam & New York, 1982, p. 547–550.
2. Marinov S. Classical physics. East-West, Graz, 1981.
3. Marinov S. The thorny way of truth. East-West, Graz, 1982.
4. Chambers R. G. In: *Proceedings of ICSTA – Intern. Conference on Space-Time Absoluteness*, Genoa, July 1982, eds. S. Marinov and J. P. Wesley, East-West, Graz, 1982, p. 44.
5. Marinov S. The velocity of light is direction dependent. *Czechoslovak Journal of Physics*, 1974, v. B24, 965–970.
6. Marinov S. Eppur si muove. C.B.D.S., Brussels, 1977; 2nd and 3rd ed., East-West, Graz, 1981 and 1987 resp.; 4th edition, 2006 (*in print*).
7. Marinov S. *Foundations of Physics*, 1979, v. 9, 445.
8. Marinov S. *Abstracts of GR8 – Intern. Conference on General Relativity and Gravitation*, Waterloo, Canada, August 1977, p.244.
9. Marinov S. Measurement of the laboratory’s absolute velocity. *General Relativity & Gravitation*, 1980, v. 12, 57–65.
10. Marinov S. *New Scientist*, 1976, v. 71, 662.
11. Marinov S. *Foundations of Physics*, 1976, v. 6, 571.

Upper Limit in the Periodic Table of Elements

Albert Khazan

E-mail: albhazan@list.ru

The method of rectangular hyperbolas is developed for the first time, by which a means for estimating the upper bound of the Periodic Table is established in calculating that its last element has an atom mass of 411.663243 and an atomic number (the nuclear charge) of 155. The formulating law is given.

1 Introduction. The mathematical basis

The periodic dependence of the properties of the elements on their atomic mass, as discovered by D. I. Mendeleev in 1869, predicted the existence of new elements in appropriate locations in the Periodic Table.

Progress in synthesis and in the study of the properties of the far transuranium elements has increased interest in the question of the upper limits of the Periodic Table. G. T. Seaborg, J. L. Bloom and V. I. Goldanskii emphasized that the charge of the atomic nucleus and the position occupied by the element "define unambiguously the structure of electron jackets of its atoms and characterize the whole set of its chemical properties". They suggested the existence of nuclei containing 114, 126 and 164 protons, 184, and 258 neutrons and the Table arrangement of the relevant elements [1, 2].

The objective of this study is to determine the possible number of chemical elements, along with atomic masses and atomic numbers up to the final entry in the Periodic Table.

The calculations were performed on the basis of IUPAC [3] table data for all known elements. The basic principle resides in the idea that the proportion of the defined element Y in any chemical compound of molecular mass X should be related to its single gram-atom. In this case, if K is the atomic mass, the equation $Y = \frac{K}{X}$ would represent a rectangular hyperbola in the first quadrant ($K > 0$). Its asymptotes conform to the axis coordinates, and semi-axis $a = b = \sqrt{2|K|}$. The peak of the curve should occur on the virtual axis inclined at an angle of 45° to the positive direction of the abscissa axis. The necessary conditions associated with this chemical conception are: $Y \leq 1$ and $K \leq X$.

The foregoing equation differs only in the atomic mass for each element of the Periodic Table and allows calculation of the proportion of the element in any compound. Accuracy plotting the curve and the associated straight line in the logarithmic coordinates depends on the size of the steps in the denominator values, which can be entirely random but must be on the relevant hyperbola in terms of X . Consequently, it can be computed without difficulty by prescribing any value of the numerator and denominator. In Table 1a are given both known oxygen containing compounds and random data on X arranged in the order of increasing molecular mass. Fig. 1 depicts the hyperbola (the value of the approximation

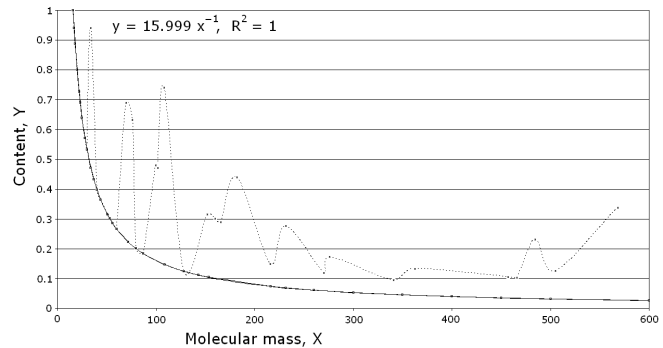


Fig. 1: Oxygen content versus the molecular mass of compounds on estimation to 1 gram-atom (hyperbola $y = k/x$) and the total amount of O (maxima, leaders). The molecular mass in the table is given according to its increase.

certainty $R^2 = 1$), calculated for 1 gram-atom of oxygen.

Estimation of the unobserved content in the chemical compound as determined by the formula is expressed on the plot by the polygonal line (Table 1b, Fig. 1). It is obvious from the Fig. 2a that the hyperbolic function of the elemental proportion in chemical compounds plotted against molecular mass, by the example of the second Group, is true ($R^2 = 1$). In the logarithmic coordinates (Fig. 2b) it is represented as the straight lines arranged in the fourth quadrant (to the right of hydrogen) all with slope 1. With the view to expansion of the basis of the arguments, this example is given for the first Group including "roentgenium" No. 111, a more recently identified element, and the predicted No. 119 and No. 155. The real axis is shown here, on which the peaks of all hyperbolas of the Periodic Table are arranged (see below).

2 Using the theorem of Lagrange

It is clear from the Fig. 2a that with the rise of the atomic mass the curvature of the hyperbola decreases (the radius of curvature increases), and the possibility to define its peak, for example, by means of graphical differentiation, becomes a problem due to errors of both subjective and objective character (instrument, vision and so on). Therefore, to estimate the curve peak of the hyperbola the mathematical method of the theorem of Lagrange was used [4].

K	X	$Y = \frac{K}{X}$	$\ln X$	$\ln Y$	Compound		Compound	X	$Y = n \frac{K}{X}$
15.9994	15.999	1	2.77255	0	O		O	15.9994	1
15.9994	17.007	0.9408	2.83363	-0.0611	$\frac{1}{2}\text{H}_2\text{O}_2$		H_2O	18.015	0.88811546
15.9994	18.015	0.8881	2.8912	-0.1187	H_2O		BeO	25.01	0.63972011
15.9994	20	0.8	2.99573	-0.2232	—		CO	28.01	0.57120314
15.9994	22	0.7272	3.09104	-0.3185	—		NO	30.006	0.53320669
15.9994	23.206	0.6895	3.14441	-0.3719	$\frac{1}{3}\text{B}_2\text{O}_3$		H_2O_2	34.01	0.94089974
15.9994	25.01	0.6397	3.21928	-0.4467	BeO		MgO	40.304	0.39698293
15.9994	28.01	0.5712	3.33256	-0.56	CO		N_2O	44.012	0.36353722
15.9994	30.006	0.5332	3.4014	-0.6288	NO		CaO	56.077	0.28532197
15.9994	33.987	0.4708	3.52598	-0.7534	$\frac{1}{3}\text{Al}_2\text{O}_3$		COS	60.075	0.26633375
15.9994	37	0.4324	3.61092	-0.8384	—		B_2O_3	69.618	0.68947686
15.9994	40.304	0.397	3.69645	-0.9239	MgO		N_2O_3	76.01	0.63149586
15.9994	44.012	0.3635	3.78446	-1.0119	N_2O		CuO	79.545	0.20114401
15.9994	50.663	0.3158	3.9252	-1.1526	$\frac{1}{3}\text{Cr}_2\text{O}_3$		Cl_2O	86.905	0.18410908
15.9994	53.229	0.3006	3.9746	-1.2021	$\frac{1}{3}\text{Fe}_2\text{O}_3$		CrO ₃	99.993	0.4800336
15.9994	56.077	0.2853	4.02673	-1.2542	CaO		Al_2O_3	101.96	0.47077285
15.9994	60.075	0.2663	4.09559	-1.323	COS		N_2O_5	108.008	0.74068588
15.9994	71.844	0.2227	4.2745	-1.5019	FeO		CdO	128.41	0.12460089
15.9994	79.545	0.2011	4.37632	-1.6038	CuO		Cr_2O_3	151.99	0.31581025
15.9994	86.905	0.1841	4.46482	-1.6923	Cl_2O		Fe_2O_3	159.687	0.30058803
15.9994	108.6	0.1473	4.6877	-1.9151	$\frac{1}{3}\text{La}_2\text{O}_3$		Co ₂ O ₃	165.86	0.2894007
15.9994	128.41	0.1246	4.85523	-2.0827	CdO		V_2O_5	181.88	0.43985045
15.9994	143.09	0.1118	4.96348	-2.1909	Cu_2O		WO ₂	215.84	0.14825797
15.9994	153.33	0.1043	5.03257	-2.26	BaO		Fe ₃ O ₄	231.53	0.27642206
15.9994	216.59	0.0739	5.37801	-2.6055	HgO		UO ₂	270.027	0.11850667
15.9994	231.74	0.069	5.44562	-2.6731	Ag ₂ O		Ag ₂ CO ₃	275.75	0.174064
15.9994	260	0.0615	5.56068	-2.7881	—		UO ₂ Cl ₂	340.94	0.0938546
15.9994	300	0.0533	5.70378	-2.9312	—		Gd ₂ O ₃	362.5	0.132409
15.9994	350	0.0457	5.85793	-3.0854	—		Tl ₂ O ₃	456.764	0.10508709
15.9994	400	0.04	5.99146	-3.2189	—		Bi ₂ O ₃	465.96	0.103009
15.9994	450	0.0356	6.10925	-3.3367	—		Re ₂ O ₇	484.4	0.231205
15.9994	500	0.032	6.21461	-3.4421	—		Tl ₂ SO ₄	504.8	0.1267781
15.9994	600	0.0267	6.39693	-3.6244	—		Ce ₂ (SO ₄) ₃	568.43	0.33776

Table 1: Content of oxygen Y in compounds X per gram-atom (Table 1a) left and summarized O (Table 1b) on the right.

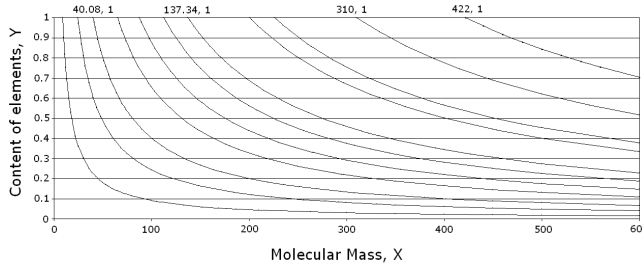


Fig. 2a: Element proportion in chemical compounds against molecular mass ($y = k/x$) on the example of the 2nd Group of the Periodic Table, plus No.126 and No.164.

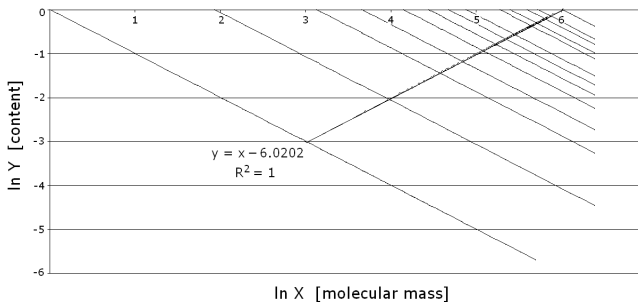


Fig. 2b: Element content versus the molecular mass in chemical compounds of the 1st Group and No.119, calculated No.119, No.155; + virtual axis.

For example, the coordinates of the peak for beryllium are as follows: $X = 60.9097$, $Y = 0.14796$, the normal equation is $Y = 0.0024292X$. Taking into consideration that the semiaxis of the rectangular hyperbola $a = b = \sqrt{2|K|}$, the coordinates of the point $X_0 = Y_0 = \sqrt{K}$.

Let us examine this fact in relation to elements with the following atomic masses (K): beryllium Be (9.0122), random Z (20), chromium Cr (51.9961), mercury Hg (200.59), No. 126 (310), random ZZ (380), No. 164 (422), random ZZZ (484). In this case $X_0 = Y_0 = \sqrt{K}$, and correspondingly, 3.00203, 4.472136, 7.210825, 14.16298, 17.606817, 19.493589, 20.54264, 22.

The obtained values are the coordinates of the rectangular hyperbola peaks ($X_0 = Y_0$), arranged along the virtual axis, the equation of which is $Y = X$ (because $\tan \alpha = 1$).

3 The point of crossing and the scaling coefficient

Our attention is focused on the point of crossing of the virtual axis with the line $Y = 1$ in Fig. 3 when the atomic mass and the molecular mass are equal, i.e. $K = X$. It is possible only in the case when the origin of the hyperbola and its peak coincide in the point with the maximum content Y according to the equation $Y = \frac{K}{X}$.

The atomic mass of this element was calculated with application of the scaling coefficient and the value of the slope of the virtual axis (the most precise mean is 0.00242917): $\tan \alpha = \frac{y}{x} = 0.00242917$, from which $x = \frac{y}{\tan \alpha}$. Due to

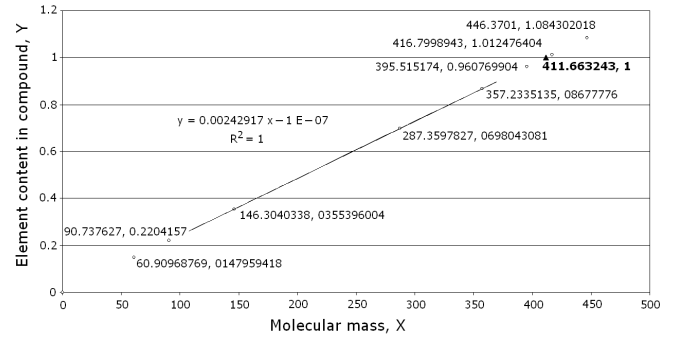


Fig. 3: The virtual axis of the hyperbolas $y = k/x$ with application of the scaling coefficient.

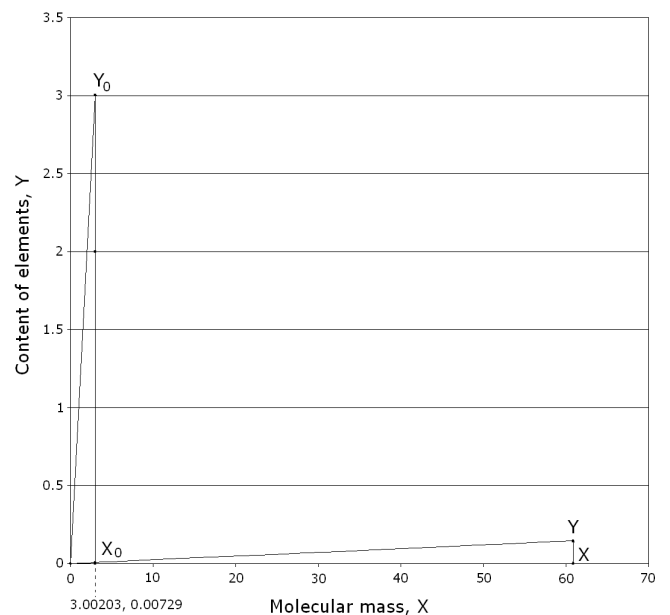


Fig. 4: Inversely proportional dependency in coordinates at calculation of the scaling coefficient.

the fact that at this point $k = x$ we have: $\frac{y}{\tan \alpha} = \frac{1}{\tan \alpha} = 411.663243$. This value is equal to the square of the scaling coefficient too: $20.2895^2 = 411.6638$, $\Delta = 0.0006$.

The coefficient was calculated from matching of the coordinates of the peak hyperbola for beryllium: $X_0 = Y_0 = \sqrt{K}$ and $X = 60.9097$, $Y = 0.14796$. Using this data to construct two triangles (Fig. 4), one easily sees an inversely proportional relationship: $\frac{X}{X_0} = \frac{Y_0}{Y}$, whence $\frac{X}{X_0} = \frac{60.9097}{3.00203} = 20.2895041$ and $\frac{Y_0}{Y} = \frac{3.00203}{0.14976} = 20.28947013$, $\Delta = 0.000034$.

The calculated value $M = 20.2895$ is the scaling coefficient. With its help the scale of system coordinates can be reorganised.

Now if one rectangular hyperbola peak is known, $X_0 = Y_0 = \sqrt{K}$, then the new coordinates will be: $X = X_0 M$ or $X = M\sqrt{K}$, $Y = \frac{\sqrt{K}}{M}$. Furthermore, $\tan \alpha_0 = \frac{Y_0}{X_0} = 1$, so $\tan \alpha = \frac{Y}{X} = \frac{1}{M^2}$. At the same time at $Y = 1$ and $K = X$, $X = \frac{Y}{\tan \alpha}$ or $K = \frac{Y}{\tan \alpha} = \frac{1}{\tan \alpha} = M^2$.

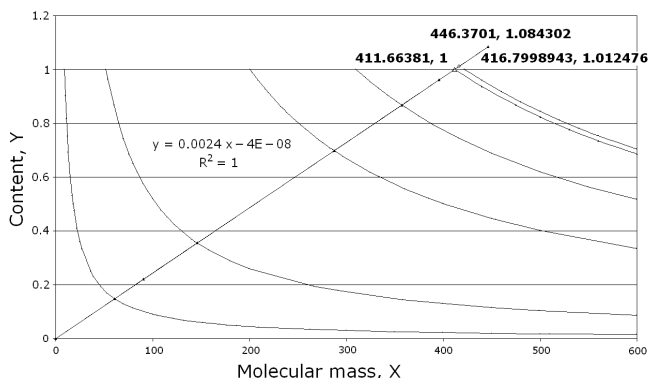


Fig. 5: Element content versus the compound's molecular mass and the hyperbola virtual axes of type $y = k/x$ for the entire Periodical Table. Additionally No.126, No.164 and that rated on (ZZZZ) are introduced.

The results obtained are plotted in Fig. 5 in comparison with the hyperbolas of such elements as Be, Cr, Hg and the hypothetical No.126 (atomic mass = 310), No.164 (atomic mass = 422), ZZZZ (atomic mass = 411.66). It is obvious that it is practically impossible to choose and calculate precisely the curve peak for an atomic mass exceeding the value 250 without the application of the mathematical method adduced herein.

The rated element ZZZZ is the last in the Periodic Table because the hyperbola No.164 after it crosses the virtual axis at the point which coordinates are: $X_0 = Y_0 = \sqrt{422} = 20.5426386$.

After scaling we have $X = 20.2895 \times 20.5426386 = 416.8$ and $Y = 20.5426386 / 20.2895 = 1.0125$, but this makes no sense because Y cannot exceed the value 1. In addition, the hypothetical atomic mass 422 occurred higher than the molecular mass 416.8, i.e. $X < K$, but that is absurd. Similarly, it is obvious from Fig. 2b how the virtual axis (the equation $Y = X - 6.0202$ where $Y = \ln y$, $X = \ln x$) crossing all the logarithmic straight lines at the points corresponding to the hyperbola peaks, takes the value $\ln x = 6.0202$ at $\ln y = 0$, or after taking logarithms, $X = 411.66$, $Y = 1$.

4 The atomic (ordinal) number

To determine important characteristics of the atomic number some variants of graphical functions of the atomic mass versus the nucleus of all the elements were studied, including No.126. One of them is exponential, with the equation $Y = 1.6091 e^{1.0992x}$ (where y is the atomic mass, x is $\ln N$) at $R^2 = 0.9967$. After taking the logarithm of the both sides and inserting the atomic mass of 411.66 we have No.155. The calculations also demonstrated that the ordinal No.126 should have the atomic mass 327.2 but not 310.

Finally, the following atomic masses were obtained: No.116 – 298.7, No.118 – 304.4, No.119 – 307.2, No.120 – 310, No.126 – 327.3, No.155 – 411.66.

5 The new law

Based on the foregoing, the heretofore unknown Hyperbolic law of the Periodic Table of Elements is established.

This law is due to the fact that the element content Y when estimated in relation to 1 gram-atom, in any chemical combination with molecular mass X , may be described by the adduced equations for the positive branches of the rectangular hyperbolas of the type $Y = \frac{K}{X}$ (where $Y \leq 1$, $K \leq X$), arranged in the order of increasing nuclear charge, and having the common virtual axis with their peaks tending to the state $Y = 1$ or $K = X$ as they become further removed from the origin of coordinates, reaching a maximum atomic mass designating the last element.

References

1. Seaborg G. T. and Bloom J. L. The synthetic elements. *Scientific American*, 1969, v.220(4), 56.
2. Goldanskii V. I. About connections nuclear and chemical physics. *Progress in Physical Sciences*, 1976, v. 118, issue 2.
3. IUPAC Commission on Atomic Weights and Isotopic Abundances/Atomic Weights of the Elements, 2001.
4. Weisstein E. W. Mean-value theorem. *CRC Concise Encyclopedia of Mathematics*, 2nd edition, CRC Press, Boca Raton (FL), 2003, 1881.

Less Mundane Explanation of Pioneer Anomaly from Q-Relativity

Florentin Smarandache* and Vic Christianto†

*Department of Mathematics, University of New Mexico, Gallup, NM 87301, USA

E-mail: smarand@unm.edu

†Sciprint.org — a Free Scientific Electronic Preprint Server, <http://www.sciprint.org>

E-mail: admin@sciprint.org

There have been various explanations of Pioneer blueshift anomaly in the past few years; nonetheless no explanation has been offered from the viewpoint of Q-relativity physics. In the present paper it is argued that Pioneer anomalous blueshift may be caused by Pioneer spacecraft experiencing angular shift induced by similar Q-relativity effect which may also affect Jupiter satellites. By taking into consideration “aether drift” effect, the proposed method as described herein could explain Pioneer blueshift anomaly within $\sim 0.26\%$ error range, which speaks for itself. Another new proposition of redshift quantization is also proposed from gravitational Bohr-radius which is consistent with Bohr-Sommerfeld quantization. Further observation is of course recommended in order to refute or verify this proposition.

1 Introduction

In the past few years, it is becoming well-known that Pioneer spacecraft has exhibited an anomalous Doppler frequency blueshifting phenomenon which cannot be explained from conventional theories, including General Relativity [1, 4]. Despite the nature of such anomalous blueshift remains unknown, some people began to argue that a post-einsteinian gravitation theory may be in sight, which may be considered as further generalisation of pseudo-Riemannian metric of general relativity theory.

Nonetheless, at this point one may ask: Why do we require a generalization of pseudo-Riemannian tensor, instead of using “patch-work” as usual to modify general relativity theory? A possible answer is: sometimes too much path-work doesn’t add up. For instance, let us begin with a thought-experiment which forms the theoretical motivation behind General Relativity, an elevator was put in free-falling motion [8a]. The passenger inside the elevator will not feel any gravitational pull, which then it is interpreted as formal analogue that “inertial acceleration equals to gravitational acceleration” (Equivalence Principle). More recent experiments (after Eötvös) suggest, however, that this principle is only applicable at certain conditions.

Further problem may arise if we ask: what if the elevator also experiences lateral rotation around its vertical axis? Does it mean that the inertial acceleration will be slightly higher or lower than gravitational pull? Similarly we observe that a disc rotating at high speed will exert out-of-plane field resemble an acceleration field. All of this seems to indicate that the thought-experiment which forms the basis of General Relativity is only applicable for some limited conditions, in particular the $F = m \frac{dv}{dt}$ part (because General Relativity is strictly related to Newtonian potential), but it may not be able to represent the rotational aspects of gravita-

tional phenomena. Einstein himself apparently recognizes this limitation [8a, p.61]:

“... all bodies of reference K' should be given preference in this sense, and they should be exactly equivalent to K for the formation of natural laws, provided that they are in a state of *uniform rectilinear and non-rotary motion* with respect to K .” (Italic by Einstein).

Therefore, it shall be clear that the restriction of *non-rotary motion* remains a limitation for all considerations by relativity theory, albeit the *uniform rectilinear* part has been relaxed by general relativity theory.

After further thought, it becomes apparent that it is required to consider a new kind of metric which may be able to represent the rotational aspects of gravitation phenomena, and by doing so extends the domain of validity of general relativity theory.

In this regard, the present paper will discuss the aforementioned Pioneer blueshift anomaly from the viewpoint of Q-relativity physics, which has been proposed by Yefremov [2] in order to bring into application the quaternion number. Despite the use of quaternion number in physical theories is very scarce in recent years — apart of Pauli matrix — it has been argued elsewhere that using quaternion number one could expect to unify all known equations in Quantum Mechanics into the same framework, in particular via the known isomorphism between Dirac equation and Maxwell equations [5].

Another problem that was often neglected in most treatises on Pioneer spacecraft anomaly is the plausible role of aether drift effect [6]. Here it can be shown that taking this effect into consideration along with the aforementioned Q-relativity satellite’s apparent shift could yield numerical prediction of Pioneer blueshift within $\sim 0.26\%$ error range, which speaks for itself.

We also suggest a new kind of Doppler frequency shift which can be predicted using Nottale-type gravitational Bohr-radius, by taking into consideration varying G parameter as described by Moffat [7]. To our knowledge this proposition of new type of redshift corresponding to gravitational Bohr-radius has never been considered before elsewhere.

Further observation is of course recommended in order to verify or refute the propositions outlined herein.

2 Some novel aspects of Q-relativity physics. Pioneer blueshift anomaly

In this section, first we will review some basic concepts of quaternion number and then discuss its implications to quaternion relativity (Q-relativity) physics [2]. Then we discuss Yefremov's calculation of satellite time-shift which may be observed by precise measurement [3]. We however introduce a new interpretation here that such a satellite Q-timeshift is already observed in the form of Pioneer spacecraft blueshift anomaly.

Quaternion number belongs to the group of "very good" algebras: of real, complex, quaternion, and octonion [2]. While Cayley also proposed new terms such as quantic, it is less known than the above group. Quaternion number can be viewed as an extension of Cauchy imaginary plane to become [2]:

$$Q \equiv a + bi + cj + dk, \quad (1)$$

where a, b, c, d are real numbers, and i, j, k are imaginary quaternion units. These Q-units can be represented either via 2×2 matrices or 4×4 matrices [2].

It is interesting to note here that there is quaternionic multiplication rule which acquires compact form:

$$1q_k = q_k 1 = q_k, \quad q_j q_k = -\delta_{jk} + \epsilon_{jkn} q_n, \quad (2)$$

where δ_{kn} and ϵ_{jkn} represent 3-dimensional symbols of Kronecker and Levi-Civita, respectively [2]. Therefore it could be expected that Q-algebra may have neat link with pseudo-Riemannian metric used by General Relativity. Interestingly, it has been argued in this regard that such Q-units can be generalised to become Finsler geometry, in particular with Berwald-Moor metric. It also can be shown that Finsler-Berwald-Moor metric is equivalent with pseudo-Riemannian metric, and an expression of Newtonian potential can be found for this metric [2a].

It may also be worth noting here that in 3D space Q-connectivity has clear geometrical and physical treatment as movable Q-basis with behaviour of Cartan 3-frame [2].

It is also possible to write the dynamics equations of Classical Mechanics for an inertial observer in constant Q-basis. $SO(3, R)$ -invariance of two vectors allow to represent these dynamics equations in Q-vector form [2]:

$$m \frac{d^2}{dt^2} (x_k q_k) = F_k q_k. \quad (3)$$

Because of antisymmetry of the connection (generalised angular velocity) the dynamics equations can be written in vector components, by conventional vector notation [2]:

$$m \left(\vec{a} + 2\vec{\Omega} \times \vec{v} + \vec{\Omega} \times \vec{r} + \vec{\Omega} \times (\vec{\Omega} \times \vec{r}) \right) = \vec{F}. \quad (4)$$

Therefore, from equation (4) one recognizes known types of classical acceleration, i.e. linear, coriolis, angular, centripetal. Meanwhile it is known that General Relativity introduces Newton potential as *rigid* requirement [2a, 6b]. In other words, we can expect — using Q-relativity — to predict new effects that cannot be explained with General Relativity.

From this viewpoint one may consider a generalisation of Minkowski metric into biquaternion form [2]:

$$dz = (dx_k + idt_k) q_k, \quad (5)$$

with some novel properties, i.e.:

- temporal interval is defined by imaginary vector;
- space-time of the model appears to have six dimensions (6D);
- vector of the displacement of the particle and vector of corresponding time change must always be normal to each other, or:

$$dx_k dt_k = 0. \quad (6)$$

It is perhaps quite interesting to note here that Einstein himself apparently once considered similar approach, by proposing tensors with Riemannian metric with Hermitian symmetry [8]. Nonetheless, there is difference with Q-relativity described above, because in Einstein's generalised Riemannian metric it has 8-dimensions, rather than 3d-space and 3d-imaginary time.

One particularly interesting feature of this new Q-relativity (or rotational relativity) is that there is universal character of motion of the bodies (including non-inertial motions), which can be described in unified manner (Hestenes also considers Classical Mechanics from similar spinor language). For instance advanced perihelion of planets can be described in term of such rotational precession [2].

Inspired by this new Q-relativity physics, it can be argued that there should be anomalous effect in planets' satellite motion. In this regard, Yefremov argues that there should be a deviation of the planetary satellite position, due to discrepancy between calculated and observed from the Earth motion magnitudes characterizing cyclic processes on this planet or near it. He proposes [2]:

$$\Delta\varphi \approx \frac{\omega V_e V_p}{c^2} t, \quad (7)$$

or

$$\Delta\varphi' \approx -\frac{\omega V_e V_p}{c^2} t'. \quad (8)$$

Therefore, given a satellite orbit radius r , its position shift is found in units of length $\Delta l = r \Delta\varphi$. His calculation

Satellites	Cycle frequency ω , 1/s	Angular shift $\Delta\varphi$, "/100 yrs	Linear shift Δl , km/100 yrs	Linear size a , km
Phobos (Mars)	0.00023	18.2	54	20
Deimos (Mars)	0.00006	4.6	34	12
Metis (Jupiter)	0.00025	10.6	431	40
Adrastea (Jupiter)	0.00024	10.5	429	20
Amalthea (Jupiter)	0.00015	6.3	361	189

Table 1: The following table gives values of the effect for five fast satellites of Mars and Jupiter. Orbital linear velocities are: of the Earth $V_E = 29.8$ km/s, of Mars $V_P = 24.1$ km/s, of Jupiter $V_P = 13.1$ km/s; the value of the light velocity is $c = 299\,793$ km/s; observation period is chosen 100 years. Courtesy of A. Yefremov, 2006 [3].

for satellites of Mars and Jupiter is given in Table 1. Nonetheless he gave no indication as to how to observe this anomalous effect.

In this regard, we introduce here an alternative interpretation of the aforementioned Q-satellite time-shift effect by Yefremov, i.e. this effect actually has similar effect with Pioneer spacecraft blueshift anomaly. It is known that Pioneer spacecraft exhibits this anomalous Doppler frequency while entering Jupiter orbit [1, 4], therefore one may argue that this effect is caused by Jupiter planetary gravitational effect, which also may cause similar effect to its satellites.

Despite the apparent contradiction with Yefremov's own intention, one could find that the aforementioned Q-satellite time-shift could yield a natural explanation of Pioneer spacecraft blueshift anomaly. In this regard, Taylor [9] argues that there is possibility of a mundane explanation of anomalous blueshift of Pioneer anomaly (5.99×10^{-9} Hz/sec). The all-angle formulae for relativistic Doppler shift is given by [9a, p.34]:

$$v' = v_0 \gamma \frac{(1 - \beta \cos \phi)}{\sqrt{1 - \beta^2}}, \quad (9)$$

where $\beta = v/c$. By neglecting the $\sqrt{1 - \beta^2}$ term because of low velocity, one gets the standard expression:

$$v' = v_0 \gamma (1 - \beta \cos \phi). \quad (9a)$$

The derivative with respect to ϕ is:

$$\frac{dv'}{d\phi} = v_0 \gamma \beta \sin \phi, \quad (10)$$

where $\frac{dv'}{d\phi} = 5.99 \times 10^{-9}$ Hz/sec, i.e. the observed Pioneer anomaly. Introducing this value into equation (10), one gets requirement of an effect to explain Pioneer anomaly:

$$d\phi = \frac{\arcsin(5.99 \times 10^{-9} \text{ Hz})}{v_0 \gamma \beta} = 1.4 \times 10^{-12} \text{ deg/sec}. \quad (11)$$

Therefore, we can conclude that to explain 5.99×10^{-9} Hz/sec blueshift anomaly, it is required to find a shift of emission angle at the order 1.4×10^{-12} degree/sec only (or around $15.894''$ per 100 years).

Interestingly this angular shift can be explained with the same order of magnitude from the viewpoint of Q-satellite angular shift (see Table 1), in particular for Jupiter's Adrastea ($10.5''$ per 100 years). There is however, a large discrepancy at the order of 50% from the expected angular shift.

It is proposed here that such discrepancy between Q-satellite angular shift and expected angular shift required to explain Pioneer anomaly can be reduced if we take into consideration the "aether drift" effect [6]. Interestingly we can use experimental result of Thorndike [6, p.9], saying that the aether drift effect implies a residual apparent Earth velocity is $v_{obs} = 15 \pm 4$ km/sec. Therefore the effective V_e in equation (8) becomes:

$$V_{e,eff} = v_{obs} + V_e = 44.8 \text{ km/sec}. \quad (12)$$

Using this improved value for Earth velocity in equation (8), one will get larger values than Table 1, which for Adrastea satellite yields:

$$\Delta\varphi_{obs} = \frac{\omega V_{e,eff} V_p}{c^2} t = \frac{V_{e,eff}}{V_e} \Delta\varphi = 15.935''/100 \text{ yrs}. \quad (13)$$

Using this improved prediction, the discrepancy with required angular shift only ($15.894''$ per 100 years) becomes $\sim 0.26\%$, which speaks for itself. Therefore one may conclude that this less mundane explanation of Pioneer blueshift anomaly with Q-relativity may deserve further consideration.

3 A new type of redshift from gravitational Bohr radius. Possible observation in solar system.

In preceding paper [10, 11] we argued in favour of an alternative interpretation of Tifft redshift quantization from the viewpoint of quantized distance between galaxies. A method can be proposed as further test of this proposition both at solar system scale or galaxies scale, by using the known quantized Tifft redshift [14, 15, 16]:

$$\delta r \approx \frac{c}{H} \delta z. \quad (14)$$

In this regards, we use gravitational Bohr radius equation:

$$r_n = n^2 \frac{GM}{v_0^2}. \quad (15)$$

Inserting equation (15) into (14), then one gets quantized redshift expected from gravitational Bohr radius:

$$z_n = \frac{H}{c} n^2 \frac{GM}{v_0^2} \quad (16)$$

which can be observed either in solar system scale or galaxies scale. To our present knowledge, this effect has never been described elsewhere before.

Therefore, it is recommended to observe such an accelerated Doppler-frequency shift, which for big jovian planets this effect may be detected. It is also worth noting here that according to equation (16), this new Doppler shift is quantized.

At this point one may also take into consideration a proposition by Moffat, regarding modification of Newtonian acceleration law to become [7]:

$$a(r) = -\frac{G_\infty M}{r^2} + K \frac{\exp(-\mu_\phi r)}{r^2} (1 + \mu_\phi r) \quad (17)$$

where

$$G_\infty = G \left[1 + \sqrt{\frac{M_0}{M}} \right]. \quad (17a)$$

Therefore equation (16) may be rewritten to become:

$$z_n \approx \frac{H}{c} n^2 \frac{GM}{v_0^2} \left[1 + \sqrt{\frac{M_0}{M}} \right] \approx \chi \frac{H}{c} n^2 \frac{GM}{v_0^2} \quad (18)$$

where n is integer (1, 2, 3, ...) and:

$$\chi = \left[1 + \sqrt{\frac{M_0}{M}} \right]. \quad (18a)$$

To use the above equations, one may start by using Bell's suggestion that there is fundamental redshift $z = 0.62$ which is typical for various galaxies and quasars [14]. Assuming we can use equation (16), then by setting $n = 1$, we can expect to predict the mass of quasar centre or galaxy centre. Then the result can be used to compute back how time-variation parameter affects redshift pattern in equation (18). In solar system scale, time-varying radius may be observed in the form of changing Astronomical Unit [4].

This proposition, however, deserves further theoretical considerations. Further observation is also recommended in order to verify and explore further this proposition.

4 Concluding remarks

In the present paper it is argued that Pioneer anomalous blueshift may be caused by Pioneer spacecraft experiencing angular shift induced by similar Q-relativity effect which may also affect Jupiter satellites. By taking into consideration aether drift effect, the proposed method as described herein could predict Pioneer blueshift within $\sim 0.26\%$ error range, which speaks for itself. Further observation is of course recommended in order to refute or verify this proposition.

Another new proposition of redshift quantization is also proposed from gravitational Bohr-radius which is consistent with Bohr-Sommerfeld quantization. It is recommended to conduct further observation in order to verify and also to explore various implications of our propositions as described herein.

Acknowledgment

The authors are would like to thank to Profs. C. Castro, E. Scholz, T. Love, and D. L. Rapoport for valuable discussions. Special thanks to Prof. A. Yefremov for sending his recent calculation of Jupiter satellite's Q-time-shift effect.

References

1. Anderson J.D., Campbell J.K., & Nieto M.M. arXiv: astro-ph/060807; [1a] Nieto M.M. & Anderson J.D. arXiv: gr-qc/0507052.
2. Yefremov A. *Hypercomplex Numbers in Geometry and Physics*, 2004, v. 1(1), 105; [2a] Pavlov D.G. arXiv: math-ph/0609009.
3. Yefremov A. Private communication, October 2006. Email: a.yefremov@rudn.ru.
4. Laemmerzahl C. & Dittus H. Clocks and gravity, from quantum to cosmos. UCLA, 2006, http://www.physics.ucla.edu/quantum_to_cosmos/q2c06/Laemmerzahl.pdf
5. Christianto V. *EJTP*, 2006, v. 3, No. 12, <http://www.ejtp.com>.
6. Consoli M. arXiv: physics/0306094, p. 9; [6a] Consoli M. et al. arXiv: gr-qc/0306105; [6b] arXiv: hep-ph/0109215.
7. Moffat J. arXiv: astro-ph/0602607.
8. Einstein A. *Ann. Math.*, 1945, v. 46; [8a] Einstein A. Relativity: the special and general theory. Crown Trade Paperback, New York, 1951, pp. 61, 66–70.
9. Taylor S. arXiv: physics/0603074; [9a] Engelhardt W. *Apeiron*, 2003, v. 10, No. 4, 34.
10. Smarandache F. & Christianto V. *Progress in Physics*, 2006, v. 4, 27–31.
11. Smarandache F. & Christianto V. *Progress in Physics*, 2006, v. 4, 37–40.
12. Smarandache F. & Christianto V. *Progress in Physics*, 2006, v. 2, 63–67.
13. Fischer U. arXiv: cond-mat/9907457; [13a] arXiv: cond-mat/0004339.
14. Bell M.B. arXiv: astro-ph/0111123; [14a] Bell M.B. arXiv: astro-ph/0305112; [14b] Bell M.B. arXiv: astro-ph/0305060.
15. Humphreys R. *TJ Archive*, v. 16, <http://answersingenesis.org>.
16. Múnera H. *Apeiron*, 1998, v. 5, No. 3–4.
17. Zurek W. (ed.) *Proc. Euroconference in Formation and Interaction of Topological Defects*, Plenum, 1995; arXiv: cond-mat/9502119.
18. Volovik G. arXiv: cond-mat/0507454.

Study of the Matrix Effect on the Plasma Characterization of Heavy Elements in Soil Sediments using LIBS with a Portable Echelle Spectrometer

Walid Tawfik Y. Mohamed*,† and Abeer Askar*

*National Inst. of Laser Enhanced Science NILES, Dept. of Environmental Applications, Cairo University, Cairo, Egypt

†Faculty of Education for Girls, Department of Physics, Gurayyat, North of Al-gouf, Kingdom of Saudi Arabia

Corresponding author: Walid Tawfik Y. Mohamed. E-mail: Walid_Tawfik@hotmail.com

Laser-induced breakdown spectroscopy (LIBS) has been applied to perform a study of the matrix effect on the plasma characterization of soil sediment targets. The plasma is generated by focusing a pulsed Nd: YAG laser on the target in air at atmospheric pressure. The plasma emission spectrum was detected using a portable Echelle spectrometer (Mechelle 7500 — Multichannel Instruments, Stockholm, Sweden) with intensified CCD camera. Spectroscopic analysis of plasma evolution of laser produced plasmas has been characterized in terms of their spectra, and electron temperature. Four heavy elements V, Pb, Mn and Co were determined in the obtained spectra. The LTE and optically thin plasma conditions were verified for the produced plasma. The electron temperature and density were determined using the emission intensity and stark broadening, respectively, of the spectral lines of the heavy elements in the soil sediments. The electron temperature does not change with concentration. For environmental applications, the obtained results showed the capability of the proposed LIBS setup with the portable Mechelle 7500 spectrometer to be applied in-situ for real-time measurements of the variation of the matrix elemental composition of soil sediments by following up only a single element as a marker for the composition of the soil sediment without need of analysis of the other elements.

1 Introduction

The Laser Induced Breakdown Spectroscopy (LIBS) technique has been already applied to the determination of elemental concentrations in a wide range of materials in solid, liquid and gaseous phase. Measurements consist of spectral and time resolved analysis of the atomic and ionic emission lines, arising from the plasma generated by an intense laser pulse. In the case of condensed samples, the plasma is produced through laser-induced evaporation of the sample surface layer [1]. The use of laser induced breakdown spectroscopy (LIBS) in the analysis of soil and soil sediments has been studied in recent years as a technique for in-situ detection of hazardous metals [2–7]. One of the main problems in the use of LIBS is the necessity of making a calibration curve with samples possessing the same matrix composition of the samples to be analyzed. In 1998, Valery Bulatov et al. proposed a method in which the composition of a sample could be determined without the need of calibration curves [8]. However, this method is based on the measurement of the emission from all the species present in the sample, a requirement difficult to satisfy when dealing with soil sediments. The physical and chemical properties of the sample can affect the produced plasma composition, a phenomenon known as the matrix effect. The matrix effect can result in the sample being ablated differently from the target sample. The interaction between the laser and the

target in LIBS is influenced significantly by the overall composition of the target, so that the intensity of the emission lines observed is a function of both the concentration of the elements of interest and the properties of the matrix that contains them. Plasma composition is dependent not only on the composition of the sample, but also on laser parameters, sample surface conditions as well as on thermal and optical properties of the sample. Previously published works studied the matrix effect under different experimental conditions to specify causes and find out the methods of correction [9–14]. The different approaches have been undertaken to discriminate between the problems resulting from the fractionation of the ablation and matrix effects. The most convenient approach is to determine elemental abundance by comparing the analyte line intensities with signals obtained from the proper reference standards having a similar matrix composition [15]. But it is not always possible to obtain such calibration curves because there are no available standard samples, or it is impossible to have an internal standard of known concentration [16]. In addition, plasma formation dynamics, sample ablation and associated processes, are highly non-linear and not fully understood and may also play an important rôle in the matrix effect.

Recently an alternative procedure, based on the LIBS technique, for quantitative elemental analysis of solid materials has been proposed, which can, in principle, provide quantitative data with no need of calibration curves or intern-

al standards [17, 18]. The method relies on the assumption about the existence of the stoichiometric ablation and local thermodynamic equilibrium (LTE) i.e. Boltzmann distribution and Saha equation amongst the level population of any species and electron density and temperature of the plasma. However for application of this method experimentally one needs to obtain both equilibrium and thin plasma conditions, a task that may not be always possible to perform. Thus, in spite of the many advantages of LIBS the realization of a quantitative analytical method, which is able to measure the main constituents in samples from different matrices, still remains a difficult task because of the complex laser-sample and laser-plasma interaction mechanisms. As a rule, laser ablation plasma is characterized by complex spatial and temporal structures, and one meets a wide range of parameter variation during the plasma existence time.

In this paper we report on the optimized conditions for LIBS to analyze the emission spectrum of soil sediment samples with high resolution using a portable Echelle spectrometer — Mechelle 7500 — equipped with an ICCD camera. Spectroscopic analysis of plasma evolution of laser produced plasmas has been characterized in terms of their spectra, and electron temperature. Four heavy elements V, Pb, Mn and Co were determined in the obtained spectra. The electron temperature was determined using the emission intensity of the spectral lines of the heavy elements in the soil sediments. The dependence of the electron temperature on the concentrations of these heavy elements was studied.

The aim of this paper is to prove that the proposed LIBS setup could be used in the on-line environmental applications control. This could be done by following up only a single element as a marker for the composition of the soil sediment without need of analysis of the other elements.

2 Methodology

A typical LIBS experimental setup, described in detail elsewhere [3, 9, 10, 15], was used throughout the present investigations. Laser induced plasma was produced by focusing 180 mJ of a Q-switched Nd: YAG laser (surelite I, continuum, USA) operating at 1064 nm (pulse duration of 7 ns) on soil sediment samples. An energy meter (Nova 978, Ophir Opttronics Ldt., USA) was employed to monitor the shot to shot pulse energy. The laser beam was focused on soil sediment samples by a 10 cm focal length quartz lens to generate the plasma. The focal point was set 5 mm below the surface of the sample in order to generate plasma of 800 μm spot diameter. This also minimized breakdown above the surface of any particles and aerosols generally present above the sample. A one meter length of used-silica optical fiber (600 μm diameter) mounted on a micro *xyz*-translation stage was used to collect the emission light from the plasma plume and feed it to a portable Echelle spectrometer of a 0.17 m focal length (Mechelle 7500, Multichannel instruments, Sweden).

The use of a micro *xyz*-translation stage as a holder for fused-silica optical fibre facilitated maximum intensity of the observed emission light from the plasma plume. On the other hand, the Echelle grating spectrometers, designed for operation in high orders and high angles of incidence and diffraction, can provide high resolution in a more compact size and cover a much wider spectral range than conventional grating spectrometers [19]. This is because the Mechelle 7500 provides a constant spectral resolution (CSR) of 7500 corresponding to 4 pixels FWHM over a wavelength range 200–1000 nm displayable in a single spectrum. A gateable, intensified CCD camera, (DiCAM-Pro-12 bit, UV enhanced, 43000 channels, PCO Computer Optics, Germany) coupled to the spectrometer was used for detection of the dispersed light. The overall linear dispersion of the spectrometer camera system ranges from 0.006 (at 200 nm) to 0.033 nm/pixel (at 1000 nm). To avoid electronic interference and jitters, the intensifier high voltage was triggered optically. Echelle spectra display, control, processing and analysis were done using both Mechelle software (Multichannel Instruments, Stockholm, Sweden) and GRAMS/32 version 5.1 Spectroscopic Data Analysis Software (Galactic Industries, Salem, NH, USA).

To improve LIBS precision, spectra from several laser shots have to be averaged in order to reduce statistical error due to laser shot-to-shot fluctuation. We reproduced the measurements at four locations on the sample surface in order to avoid problems linked to sample heterogeneity. Fifty laser shots were fired at each location and saved in separated files and the average (average of 250 spectra) was computed and saved to serve as the library spectrum. For each recorded spectrum, the peak intensity, the Lorentzian curve fitting, the full width at half maximum FWHM, and the center wavelength of each line, as well as the background emission continuum were determined. Data treatment preprocessing of the averaged spectra was performed in the Microsoft Windows XP environment on a Pentium 4 PC using GRAMS/32, Excel (Microsoft office Excel 2003) and Origin software version 7.0220 (Origin Lab corporation, USA). The averages of peak tables (lists of wavelengths and intensities) of the averaged spectra were roll generated in GRAMS/32 and exported for data evaluation.

Three certified reference samples were purchased from the International Atomic Energy Agency (IAEA). The standard samples were named IAEA-SL-1, IAEA-SL-5 and IAEA-SL-7. Another three standard samples have been made by mixing of the IAEA-samples in different ratios. These samples were named Mix A, Mix B, and Mix C. The composition of Mix A, Mix B and Mix C are (37.3% of IAEA-SL-1 + 62.7% of IAEA-SL-5), (37.3% of IAEA-SL-7 + 62.7% of IAEA-SL-5) and (26.3% of IAEA-SL-1 + 73.7% of IAEA-SL-7) respectively. These mixtures were carefully blended and ground in a ceramic grinder, then sieved using a stainless steel sieve with a net grain size of 70 microns to ensure

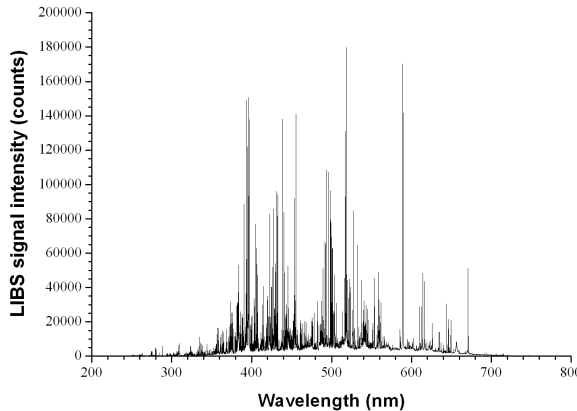


Fig. 1: Typical LIBS spectrum for soil sediment target. The laser energy was 100 mJ at wavelength 1064 nm, plasma emissions are accumulated with delay 2.5 μ s, and gate width 1 μ s.

Sample	Mn	Pb	Co	V
IAEA-SL-1	3460	37.7	19.8	170
IAEA-SL-5	852	129	14.8	151
IAEA-SL-7	631	60	8.9	66
Mix A	1825	95	16.6	158
Mix B	770	103.2	12.6	119.3
Mix C	1375	54.1	11.7	93.4

Table 1: The elemental concentrations of Mn, Pb, Co and V in the six standard soil sediments (in ppm).

good homogeneity and to simulate the properties of the original standard samples. The powder of each of the six standard samples was put into a stainless steel dish (30-mm diameter \times 7-mm deep) to be pressed into a form of tablet at a hydraulic press weight of 20 tons/cm² to be suitable for handling in LIBS experiments. The elemental concentrations of Mn, Pb, Co and V in the six standard soil sediments are given in Table 1.

3 Results and discussion

3.1 LIBS spectrum

Figure 1 shows a typical plasma emission spectrum for soil sediment sample IAEA-SL-1. This spectrum is the average of 250 single shot spectra recorded at 1.5 μ s delay time and 1 μ s gate width.

The panoramic Echelle spectra in the spectral range 200–750 nm show the UV-visible emission lines of soil sediment samples which have a very rich spectral structure and, consequently a lot of interfering lines. In particular, soil sediment samples, made mostly of inorganic material constituents, give rise to a dense spectrum due to the contribution of heavy atom emissions in the investigated range [6]. Moreover, our observed spectra reflect the wide spectral range and the high resolution of the spectroscopic system used.

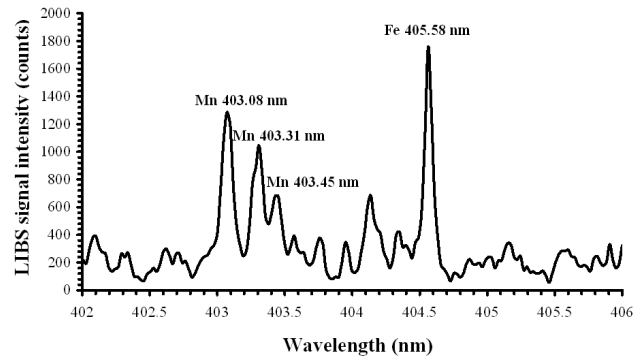


Fig. 2: Shows a high resolution spectrum of Mn with concentration of 0.346% in soil sediment sample IAEA-SL-1. Intensities ratios of the manganese triplet at wavelengths: 403.08, 403.31 and 403.45 nm are consistent with the ratios of the statistical weights of their upper level (7:5:3).

3.2 Plasma characterization

In LIBS experiments, after the initial plasma decay and during the entire observation interval, the local thermodynamic equilibrium (LTE) conditions are assumed to hold.

On the other hand, optically thin plasma has been confirmed by checking the intensity ratios of the manganese triplet at wavelengths: 403.08, 403.31 and 403.45 nm which are consistent with the ratios of the statistical weights of their upper level (7:5:3) as shown in Fig. 2 (refer to Table 2). This result indicates that the plasma was optically thin according to a procedure described previously by Simeonsson and Miziolek [20].

For optically thin plasma, the re-absorption effects of plasma emission are negligible, so the emitted spectral line intensity I is a measure of the population of the corresponding energy level of this element in the plasma. For the LTE plasma, the population of an excited level can be related to the total density $N(T)$ of neutral atom or ion of this element by Boltzmann equation as:

$$I = \frac{hc}{4\pi\lambda} N(T) \frac{A_{ki} g_k}{U(T)} \exp\left(-\frac{E_k}{KT}\right), \quad (1)$$

where λ is the wavelength, A_{ki} is the transition probability, g_k is the statistical weight for the upper level, E_k is the excited level energy, T is the temperature (in LTE all temperatures are assumed to be equal, i.e. $T_e \approx T_{ion} \approx T_{plasma}$, K is Boltzmann's constant, $U(T)$ is the partition function).

The emitted spectral line intensity from a given state of excitation can be used to evaluate the plasma temperature. The lines must be well resolved for accurately evaluating their wavelengths λ , intensities I , and their transition probabilities A_{ki} must be well known [21].

Reformulating Eqn. 1 gives:

$$\ln \frac{I \lambda}{A_{ki} g_k} = -\frac{1}{KT} E_k + \ln \frac{C F}{U(T)}, \quad (2)$$

Element	Wavelength, nm	A_{ki}, s^{-1}	E_k, cm^{-1}	g_k	Element	Wavelength, nm	A_{ki}, s^{-1}	E_k, cm^{-1}	g_k
Pb	240.194	2.79E+07	49439.62	3	Co	242.493	3.20E+08	41225.76	10
Pb	244.6181	2.45E+07	48686.93	3	Co	243.221	2.60E+08	41918.41	8
Pb	244.6181	2.45E+07	48686.93	3	Co	252.136	3.00E+08	39649.16	8
Pb	247.6378	3.78E+07	48188.63	5	Co	252.897	2.80E+08	40345.95	6
Pb	247.6378	3.78E+07	48188.63	5	Co	253.596	1.90E+08	40827.77	4
Pb	257.726	6.68E+07	49439.62	3	Co	254.425	3.00E+08	41101.8	2
Pb	257.726	6.68E+07	49439.62	3	Co	340.512	1.00E+08	32841.99	10
Pb	261.3655	1.87E+07	46068.44	3	Co	344.364	6.90E+07	33173.36	8
Pb	261.4175	2.35E+08	46060.84	5	Co	345.35	1.10E+08	32430.59	12
Pb	262.8262	5.59E+07	48686.93	3	Co	347.402	5.60E+07	33466.87	8
Pb	265.7094	9.91E+05	45443.17	5	Co	348.94	1.30E+08	36092.44	6
Pb	266.3154	1.01E+08	48188.63	5	Co	350.228	8.00E+07	32027.5	8
Pb	280.1995	1.08E+08	46328.67	7	Co	351.835	1.60E+08	36875.13	4
Pb	282.3189	3.04E+07	46060.84	5	Co	356.938	1.50E+08	35450.56	8
Pb	283.3053	5.92E+07	35287.22	3	Co	358.719	1.40E+08	36329.86	6
Pb	287.3311	4.15E+07	45443.17	5	Co	389.408	6.90E+07	34133.59	8
Pb	357.2729	4.08E+08	49439.62	3	V	230.785	2.60E+08	47345.94	11
Pb	363.9568	3.20E+07	35287.22	3	V	231.16	2.80E+08	47807.58	9
Pb	367.1491	1.11E+08	48686.93	3	V	231.405	2.80E+08	48151.07	7
Pb	368.3462	1.70E+08	34959.91	1	V	231.496	2.70E+08	48388.62	5
Pb	373.9935	8.30E+07	48188.63	5	V	235.341	1.90E+08	47039.27	7
Pb	401.9632	3.55E+07	46328.67	7	V	236.38	2.10E+08	46320.96	9
Pb	405.7807	9.12E+07	35287.22	3	V	237.862	1.90E+08	45378.85	9
Pb	406.2136	1.07E+08	46068.44	3	V	238.345	1.80E+08	45972.17	7
Co	231.16	2.80E+08	47807.58	9	V	238.892	2.80E+08	45197.78	11
Co	231.405	2.80E+08	48151.07	7	V	240.416	1.50E+08	46786.53	3
Co	235.341	1.90E+08	47039.27	7	V	240.725	3.60E+08	41528.53	12
Co	236.38	2.10E+08	46320.96	9	V	241.446	3.40E+08	42811.44	8
Co	237.862	1.90E+08	45378.85	9	V	241.53	3.60E+08	43199.65	6
Co	238.345	1.80E+08	45972.17	7	V	242.493	3.20E+08	41225.76	10
Co	238.892	2.80E+08	45197.78	11	V	243.221	2.60E+08	41918.41	8
Co	240.416	1.50E+08	46786.53	3	V	243.666	2.60E+08	42434.23	6
Co	240.725	3.60E+08	41528.53	12	V	243.905	2.70E+08	42796.67	4
Co	241.446	3.40E+08	42811.44	8	V	252.136	3.00E+08	39649.16	8
Co	241.53	3.60E+08	43199.65	6	V	252.897	2.80E+08	40345.95	6
V	253.596	1.90E+08	40827.77	4	Mn	404.14	7.87E+07	41789.48	10
V	254.425	3.00E+08	41101.8	2	Mn	404.88	7.50E+07	42143.57	4
V	340.512	1.00E+08	32841.99	10	Mn	405.55	4.31E+07	41932.64	8
V	344.364	6.90E+07	33173.36	8	Mn	405.89	7.25E+07	42198.56	2
V	345.35	1.10E+08	32430.59	12	Mn	406.17	1.90E+07	49415.35	6
V	347.402	5.60E+07	33466.87	8	Mn	406.35	1.69E+07	42053.73	6
V	348.94	1.30E+08	36092.44	6	Mn	407.92	3.80E+07	42143.57	4
V	350.228	8.00E+07	32027.5	8	Mn	408.29	2.95E+07	42053.73	6
V	351.835	1.60E+08	36875.13	4	Mn	408.36	2.80E+07	41932.64	8
V	356.938	1.50E+08	35450.56	8	Mn	423.51	9.17E+07	46901.13	6
V	358.719	1.40E+08	36329.86	6	Mn	441.49	2.93E+07	45940.93	6
V	389.408	6.90E+07	34133.59	8	Mn	445.16	7.98E+07	45754.27	8
Mn	401.81	2.54E+07	41932.64	8	Mn	446.20	7.00E+07	47207.28	10
Mn	403.08	1.70E+07	24802.25	8	Mn	475.40	3.03E+07	39431.31	8
Mn	403.31	1.65E+07	24788.05	6	Mn	478.34	4.01E+07	39431.31	8
Mn	403.45	1.58E+07	24779.32	4	Mn	482.35	4.99E+07	39431.31	8

Table 2: A list of the spectroscopic data of the spectral lines used for the determination of plasma temperature and density of soil sediment samples.

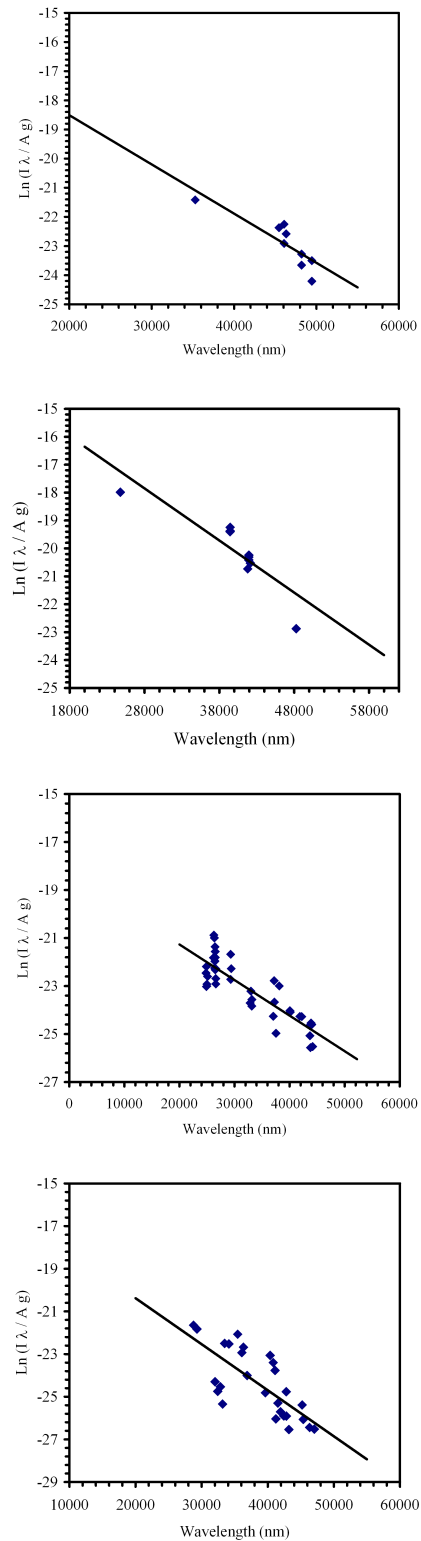


Fig. 3: Four Boltzmann plots were determined form the emission line intensities of Pb, Mn, V, and Co (shown, respectively, from up to down) observed in the laser-induced plasma of soil sediments. The slope of the plotted curves yields temperatures of for the elements 8526 K, 7700 K, 9693 K, and 6658 K respectively.

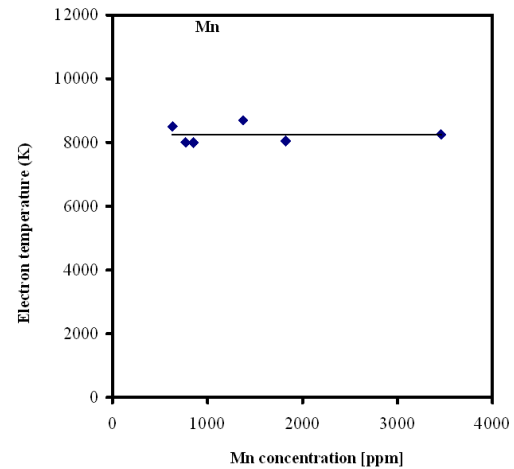


Fig. 4: Temperature measured at $2.5 \mu\text{s}$ delay time and $1 \mu\text{s}$ gate width for different concentrations of manganese in soil sediment samples.

where F is an experimental factor and C is the species concentration.

By plotting the left hand side of Eqn. 2 against the excited level energy E_k , the plasma temperature can be obtained from the slope of the resulting straight line.

The temperatures were determined form the emission line intensities of Mn, V, Co, and Pb observed in the laser-induced plasma of soil sediments. Figure 3 shows four Boltzmann plots of Eqn. 2, for each of these four trace elements where the data were fitted with the least-squares approximation. The spectral line wavelengths, energies of the upper levels, statistical weights, and transition probabilities used for each element are obtained from Griem [21], NIST [22] and Kurucz [23], and listed in Table 2. The slope of the plotted curves yields temperatures 7700 K, 9693 K, 6658 K, and 8526 K for the elements Mn, V, Co, and Pb respectively. The average value of the plasma temperature is 8000 K for soil sediment, which agrees with the value obtained by V. Lazic et al. [27] under conditions similar to ours. The difference in the plasma temperature of the four elements may be attributed to the difference in the excitation and ionization potentials between these elements.

Study of the matrix effect on the plasma temperature was done by plotting the corresponding temperature for each element against its concentration in the soil sediment samples. The variation of the plasma temperature with the concentration of the four elements was found to be about ± 500 K around the 8000 K as shown in Fig. 4 for Mn as an example. The figure reveals that plasma temperature has a small variation, due to some experimental errors and matrix effect, around an average value with the elemental concentration. This can be understood as follows; for optically thin plasma, increasing the element concentration returns an increasing intensity of its corresponding spectral lines with roughly the same ratio, which leads to the same slope of the Boltzmann

plot and results in the same plasma temperature.

The electrons in the plasma can perturb the energy levels of the individual ions which broaden the emission lines originating from these excited levels. Stark broadening of well-isolated lines in the plasma is, thus, useful for estimating the electron number densities provided that the Stark-broadening coefficients have been measured or calculated. The line profile for Stark broadening is well described by a Lorentzian function. The Stark line width $\Delta\lambda_{FWHM}$ can be extracted from the measured line width $\Delta\lambda_{observed}$ by subtracting the instrumental line broadening $\Delta\lambda_{instrument}$:

$$\Delta\lambda_{FWHM} = \Delta\lambda_{observed} - \Delta\lambda_{instrument}. \quad (3)$$

In our case $\Delta\lambda_{instrument}$ was 0.05 nm (determined by measuring the FWHM of the Hg lines emitted by a standard low pressure Hg lamp).

The width of Stark broadened spectral lines depends on the electron density N_e . The electron density N_e (in cm^{-3}) could be determined from the FWHM of the line from the formula [21]:

$$N_e \approx \left(\frac{\Delta\lambda_{FWHM}}{2w} \right) \times 10^{16}, \quad (4)$$

where w is the electron impact parameter (stark broadening value). This formula is generally used for calculations of plasma generated from solid targets [7, 27, 28]. Substituting the values of Stark broadening w from [21], [30], [31], and [32] in Eqn. 4, the electron density for soil sediment samples is $3 \times 10^{17} \text{ cm}^{-3}$. The obtained results agree with those reported by O. Samek [29].

Finally, by knowing the electron density and the plasma temperature we can determine whether the local thermodynamic equilibrium (LTE) assumption is valid by applying the criterion given by McWhirter [26].

The lower limit for electron density for which the plasma will be in LTE is:

$$N_e \geq 1.6 \times 10^{12} \Delta E T^{1/2}, \quad (5)$$

where ΔE is the largest energy transition for which the condition holds and T is the plasma temperature [20].

In the present case $\Delta E = 4.9 \text{ eV}$ for Si (one of the main elements in soil sediments) and the electron density lower limit value given by Eqn. 5 is $6 \times 10^{15} \text{ cm}^{-3}$ (see ref. 21). The experimentally calculated densities are greater than this value, which is consistent with the assumption that the LTE prevails in the plasma.

4 Conclusion

In summary, we have carried out an accurate LIBS setup using a portable commercial Echelle spectrometer equipped with ICCD detector to study soil sediments matrix effects on the plasma characterization. Four trace heavy elements V, Pb, Mn and Co were determined in the obtained spectra. The

electron density and plasma temperature were determined for the soil sediment targets. For a plasma diagnostics perspective, the target physical properties play an important role in the obtained values of the laser induced plasma temperature T_e and electron density N_e . The obtained results indicate that the produced plasma parameters (T_e , N_e) are the same for any of the elements in the same matrix composition. On the other hand, T_e and N_e are different for different matrix composition as proven previously by our group [10]. So the proposed LIBS setup could be used in on-line environmental applications control. This could be done by following up only single element as markers for the composition of the soil sediment without need of analysis of the other elements.

Acknowledgements

The authors especially acknowledge Prof. M. Abdel Harith for offering the soil sediment samples.

References

- Piepmeier E.H. Laser ablation for atomic spectroscopy analytical application of laser. John Wiley & Sons, N.Y., 1986.
- Davies B.E. Trace metals in the environment: retrospect and prospect. In: Adriano D.C., Ed. *Biogeochemistry of Trace Metals, Advances in Trace Substances Research*, Lewis Publishers, Boca Raton, FL, 1992, 1–17.
- Soliman M., Tawfik W., and Harith M.A. Quantitative elemental analysis of agricultural drainage water using laser induced breakdown spectroscopy, First Cairo conference on plasma physics & applications. Cairo, Egypt, Forschungszentrum Juelich GmbH, Bilateral Seminars of the International Bureau, v. 34, 2003, 240–243.
- Wisbrun R., Schechter I., Niessner R., and Shröder H. Laser induced breakdown spectroscopy for detection of heavy metals in environmental samples. *SPIE*, 1992, v. 1716 (SPIE, Bellingham, Washington), 2–14.
- Colao F., Barbini R., Fantoni R., Lazic V., Palucci A., Capitelli F., and van der Steen H.J.L. Laser induced breakdown spectroscopy for semi-quantitative elemental analysis in soils and marine sediments. *EARSeL Conference Proceeding*, Dresden, Germany, 1999.
- Barbini R., Colao F., Fantoni R., Palucci A., Ribezzo S., van der Steen H.J.L., and Angelone M. Semi-quantitative time resolved LIBS measurements. *Appl. Phys. B*, 1997, v. 65, 101–107.
- Barbini R., Colao F., Fantoni R., Palucci A., and Capitelli F. Application of laser induced breakdown spectroscopy to the analysis of metals in soils. *Appl. Phys. A*, 1999, v. 69, 175–179.
- Bulatov V., Krasniker R., and Schechter I. Study of matrix effects in laser plasma spectroscopy by combined multifiber spatial and temporal resolutions. *Anal. Chem.*, 1998, v. 70, 5302–5310.

9. Sabsabi M., Detalle V., Harith M.A., Tawfik W., and Imam H. Comparative study of two new commercial Echelle spectrometers equipped with intensified CCD for analysis of laser-induced breakdown spectroscopy. *Applied Optics*, 2003, v. 42, No. 30, 6094–6098.
10. Ismail M.A., Imam H., Elhassan A., Youniss W.T., and Harith M.A. LIBS limit of detection and plasma parameters of some elements in two different metallic matrices. *J. Anal. At. Spectrom.*, 2004, v. 19, 1–7.
11. Xu L., Bulatov V., Gridin V., and Schechter I. Absolute analysis of particulate materials by laser-induced breakdown spectroscopy. *Anal. Chem.*, 1997, v. 69, 2103–2108.
12. Goode S.R., Morgan S.L., Hoskins R., and Oxsher A. Identifying alloys by laser-induced breakdown spectroscopy with a time-resolved high resolution echelle spectrometer. *J. Anal. At. Spectrom.*, 2000, v. 15, 1133–1138.
13. Eppler A.S., Cremers D.A., Hickmott D.D., Ferris M.J., and Koskelo A.C. Matrix effects in the detection of Pb and Ba in soils using laser-induced breakdown spectroscopy. *Appl. Spectrosc.*, 1996, v. 50, 1175–1181.
14. Quentmeier A., Sdorra W., and Niemax K. Internal standardization in laser induced fluorescences spectrometry of micro-plasmas produced by laser ablation of solid samples. *Spectrochimica Acta B*, 1990, v. 45, No. 6, 5371–5379.
15. Tawfik W. Quantitative elemental analysis of seawater by laser induced breakdown spectroscopy. *Intern. J. of Pure and Applied Physics*, 2006, v. 2, No. 1, 11–21.
16. Ciucci A., Corsi M., Palleschi V., Rastelli S., Salvetti A., and Tognoni E. A new procedure for quantitative elemental analyses by laser induced plasma spectroscopy. *Applied Spectroscopy*, 1999, v. 53, 960–964.
17. Bulajic D., Corsi M., Cristoforetti G., Legnaioli S., Palleschi V., Solvetti A., and Rognoni E. A procedure for correcting self-absorption in calibration-free laser induced breakdown spectroscopy. *Spectrochim. Acta B*, 2002, v. 57, 339–353.
18. Corsi M., Palleschi V., Salvetti A., and Tognoni E. Making LIBS quantitative: a critical review of the current approaches to the problem. *Res. Adv. Appl. Spectrosc.*, 2000, v. 1, 41–47.
19. Olesik J.W. Echelle grating spectrometers for inductively coupled plasma-optical emission spectrometry. *Spectroscopy*, 1999, v. 14, No. 10, 27–30.
20. Simeonsson J.B. and Miziolek A.W. Time-resolved emission, studies of ArF laser-produced micro plasmas. *Appl. Opt.*, 1993, v. 32, 939–947.
21. Griem H.R. *Plasma spectroscopy*. McGraw-Hill, N.Y., 1964.
22. NIST National Institute of Standards and Technology, USA. Electronic database, http://physics.nist.gov/PhysRefData/ASD/lines_form.html.
23. Kurucz Atomic Line Database, <http://www.cfa.harvard.edu/amdata/ampdata/kurucz23/sekur.html>.
24. Lida Y. Effects of atmosphere on laser vaporization and excitation processes of solid samples. *Spectrochim. Acta B*, 1990, v. 45, 1353–1367.
25. Nemet B. and Kozma L. Time-resolved optical emission spectrometry of Q-switched Nd: YAG laser-induced plasmas from copper targets in air at atmospheric pressure. *Spectrochim. Acta B*, v. 50, 1869–1888.
26. Kyuseok Song, Hyungki Cha, Jongmin Lee, and Yong Lee. Investigation of the line-broadening mechanism for laser-induced copper plasma by time-resolved laser-induced breakdown spectroscopy. *Microchemical J.*, 1999, v. 63, 53–60.
27. Lazic V., Colao F., Barbini R., Fantoni R., and Palucci A. Self-absorption model in quantitative laser induced breakdown spectroscopy measurements on soils and sediments. *Spectrochimica Acta B*, 2001, v. 56, 807–820.
28. Sabsabi M. and Cielo P. Quantitative analysis of aluminum alloys by laser-induced breakdown spectroscopy and plasma characterization. *Applied Spectroscopy*, 1995, v. 49, No. 4, 499–507.
29. Samek O., Beddows D.C.S., Telle H.H., Kaiser J., Liska M., Caceres J.O., and Gonzales Urena A. Quantitative laser-induced breakdown spectroscopy analysis of calcified tissue samples. *Spectrochimica Acta B*, 2001, v. 56, 865–875.
30. Tankosic D., Popovic L.C., and Dimitrijevic M.S. The electron-impact broadening parameters for Co III spectral lines. *Astronomy and Astrophysics*, 2003, v. 399, 795–797.
31. Popovic L.C. and Dimitrijevic M.S. Tables of the electron impact broadening parameters: Mn II, Mn III, Ga III, Ge III and Ge IV Lines. *Bull. Astron. Belgrade*, 1997, No. 156, 173–178.
32. Dunaevsky A., Chirko K., Krasik Ya.E. and Felsteiner J. Spectroscopy of a ferroelectric plasma cathode. *J. Appl. Phys.*, 2001, v. 90, No. 8, 4108–4114.

Search for Anisotropic Light Propagation as a Function of Laser Beam Alignment Relative to the Earth's Velocity Vector

C. E. Navia, C. R. A. Augusto, D. F. Franceschini, M. B. Robba and K. H. Tsui

Instituto de Física Universidade Federal Fluminense, 24210-346, Niterói, RJ, Brazil

Corresponding author: C. E. Navia. E-mail: navia@if.uff.br

A laser diffraction experiment was conducted to study light propagation in air. The experiment is easy to reproduce and it is based on simple optical principles. Two optical sensors (segmented photo-diodes) are used for measuring the position of diffracted light spots with a precision better than $0.1 \mu\text{m}$. The goal is to look for signals of anisotropic light propagation as function of the laser beam alignment to the Earth's motion (solar barycenter motion) obtained by COBE. Two raster search techniques have been used. First, a laser beam fixed in the laboratory frame scans in space due to Earth's rotation. Second, a laser beam mounted on a turntable system scans actively in space by turning the table. The results obtained with both methods show that the course of light rays are affected by the motion of the Earth, and a predominant first order quantity with a $\Delta c/c = -\beta(1 + 2a)\cos\theta$ signature with $\bar{a} = -0.393 \pm 0.032$ describes well the experimental results. This result differs in amount of 21% from the Special Relativity Theory prediction and that supplies the value of $a = -\frac{1}{2}$ (isotropy).

1 Introduction

There are several physical reasons, theoretical and experimental, that could justify a search for anisotropies in light propagation. It is well known that Lorentz and Poincaré were the first ones to build the major part of the relativity theory on the basis of the ether concept as an inertial rest frame, and it is compatible with the Einstein's Special Relativity Theory (SRT). There are also some test theories of SRT, where the Lorentz transformations are modified. For example, an ether theory that maintains the absolute simultaneity and is kinematically equivalent to Einstein SRT was constructed [1]. These test theories are considered useful to examine potential alternatives to SRT. On the other hand, the reconstruction of the SRT, on the basis of the Lorentz-Poincaré scheme implies in an undetectable ether rest frame (non ether drift) at least in the first order [2].

This behavior of the Lorentz-Poincaré, as well as, of the Einstein theories arise because they do not govern the whole physics, for instance they do not involve gravitation. It is also well known that the presence of a gravitational field breaks the Lorentz symmetry.

On the other hand, periodic boundary conditions or close space-time topology, such as the Sagnac effect [3] where two opposite light beams travel in different time intervals the same closed path on a rotating disk, as well as the twin paradox, leads to preferred frame effects. This assumption of a preferred frame comes from an analysis made by Brans and Stewart [4] on the twin paradox, where a description of the close topology of the universe has imposed a preferred state of rest so that the principle of special relativity, although locally valid, is not globally applicable. Similar conclusion is obtained in the Wucknitz's paper [5], where standard nota-

tion of SRT using Lorentz transformations leads to coordinates which are valid locally. Periodic boundary conditions or close space-time topology, such as the Sagnac effect and the twin paradox, leads to preferred frame effects.

The above conclusion is reinforced by the generalized Sagnac effect [6] observed in a light waveguide loop consisting of linearly and circularly segments, any segment of the loop contributes to the phase difference between two counter-propagating light beams in the loop. Showing that the acceleration is not essential to take into account the effect.

A preferred frame emerge also from an analysis on the Global Positioning System (GPS) made by R. Hatch [7] and T. Van Flandern [8] where the preferred frame is not universal, but rather coincides with the local gravity field.

On the other hand, according to Fox [9], it is possible to preserve the general Lorentz Poincaré symmetry group without assuming the constancy of light speed. There are also the so called extended theories, where the SRT is modified in order to including the Planck scale parameters [10] (double relativity theories), suggesting several dispersion relations that include theories where an energy dependent speed of light [11] is claimed.

There are also evidences suggesting that the propagation of light over cosmological distances has anisotropic characteristics [12], with dependence on direction and polarization. This picture is in agreement with the interpretations of the COBE [13] measurements giving the Earth's "absolute" velocity in relation to the uniform cosmic microwave background radiation (CMBR). Of course, there are also interpretations claiming that the COBE measurements give only a velocity for the "relative" motion between the Earth and the CMBR [14]. For instance, it is possible to obtain a "virtual" image, where an isotropic distribution of CMBR with small

fluctuations ($\delta T/T \sim 10^{-5}$) can be seen, by removing the Earth motion.

So far, several tests about violation of the isotropy of the speed of light have been made. In most cases, the tests involve the so called round-trip test of light-speed isotropy like Michelson-Morley experiment and all its variants. Particularly, Miller [15, 16] has claimed a non-null results in the M-M experiments. These aspects are presented in Appendix.

On the other hand, there are also several one-way test of light isotropy experiments. In most cases, they have claimed a null result [17, 18, 19, 20]. Particularly the NASA's Deep Space Network [21] using hydrogen-maser frequency have to obtained a crude bound $\Delta c(\theta)/c < 4.5 \times 10^{-6}$ for the anisotropy of the one way velocity of light and refined to $\Delta c(\theta)/c < 3.5 \times 10^{-7}$. However, according to their own conclusions the validity of these limits rest upon the assumption that the prediction phase variations were not partially canceled. There are also experiments that have claimed success [22, 23]. Particularly, Silvertooth has claimed an experimental detection of the ether drift velocity using a device capable of detecting the beams arriving in opposite directions [23]. Silvertooth reported in 1986 a light anisotropy toward the direction of Leo constellation and compatible with COBE results. The experiment is an unusual double interferometer, an arrangement of light paths and detectors hard to be reproduced. In addition, the presence of a feedback into the laser is quite probable.

In this paper, we report results of a search for anisotropic light propagation as a function of the laser beam alignment relative to the Earth's velocity vector, using a diffraction device. The method is based on simple optical principles. Initial attempts have used digital images of the diffraction spots. However, this method was working in the limit of sensitivity. In other words, the signal's size was close to the measurement resolution. Now, our results are obtained by using the highly sensitive segmented photo-diodes to measure the position of diffracted light spots. In Section 2, the experimental setup and the basic operating principles of the diffractometer are presented. The Earth's velocity vector on the basis of the Doppler shift of the CMBR results are presents in Section 3. In Section 4, the two scanning methods and their results are presented, and finally Section 5 contains our conclusions.

2 Experimental setup and method

The diffraction experiment is installed on the campus of the Universidade Federal Fluminense, Niterói, Rio de Janeiro-Brazil at sea level. The position is given by $22^{\circ}54'33''$ S latitude and $43^{\circ}08'39''$ W longitude. The diffraction experiment is mounted on a horizontal rotating circular table.

The layout of the diffraction device is shown in Fig. 1. A laser beam transverse to a diffraction grating is diffracted in several rays. In order to determine the position of the

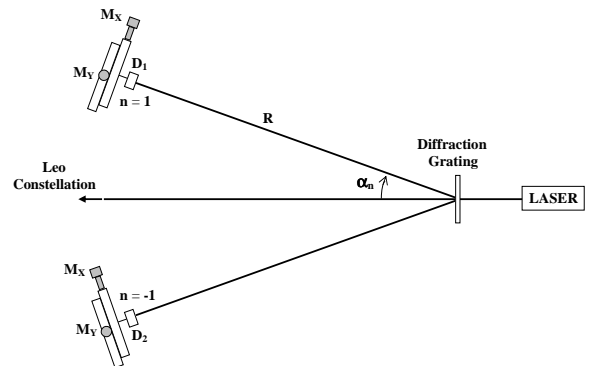


Fig. 1: General layout of the diffraction experiment. Two segmented photo-diodes (D_1 and D_2) are positioned using two vertical platforms with two positioning system (micrometers $M_x - M_y$) to detect two diffracted rays produced by a HE-Ne laser on a grating diffraction device. The relative position of a light spot with respect to the center on a segmented photo-diode is obtained by simply measuring the output current of each segment. The setup is mounted on a turntable system

light spots, we have used two segmented PSD photo-diodes divided into two segments, separated by a gap (see Fig. 2). The position of each photo-diode coincides with the positions of the maxima intensity of the diffraction images, for $n = +1$ and $n = -1$ respectively, as shown in Fig. 1. Two precision multi-axis positioning systems, and each one consist of a vertical platform with two independent ($X-Y$) micrometers, have been used to mount the photo-diodes.

Following Fig. 1, it is possible to see that the maxima of intensity of the diffraction images (rays) satisfy the condition

$$\sin \alpha_n = \pm n \frac{\lambda}{\eta \delta}, \quad \text{with } n = 0, 1, 2, \dots, \quad (1)$$

where $\lambda (= 632.8 \text{ nm})$ is the wave length, $\delta (= 1/600 \text{ mm})$ is the diffraction grating step and $\eta (= 1.000226)$ is the refraction index of air. The wave length λ can be obtained as the ratio between the speed of light c and the light frequency ν resulting in $\lambda = c/\nu$. An expression for c as a function of the angle α can be obtained as

$$c = \frac{\eta \nu \delta}{n} \sin \alpha_n. \quad (2)$$

Under the assumption that ν and η remain constant during the experiment, and if c depends on the direction of propagation, variations of the diffraction spot positions, α_n , for instance, as a function of the laser beam alignment, relative to the Earth's velocity vector, can be interpreted as an indication of violation of the isotropy of c . The relative variation can be expressed as

$$\frac{\Delta c}{c} = \frac{\Delta(\sin \alpha_n)}{\sin \alpha_n} = \cot \alpha_n \Delta \alpha_n. \quad (3)$$

We look for this anisotropic light propagation signal through measurements of $\Delta \alpha_n$ as a function of the Earth's

Observer	Year	v_E , km/s	α , hour	δ , degree
Penzias & Wilson (ground) [27]	1965		I s o t r o p i c	
Conklin (ground) [28]	1969	200 ± 100	13 ± 2	30 ± 30
Henry (balloon) [29]	1971	320 ± 80	10 ± 4	-30 ± 25
Smoot et al. (airplane) [30]	1977	390 ± 60	11.0 ± 0.5	6 ± 10
COBE (satellite) [32]	1991	371 ± 0.5	11.20 ± 0.01	-7.22 ± 0.08
WMAP (satellite) [33]	2003	368 ± 0.2	11.20 ± 0.01	-7.22 ± 0.08

Table 1: Vector velocity of the Earth (solar system) relative to the CMBR rest frame, measured using the anisotropy of the CMBR in several experiments.

velocity vector. The search has been made by using two independent types of scanning, and the methods as well as the results are presented in Section 4.

The determination of the position of the light spots is made by measuring the output photo-current in each segment of the photo-diodes. A symmetric spot, positioned at the center, generates equal photo-currents in the two segments. The relative position is obtained by simply measuring the output current of each segment. The position of a light spot with respect to the center on a segmented photo-diode is found by

$$\Delta l = l_0 \left(\frac{I_1 - I_2}{I_1 + I_2} \right), \quad (4)$$

where l_0 is a proportionality constant. The method offers position resolution better than $0.1 \mu\text{m}$, and the angular variation can be obtained as

$$\Delta\alpha_n = \frac{\Delta l}{R} = \frac{l_0}{R} \left(\frac{I_1 - I_2}{I_1 + I_2} \right). \quad (5)$$

For the diffraction experiment with $R = 30.0 \text{ cm}$, the angular resolution is better than $3.3 \times 10^{-7} \text{ rad}$.

We have used the data acquisition system of the Tupi muon telescope [24, 25, 26], which is made on the basis of the Advantech PCI-1711/73 card. The analog output signal from each segmented photo-diodes is linked to the analog input of the PCI card. The PCI card has 16 analog input channels with a A/D conversion up to 100 kHz sampling rate. All the data manipulations such as the addition and the subtraction of currents are made via software, using the virtual instrument technique. The application programs were written using the Lab-View tools. A summary of the basic circuit is shown in Fig. 2.

3 The Earth's velocity vector

The discovery of a pervasive background radiation from the universe by Penzias and Wilson [27] in 1965 is probably the strongest evidence for the hot Big Bang model. The CMBR is a 2.7 Kelvin thermal black body spectrum with a peak in the micro wave range, and it is considered a relic of the Big Bang. In the past when the Universe was much smaller, the radiation was also much hotter. As the Universe expanded,

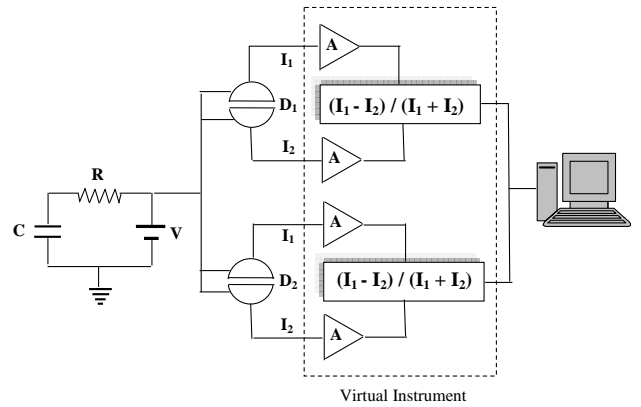


Fig. 2: Block diagram of the diffraction experiment data acquisition system. D_1 and D_2 represent the segment photo-diodes.

it cooled down to the present level.

In Penzias-Wilson's data, the radiation appeared as highly isotropic. However, in the next round of experiments [28, 29, 30] temperature anisotropies were found. These anisotropies are expressed using the spherical harmonic expansion, and the Earth's motion with velocity $\beta = v/c$ relative to the CMBR rest frame of temperature T_0 produces a Doppler shift as

$$\frac{\Delta T}{T_0} = \beta \cos \theta + \frac{\beta^2}{2} \cos 2\theta + O(\beta^3). \quad (6)$$

In Table 1, measurements of the velocity vector of the Earth (solar system) in several experiments in chronological order using the anisotropy of the CMBR are summarized. Southern Hemisphere airborne measurements of the anisotropy in the cosmic microwave background radiation by Smoot and Lubin [31] (1979 — Lima, Peru) are in essential agreement with previous measurements from the northern hemisphere and the first-order anisotropy is readily interpreted as resulting from a motion of the Sun relative to the background radiation.

The COBE data [32] indicate a big temperature anisotropy in the cosmic background radiation which is represented by a dipole form with an amplitude of $\Delta T/T_0 = 1.23 \times 10^{-3} = 0.123\%$. This arises from the motion of the solar system barycenter, with a velocity $v = 371 \pm 0.5 \text{ km/s}$ ($\beta = 0.001237 \pm 0.000002$) at 68%CL, relative to the so called

“CMBR rest frame” and towards a point whose equatorial coordinates are $(\alpha, \delta) = (11.20^{\text{h}} \pm 0.01^{\text{h}}, -7.22^{\circ} \pm 0.08^{\circ})$. This direction points to the Leo constellation. Recently, the WMAP [33] mission has improved the resolution of the angular power spectrum of the CMBR and has verified the COBE results.

4 Raster search techniques

We look for an anisotropy signal in the light propagation as a function of the Earth’s velocity vector. At our latitude ($\sim 23^{\circ}$ S) there are two passages of the Leo constellation on the horizon every 24 hours. The first one is near the West direction, and the second is approximately 12 hours later, and it is near the East direction. Consequently it is possible to mount a laser diffraction experiment on a horizontal turntable system and point the laser beam toward the Leo constellation. The raster search can be made by using two methods as are described below.

4.1 Passive raster search system due to Earth’s rotation

This method consists in to fix the laser beam direction toward the first or second passage of the Leo constellation on the horizon. As the Earth rotates, the laser beam will be aligned to the first or second passage of the Leo constellation (CMBR apex according to COBE) on the horizon over a 24 hour period.

As the laser, the diffraction grating, and the detectors are always fixed, the method is free of mechanical perturbations, which can be introduced, for instance, when the system is rotated. However, the method requires measurements over a long period of time (at least 12 hours) and several days and this introduces the so called DRIFT-long-term timing variation by aging due to temperature variations (diurnal and semi-diurnal temperature dependence). In the case of diffraction experiments, this effect is amplified due to the temperature dependence of the refraction index. Even so, the situation is not critical, because the angular variation of the diffracted rays is obtained from the ratio $(I_1 - I_2)/(I_1 + I_2)$ and the systematic effects tend to the cancel.

There is also the JITTER-timing (short term) noise due to statistical fluctuations of the signal (shot and thermal noises), and they have a “white” frequency distribution, where the spectral power densities are constant.

If the CMBR apex has an altitude, h , and an azimuth angle, θ_A , the projection of the Earth’s velocity, v , on the laser beam direction is

$$v_p = v \cos(\theta_A - \theta_{beam}) \cos h, \quad (7)$$

where θ_{beam} is the azimuth of the laser beam and coincides with the CMBR apex azimuth when it is on the horizon. Consequently, the values $\theta_A = \theta_{beam}$ and $h = 0$ represents the CMBR apex culmination on the horizon.

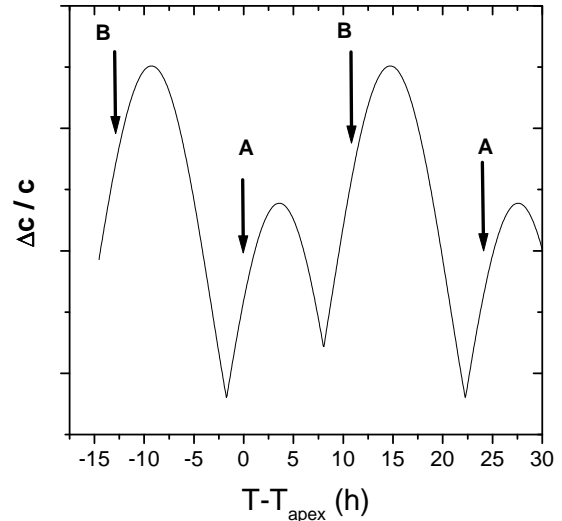


Fig. 3: Expected variation of the one way light speed anisotropy relative to the CMBR dipole direction for a period of 24 hours according to Mausouri and Sexl test theory (with $a \neq -\frac{1}{2}$) and modulated by the altitude variation of the CMBR apex due to Earth rotation. The curve was obtained for the Latitude = 23° S. The vertical arrows A and B indicates the moment of the passage of the CMBR apex for the horizon. In A (B) the laser beam is parallel (anti-parallel) to the Earth velocity vector.

On the other hand, we have analyzed the experimental data using the test theory of Mausouri and Sexl [1]. according to this test theory, the one way speed of light is anisotropic by an among

$$c(\theta) = c - v(1 + 2a) \cos \theta, \quad (8)$$

where θ is the angle between the velocity, v , of the moving system (i.e. the Earth motion) and the direction of light propagation. In our experiment $\theta = \theta_A - \theta_{beam}$. The value $a = -\frac{1}{2}$ correspond to the isotropic SRT prediction, and $a \neq -\frac{1}{2}$ represents an anisotropic signal in the one-way path speed of light. According to Eq. 7 in the passive raster search system, the Mausouri and Sexl equation is modulated by the altitude variation and can be expressed as

$$c(\theta, h) = c - v(1 + 2a) \cos(\theta_A - \theta_{beam}) \cos h, \quad (9)$$

and the relative variation is

$$\Delta c(\theta, h)/c = -\beta(1 + 2a) \cos(\theta_A - \theta_{beam}) \cos h, \quad (10)$$

where $\beta = v/c$. As we know the equatorial coordinates of the CMBR $(\alpha, \delta) = (11.20^{\text{h}} \pm 0.01^{\text{h}}, -7.22^{\circ} \pm 0.08^{\circ})$ according to COBE. The transformation from equatorial coordinate system (α, δ) to the horizontal coordinate system (θ_A, h) permits to obtain a correlation between θ_A and h as

$$h = \arcsin(\sin \phi \sin \delta + \cos \phi \cos \delta \cos H), \quad (11)$$

$$\theta_A = \arcsin(-\cos \delta \sin H / \cos h), \quad (12)$$

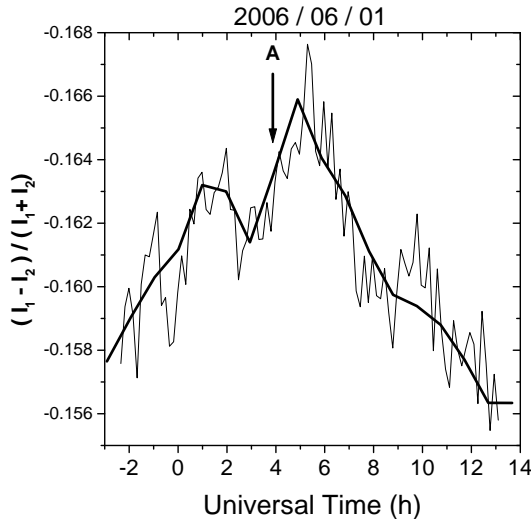


Fig. 4: Histogram obtained in the passive scan system averaging the raw data in blocks of 10 minutes. The vertical arrow indicates the moment of the passage of the CMBR apex (according to COBE) for the horizon. The bold line represent a polynomial fit on the data.

where $\phi (= -23^\circ \text{ S})$ is the latitude and $H (= T - \alpha)$ is the hour angle and T is the sidereal time. Under this conditions, the behavior of $(\Delta c/c)$ given by the Eq. 10 is reproduced in Fig. 3, where the vertical arrows A and B indicates the moment of the passage of the CMBR apex (according to COBE) for the horizon. In A (B) the laser beam is parallel (anti-parallel) to the Earth velocity vector.

In the experiment $\Delta c/c$ is inferred from $\Delta \alpha_n$ measurements (see Eq. 3 and Eq. 5 from Section 2). Examples of raster scans (in the passive mode) were obtained in the first set of measurements (June of 2006) as shown in Fig. 4, Fig. 5 and Fig. 6. Four months after we have repeating the experiment and the result obtained on November of 2006 is shown in Fig. 7. In all cases, built-in a DRIFT-long-term it is possible to see peculiar signatures (see Fig. 3) where the culmination of the CMBR apex on the horizon is between a depression and a peak of the $\Delta c/c$.

In order to extract the Earth's velocity from these experimental data, it is necessary to remove the DRIFT-long-term timing variation, because they are obtained in different days. Meantime this procedure is not free from experimental bias. The calibration will be done in the next search with active rotation which is free of the DRIFT-long-term timing variation.

Before publication of this paper we were informed by V. Gurzadyan [34, 35] of a similar study on anisotropy of the one way velocity of light relative to the dipole of the CMBR based on the Compton edge of laser photons scattered in electron beam at GRAAL ESRF (Grenoble) accelerator, where a similar behavior in the time series was obtained (see Fig. 4 from ref. [35]). However, according to the authors this variations comes probably from temperature variations. We were also informed that is in progress an analysis with new data.

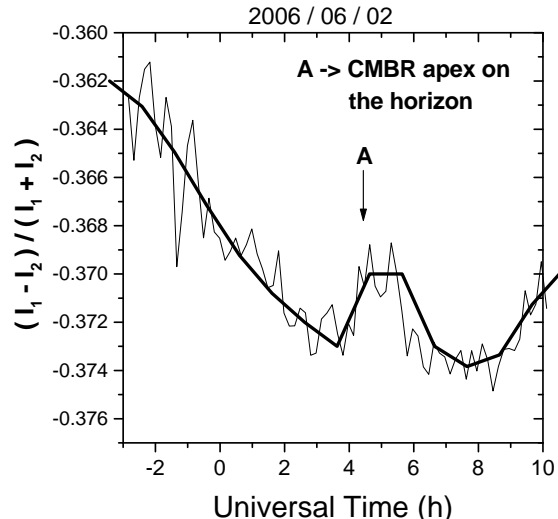


Fig. 5: The same as Fig. 4.

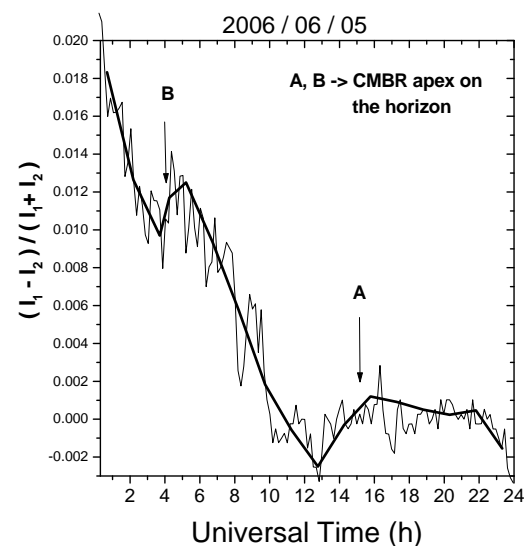


Fig. 6: The same as Fig. 4

4.2 Active raster search with a turntable system

In this active system, the laser beam is first pointed toward the direction of the Leo constellation (CMBR apex) when it is exactly on the horizon. Then the turntable, upon which the entire laser diffraction experiment is mounted, is rotated in steps of 30 degrees up to 180 degrees. At every angular step, the output current of the photo-diodes is registered during one minute at a counting rate of 10 readings per second. A complete set of measurements can be done in less than ten minutes. Consequently the measurements are free from DRIFT-long-term timing variations. They are influenced only by the JITTER-timing uncertainties (noise in the system by statistical fluctuations of the signals). However, this method requires a careful rotation of the system in order to avoid mechanical perturbations. The measurements, after a gaussian fit in the raw data, are shown in Fig. 8 for seven angular

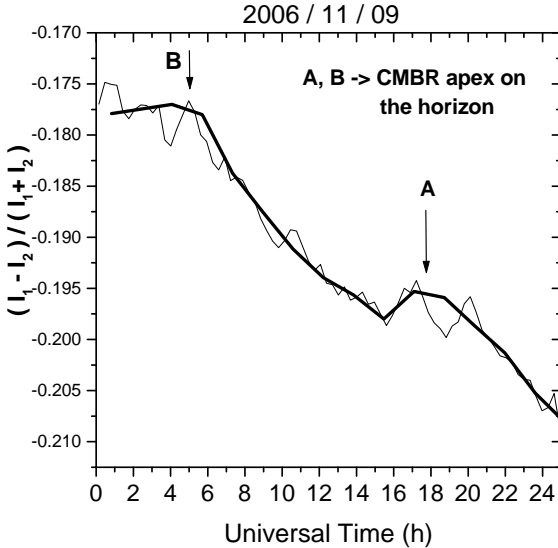


Fig. 7: The same as Fig. 4

regions, and the one-way light path anisotropy can be extracted from

$$\frac{\Delta c}{c} = \cot \alpha \Delta \alpha, \quad (13)$$

with

$$\Delta \alpha = \frac{l_0}{R} \left[\frac{I_1 - I_2}{I_1 + I_2} \right], \quad (14)$$

where the calibration factor obtained for these measurements is $l_0 (= 0.407 \pm 0.034 \text{ mm})$.

We have analyzed the experimental data using also the test theory of Mausouri and Sexl [1] where the one way speed of light is anisotropic by the among

$$c(\theta) = c - v(1 + 2a) \cos \theta. \quad (15)$$

The parameter a can be obtained by fitting the test theory to the experimental results using the expression

$$\frac{\Delta c}{c} = \cot \alpha \Delta \alpha = -\beta(1 + 2a) \cos \theta, \quad (16)$$

where $\beta (= 0.001237 \pm 0.000002)$ is the COBE Earth's velocity parameter. The comparison between our measurements and the test theory is shown in Fig. 9, where an offset such that $(I_1 - I_2)/(I_1 + I_2) = 0$ at $\theta = 90^\circ$ has been used. The experimental results seem to agree to a $\beta(1 + 2a) \cos \theta_A$ signature, and the parameter a extracted from our data is

$$a = -0.4106 \pm 0.0225, \quad (17)$$

which differs from the $a = -\frac{1}{2}$ SRT prediction, as well as, some experimental upper limits using the Mössbauer effect [19].

The measurements above shown were made on June of 2006, they were confirmed in a new set of measurements (including a new calibration) in November of 2006 and the result is presented in Fig. 10. The parameter a extracted from this new data is $a = 0.3755 \pm 0.0403$ in agreement with the previous value.

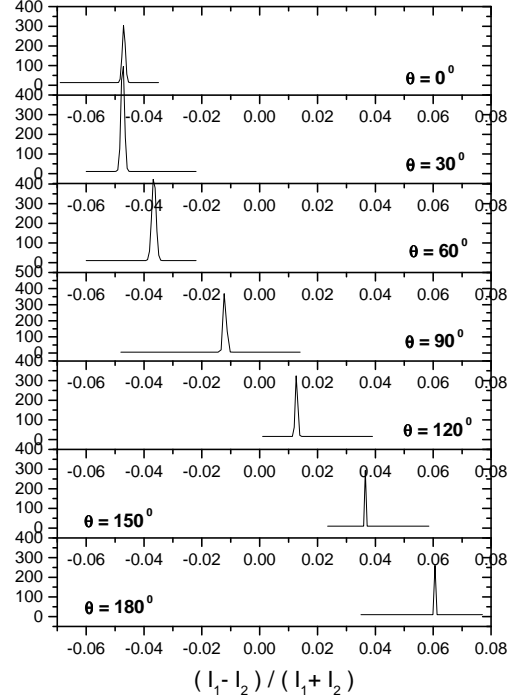


Fig. 8: Counting rate is plotted as a function of $(I_1 - I_2)/(I_1 + I_2)$ at a given laser beam alignment relative to the Earth's velocity vector obtained in June of 2006. The complete set of measurements was made in ten minutes.

5 Conclusions and remarks

The discovery of a dipole anisotropy in the CMBR is interpreted as a Doppler shift produced by the Earth's motion (solar barycenter). An experimental survey has been made in order to test if the Earth's velocity is relevant on light propagation in a quantity of first order. The measurements have been obtained by using a laser diffraction experiment mounted on turntable system. Two optic sensors (segmented photo-diodes) were used for measuring the position of diffracted light spots with a precision better than $0.1 \mu\text{m}$. The experiment is easy to reproduce, and it is based on simple optical principles. Two raster search techniques (scan subjected to Earth's rotation and scan subjected to an active rotation) have been used to look for signals of anisotropic light propagation as a function of the laser beam alignment relative to the Earth's motion. The results obtained with both methods show that the course of the rays is affected by the motion of the Earth. They are susceptible of being interpreted by the test theory of Mausouri and Sexl [1] where the one way speed of light is anisotropic by the amount $c(\theta) = c - v(1 + 2a) \cos \theta$.

In the scan subjected to Earth's rotation, this pure* dependence is modulated by the variation of the altitude, h , of the CMBR apex and expressed as $\Delta c/c = -\beta(1 + 2a) \times \cos(\theta_A - \theta_{beam}) \cos h$. Despite of the statistical fluctua-

*This meas $\cos \theta = \cos(\theta_A - \theta_{beam})$.

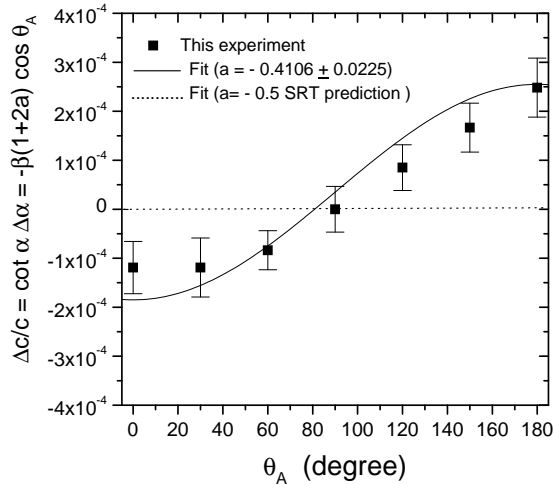


Fig. 9: Comparison between the one-way path light anisotropy $\Delta c/c = -\beta(1+2a) \cos \theta$ function, relative to the Earth's velocity vector and the experimental data obtained in June of 2006, for two different values of the fit parameter, $a = -0.4106$ and $a = -\frac{1}{2}$ respectively. Here $\theta_A = 0$ represent the laser beam pointing to the CMBR apex on the horizon.

tions (short term noise), the results of these scans are in agreement with the prediction of the “modulated” Mousouri and Sexl test theory (with $a \neq -\frac{1}{2}$). In all cases, built-in a DRIFT-long-term it is possible to see peculiar signatures (see Fig. 3) where the culmination of the CMBR apex on the horizon is between a depression and a peak of the $\Delta c/c$.

In the scan subjected to an active rotation, the altitude of the CMBR apex is always $h = 0$, because a complete set of measurements can be done in 10 minutes. The azimuth varies from zero to 180 degree relative to the Earth's velocity direction. Consequently it is free from DRIFT-long-term timing variations. In this case, the Mausouri and Sexl parameter is extract from a fit of the data giving $a = -0.4106 \pm 0.0225$ (from data obtained on June 2006), and $a = -0.3755 \pm 0.0403$ (from data obtained on November 2006), and they differs from SRT prediction where $a = -0.5$.

We remark that the CMBR dipole is a frame dependent quantity. According to Scott and Smoot [39], we can thus determine the “absolute rest frame” of the universe as that in which the CMBR dipole would be zero. In short, our results point out that it is not possible to neglect the preferred frame imposed by cosmology.

Acknowledgements

This paper is a memorial tribute to our professor and friend C. M. G. Lattes, who introduced us the non-conventional aspects of relativity. We are thankful to all the members of the laboratory of Thin Films of IF-UFF for implementing the techniques of using segmented photo-diodes. One of the authors (C.E.N) is thankful to R. Wang for the critics and useful comments.

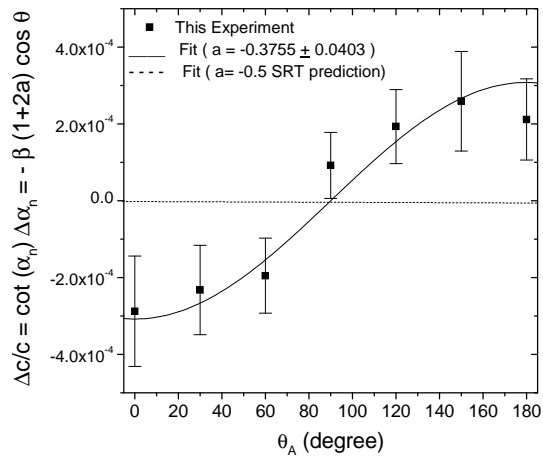


Fig. 10: The same as Fig. 9.

Appendix: The Miller's ether drift direction

According to the theories that incorporate the length contraction principle (Einstein and Lorentz-Poincaré theories), experiments where two orthogonal light paths are compared (two way speed experiments) like the Michelson-Morley interferometer and all variants are incapable of detecting the Earth's motion (no ether drift) due to the length contraction of the interferometer arm parallel to the direction of the Earth's velocity.

Strictly speaking, a null result is expected only in vacuum where the refractive index is $\eta = 1$. While, if $\eta \neq 1$ the Fresnel's drag effect in the rest frame of the medium (Σ) cancels the effect of the genuine Lorentz transformation to a moving frame (Σ'). Following the Lorentz transformation equations from Σ' with speed v to Σ , and taking into account the Fresnel relation of the speed of light in the medium $c' = c/\eta$, it is possible to obtain the so called two-way speed of light anisotropy as

$$\bar{c}'(\theta) = \frac{2c'(\theta)c'(\theta + \pi)}{c'(\theta) + c'(\theta + \pi)}, \quad (A1)$$

and the relative variation as

$$\frac{\Delta c'(\theta)}{c} = -\frac{v^2}{c^2} \left[\frac{\eta^2 - 1}{\eta^2} \left(1 - \frac{3}{2} \sin \theta^2 \right) \right]. \quad (A2)$$

We can see that the two-way speed of light anisotropy is null only in the case $\eta = 1$ (vacuum). This prediction is in agreement with modern ether drift experiments in vacuum [36, 37], using two cavity-stabilized lasers and whose value is

$$\frac{\Delta c'}{c} \sim 10^{-15}. \quad (A3)$$

In the gaseous mode, for instance air ($\eta = 1.000226$), a maximum value of $\Delta c'/c$ happens in reference axis parallel to Earth's velocity. The tiny fringe shifts, observed in various Michelson-Morley type experiments, represent a non-null

effect for the two-way speed of light anisotropy. Dayton Miller [15, 16] was one of the first few in claiming that the Michelson-Morley data and his own data obtained in the mount Wilson are non-null results. Particularly, the mount Wilson data obtained in 1925–1926 is compatible with an observable Earth velocity of $v \sim 8.5 \pm 1.5$ km/s, when the data is analyzed on the basis of classical physics. While on the basis of a different calibration including the length contraction (see Eq. A2), the Miller result gives speeds for the movement of the Earth, larger than $v > 300$ km/s.

A review of the Dayton Miller's ether drift experiments made by James DeMeo [38] shows indisputable evidence that data collected by Miller was affected by the sidereal period and this is clear proof of a cosmological ether drift effect. However, the Miller's determination of the velocity direction of the Earth does not coincide with the direction obtained by COBE. The Miller's direction for the Earth velocity is almost perpendicular to the direction established by COBE, observing the CMBR anisotropy. In our opinion, Miller's result has the same problem as the first results of the CMBR survey as is shown in Table 1. For instance, both Miller and Conklin have obtained a non-null result on the two-way path light speed anisotropy and the dipole anisotropy of the CMBR, respectively. Nevertheless, both experiments have failed to obtain the coordinates of the Earth's velocity vector direction correctly.

References

1. Mansouri R. M. and Sexl R. U. *Gen. Relativ. & Gravit.*, 1977, v. 8, 497.
2. Lorentz H. A. The theory of electrons:and its applications to the phenomena of light and radiant heat. Dover Phoenix Editions, 2004.
3. Sagnac G. C. R. *Acad. Sci. Paris*, 1913, v. 157, 708.
4. Brans C. H. and Stewart D. R. *Phys. Rev. D*, 1973, v. 8, 1662–1666.
5. Wucknitz O. arXiv: gr-qc/0403111.
6. Wang R., Zheng Y., and Yao A. *Phys. Rev. Lett.*, 2004, v. 93, 143901.
7. Hatch R. R. *Galilean Electrodynamics*, 2002, v. 13, 3.
8. Flandern V. T. Available in <http://metaresearch.org/cosmology/gps-relativity.asp>.
9. Fox V. The theory of the space-time and gravitation. Pergamon, New York, 1964.
10. Amelino-Camelia G. *Phys. Lett. B*, 2001, v. 510, 255.
11. Albrecht A. and Magueijo J. *Phys. Rev. D*, 1999, v. 59, 043516.
12. Nodland B. and Ralston J. P. *Phys. Rev. Lett.*, 1997, v. 78, 3043–3046.
13. Smoot G. F. et al. *Astrophysical Journal*, 1991, v. 371, L1–L5.
14. Yaes R. J. Reconciling COBE data with relativity. *Physics Today*, 1993, March 13.
15. Miller D. C. *Rev. Mod. Phys.*, 1933, v. 5, 203–255.
16. Cahill R. T. *Progress in Physics*, 2005, v. 3, 25.
17. Cialdea R. *Lett. Nuovo Cimento*, 1972, v. 4, 821.
18. Krisher T. P. et al. *Phys. Rev. D*, 1990, v. 42, 731.
19. Turner K. C. and Hill H. A. *Phys. Rev. B*, 1964, v. 252, 134.
20. Gagnon D. R., Torr D. G., Kolen P. T., and Chang T. *Phys. Rev. A*, 1988, v. 38, 1767.
21. Timothy P. et al. *Phys. Rev. D*, 1990, v. 42, 731.
22. Kolen P. T. and Torr D. G. *Found. Phys.*, 1982, Np. 12, 401.
23. Silvertooth E. W. *Spec. Sci. and Tech.*, 1986, v. 10, 3.
24. Navia C. E., Augusto C. R. A., Robba M. B., Malheiro M., and Shigueoka H. *Astrophysical Journal*, 2005, v. 621, 1137.
25. Augusto C. R. A., Navia C. E. and Robba M. B., *Phys. Rev. D*, 2005, v. 71, 103011.
26. Navia C. E., Augusto C. R. A., Tsui K. H. and Robba M. B. *Phys. Rev.*, 2005, v. 72, 103001.
27. Penzias A. A. and Wilson R. W. *Astrophys. Journal*, 1965, v. 142, 419.
28. Conklin E. K. *Nature*, 1969, v. 222, 971.
29. Henry P. *Nature*, 1971, v. 231, 516.
30. Smoot G. F., Gorenstein M. V., and Miller R. A. *Phys. Rev. Lett.*, 1977, v. 39, 898.
31. Smoot G. F. and Lubin P. M. *Astrophysical Journal*, Part 2 – Letters to the Editor, 1979, v. 234, L83.
32. Smoot G. F. and Scoot D. Cosmic Background Radiation. *European. Phys. J.*, 2000, No. 1–4, 145–149.
33. Bennett C. L. et al. *Astrophys. J. Suppl.*, 2003, v. 148, 1.
34. Gurzadyan V. Private communication.
35. Gurzadyan V. et al. *Mod. Phys. Lett.*, 2005, v. 20, 19; arXiv: astro-ph/0410742.
36. Brillet A. and Hall J. L. *Phys. Rev. Lett.*, 1979, v. 42, 549.
37. Müller H., Hermann S., Braxmaier C., Schiller S. and Peters A. *Phys. Rev. Lett.*, 2003, v. 91, 0204001.
38. DeMeo J. Available in <http://www.orgonelab.org/miller.htm>.
39. Scott D. and Smoot G. F. *Journal of Physics*, 2006, v. 33, 238.

Quantization State of Baryonic Mass in Clusters of Galaxies

Franklin Potter* and Howard G. Preston†

**Sciencegems.com, 8642 Marvale Dr, Huntington Beach, CA 92646 USA*

†*15 Vista del Sol, Laguna Beach, CA 92651 USA*

E-mail: *drpotter@lycos.com and †hpres@cox.net

The rotational velocity curves for clusters of galaxies cannot be explained by Newtonian gravitation using the baryonic mass nor does MOND succeed in reducing this discrepancy to acceptable differences. The dark matter hypothesis appears to offer a solution; however, non-baryonic dark matter has never been detected. As an alternative approach, quantum celestial mechanics (QCM) predicts that galactic clusters are in quantization states determined solely by the total baryonic mass of the cluster and its total angular momentum. We find excellent agreement with QCM for ten galactic clusters, demonstrating that dark matter is not needed to explain the rotation velocities and providing further support to the hypothesis that all gravitationally bound systems have QCM quantization states.

1 Introduction

The rotational velocity curves of galaxy clusters [1] are very similar to the rotational velocity curves of individual galaxies, with the rotational velocity value rising rapidly at very small radial distances only to quickly reach an approximately constant velocity for all greater radial distances from about 200 kpc to out beyond 1500 kpc. Newtonian gravitation using only the observed baryonic mass fails to explain the curves both for galaxies and for clusters of galaxies. In clusters, the baryonic mass is predominantly due to the hot intracluster gas that is observed by its free-free X-ray emissions. This gas fraction plus the stellar masses make up the observed baryonic mass of about 10%–15% of the dynamic mass required to explain the rotational velocity curves using Newtonian gravitation, an enormous discrepancy.

Three interesting possible explanations for galactic rotation curves have been proposed: (1) the dark matter hypothesis (DM) introduces non-baryonic matter that is insensitive to all interactions except gravitation, but there has been no detection of any possible form of dark matter; (2) a modified Newtonian dynamics (MOND) effective at all distance scales when the accelerations are less than $1.2 \times 10^{-10} \text{ m/s}^2$, which has been very successful in explaining the rotation and luminosity curves of individual galaxies but has large discrepancies for galaxy clusters [2] in both the cluster core and in the outer regions; (3) quantum celestial mechanics (QCM) derived [3] from the general relativistic Hamilton-Jacobi equation which dictates that all gravitationally bound systems have quantization states. The QCM states are determined by two physical quantities only — the system's total baryonic mass and its total angular momentum. QCM agrees with MOND and the baryonic Tully-Fisher relation for individual galaxies.

In this paper, we compare the QCM predictions for the

baryonic mass for ten galaxy clusters to the detected baryonic masses. Our new result is that the QCM baryonic mass values agree with the measured baryonic values even where DM succeeds and MOND fails. No dark matter is required to explain the observed rotation curves. The baryonic matter in a single QCM quantization state produces the correct rotational velocity for the cluster.

2 Conceptual review of QCM

In a series of papers [3, 4, 5], we derived a Schrödinger-like scalar wave equation from the general relativistic Hamilton-Jacobi equation via a transformation that utilizes the total angular momentum of the gravitationally bound system instead of an angular momentum proportional to Planck's constant. We have shown agreement of its quantization state solutions with the energy states of the planets of the Solar System, of the satellites of the Jovian planets, and of the disk states of galaxies. In a preliminary table-top investigation with a torsion bar system that is now being modified to minimize possible extraneous influences, the QCM predicted quantization states with quantized energy per mass and quantized angular momentum per mass have been detected. The results from the improved apparatus will be reported.

According to QCM, the quantization state energies per orbiting particle mass μ are

$$\frac{E_n}{\mu} = -\frac{G^2 M^4}{2n^2 H_\Sigma^2} \quad (1)$$

where G is the gravitational constant, M is the total mass of the gravitationally bound system, H_Σ is the system's total angular momentum, and n is an integer. Typically, E_n is on the order of $10^{-6} \mu c^2$. Unlike the quantum mechanics of atomic states whereby each electron is in its own quantum state, in QCM there can be billions of stars (i.e., particles)

Cluster	kT , keV	R_{200} , kpc	M_{200} , $\times 10^{14} M_\odot$	v_{kT} , $\times 10^6$ m/s	M , $\times 10^{13} M_\odot$	H_Σ , $\times 10^{70}$ kg \times m 2 /s
A1983	2.18 ± 0.09	1100 ± 140	1.59 ± 0.61	0.65 ± 0.03	1.12 ± 0.21	5.10 ± 1.65
MKW9	2.43 ± 0.24	1006 ± 84	1.20 ± 0.30	0.68 ± 0.08	1.34 ± 0.63	7.00 ± 5.76
A2717	2.56 ± 0.06	1096 ± 44	1.57 ± 0.19	0.70 ± 0.02	1.50 ± 0.17	8.57 ± 1.71
A1991	2.71 ± 0.07	1106 ± 41	1.63 ± 0.18	0.72 ± 0.02	1.68 ± 0.19	10.4 ± 2.0
A2597	3.67 ± 0.09	1344 ± 49	3.00 ± 0.33	0.84 ± 0.02	3.11 ± 0.30	30.7 ± 5.1
A1068	4.67 ± 0.11	1635 ± 47	5.68 ± 0.49	0.95 ± 0.03	5.09 ± 0.64	72.7 ± 16.1
A1413	6.62 ± 0.14	1707 ± 57	6.50 ± 0.65	1.13 ± 0.03	10.2 ± 1.1	$245. \pm 46$
A478	7.05 ± 0.12	2060 ± 110	10.8 ± 1.8	1.16 ± 0.02	11.3 ± 0.8	$294. \pm 36$
PKS0745	7.97 ± 0.28	1999 ± 77	10.0 ± 1.2	1.24 ± 0.05	14.8 ± 2.4	$469. \pm 132$
A2204	8.26 ± 0.22	2075 ± 77	11.8 ± 1.3	1.26 ± 0.04	15.7 ± 2.0	$525. \pm 116$

Table 1: QCM predicted galactic cluster baryonic mass M and angular momentum H_Σ .

in the same QCM state. Also notice that there is no explicit distance dependence in this energy state expression, in sharp contrast to classical mechanics, because the state radial wave function extends over a large range. QCM tells us that gravitationally bound systems, such as planetary systems and galaxies, are quantized systems and that their behavior cannot be fully understood by classical general relativistic dynamics.

QCM has been used also to derive the general expression for the MOND acceleration $a_0 = 1.2 \times 10^{-10}$ m/s 2 , this specific MOND value being an average value for many galaxies. Our general expression is

$$a_0 = \frac{G^3 M^7}{n^4 H_\Sigma^4}, \quad (2)$$

a result which suggests that a_0 would be slightly different for each galaxy instead of being taken as a universal value.

We combine these equations algebraically to solve for M and H_Σ in terms of the measured asymptotic rotational velocity and the MOND acceleration. Assuming that the virial theorem holds for galaxies, the velocity v is derived from Eq. 1 to yield

$$M = \frac{v^4}{G a_0}, \quad H_\Sigma = \frac{v^7}{n G a_0^2}. \quad (3)$$

These expressions hold true for galaxies. In the next section they will be applied to clusters of galaxies and the predicted baryonic mass values will be compared to the dynamic mass values determined from observational data.

3 Galaxy cluster QCM masses

QCM is assumed to have universal application to isolated gravitationally bound systems. To a good approximation, clusters of galaxies are isolated gravitationally bound systems and therefore should demonstrate the quantization states dictated by QCM. In many cases the galaxy clusters have no dominant central mass, with the intragalactic gas

dispersed throughout the cluster. For simplicity, we assume that the cluster system is in the $n = 1$ state, that the virial theorem applies, that $a_0 = 1.2 \times 10^{-10}$ m/s 2 , and that the cluster is approximately a flattened ellipsoid similar to the Local Group [6] that includes our Galaxy and M31. The latter assumption is not strictly required but allows an easy analogy to disk galaxies where we know that QCM and MOND apply extremely well.

We use the ten galaxy clusters analyzed by Arnaud et al. [7] to determine the QCM predicted baryonic mass and angular momentum via Eqs. 3 above. Their radial distance R_{200} is the distance where inside that radius the mean mass density is 200 times the critical density of the universe, and their M_{200} is the total mass within this radius in solar masses M_\odot as determined by a standard NFW universal density profile for a dark matter halo as determined by Navarro et al. [8] from N -body simulations. The kT (keV) represents the spectroscopic temperature of the $0.1 \leq r \leq 0.5 R_{200}$ region, and the velocity v_{kT} comes from these temperatures. Table 1 lists our results for the total baryonic mass M and the total angular momentum H_Σ .

4 Discussion

Our predicted QCM baryonic masses M in Table 1 for the clusters are about a factor of ten smaller (10^{13} vs. 10^{14}) than the dynamic masses M_{200} which were determined by assuming a dark matter NFW profile. There is reasonable agreement between our QCM baryonic mass values and the baryonic masses from the spectroscopic data. There is no need to invoke the gravitational consequences of DM. The galactic cluster is in a QCM quantization state. This result indicates that quantum celestial mechanics determines certain dynamic behavior of galaxies and galactic clusters.

One additional physical quantity we know now is the total baryonic angular momentum of each galactic cluster. This angular momentum value determines all the quantiza-

tion states of the system in which the gas and the individual galaxies (i.e., particles) can occupy. Particles at all radii from the cluster center are in the same angular momentum quantization state. Note that we have assumed that $n = 1$ for each cluster; however, some clusters could have baryonic mass in the $n = 2$ state as well.

QCM has been applied successfully to solar systems, galaxies and clusters of galaxies. The results strongly suggest that the known baryonic mass in each system is sufficient to explain the rotational velocity values without invoking the gravitational consequences of dark matter. As expected from QCM, these gravitationally bound systems all behave as non-classical systems exhibiting quantization states determined by the total mass and the total angular momentum.

References

1. Pointecouteau E., Arnaud M. and Pratt G. W. The structural and scaling properties of nearby galaxy clusters: I — The universal mass profile. arXiv: astro-ph/0501635.
2. Pointecouteau E. and Silk J. New constraints on MOND from galaxy clusters. arXiv: astro-ph/0505017.
3. Preston H. G. and Potter F. Exploring large-scale gravitational quantization without \hbar in planetary systems, galaxies, and the Universe. arXiv: gr-qc/0303112.
4. Potter F. and Preston, H.G. Gravitational lensing by galaxy quantization states. arXiv: gr-qc/0405025.
5. Potter F. and Preston H. G. Quantum Celestial Mechanics: large-scale gravitational quantization states in galaxies and the Universe. *1st Crisis in Cosmology Conference: CCC-I*, Lerner E.J. and Almeida J. B., eds., AIP CP822, 2006, 239–252.
6. Pasetto S. and Chiosi C. Planar distribution of the galaxies in the Local Group: a statistical and dynamical analysis. arXiv: astro-ph/0611734.
7. Arnaud M., Pointecouteau E. and Pratt G. W. The structural and scaling properties of nearby galaxy clusters — II. The $M - T$ relation. *Astron. & Astrophys.*, v. 441, 2005, 893; arXiv: astro-ph/0502210.
8. Navarro J., Frenk C. S. and White S. D. M. A universal density profile from hierarchical clustering. *Astrophys. J.*, 1997, v. 490, 493.

Experimental Investigations of the Existence of a Local-Time Effect on the Laboratory Scale and the Heterogeneity of Space-Time

Victor A. Panchelyuga*, Valeri A. Kolombet*, Maria S. Panchelyuga* and Simon E. Shnoll*,†

*Institute of Theor. and Experim. Biophysics, Russian Acad. of Sciences, Pushchino, Moscow Region, 142290, Russia

†Department of Physics, Moscow State University, Moscow 119992, Russia

Corresponding authors. Victor A. Panchelyuga: panvic333@yahoo.com; Simon E. Shnoll: shnoll@iteb.ru

The main subject of this work is an experimental investigation of the existence of a local-time effect on the laboratory scale, i.e. longitudinal distances between locations of measurements from one metre to tens of metres. A short review of our investigations of the existence of a local-time effect for longitudinal distances from 500 m to 15 km is also presented. Besides investigations of the minimal spatial scale for a local-time effect, the paper presents investigations of the effect in the time domain. In this relation the structure of intervals distribution in the neighbourhood of local-time peaks was studied and splitting of the peaks was revealed. Further investigations revealed second order splitting of local-time peaks. From this result it is concluded that space-time heterogeneity, which follows from the local-time effect, probably has fractal character. The results lead to the conclusion of sharp anisotropy of space-time.

1 Introduction

Our previous works [1–4] give a detailed description of macroscopic fluctuations phenomena, which consists of regular changes in the fine structure of histogram shapes built on the basis of short samples of time series of fluctuations in different process of any nature — from biochemical reactions and noises in gravitational antennae to fluctuations in α -decay rate. From the fact that fine structure of histograms, which is the main object of macroscopic fluctuation phenomena investigations, doesn't depend on the qualitative nature of the fluctuating process, so it follows that the fine structure can be caused only by the common factor of space-time heterogeneity. Consequently, macroscopic fluctuation phenomena can be determined by gravitational interaction, or as shown in [5, 6], by gravitational wave influence.

The present work was carried out as further investigations into macroscopic fluctuation phenomena. The local time effect, which is the main subject of this paper, is synchronous in the local time appearance of pairs of histograms with similar fine structure constructed on the basis of measurements of fluctuations in processes of different nature at different geographical locations. The effect illustrates the dependence of the fine structure of the histograms on the Earth's rotation around its axis and around the Sun.

The local time effect is closely connected with space-time heterogeneity. In other words, this effect is possible only if the experimental setup consists of a pair of separated sources of fluctuations moving through heterogeneous space. It is obvious that for the case of homogeneous space the effect doesn't exist. Existence of a local-time effect for some space-time scale can be considered as evidence of space-time heterogeneity, which corresponds to this scale. Dependence

of a local-time effect on the local time or longitudinal time difference between places of measurements leads to the conclusion that space heterogeneity has axial symmetry.

The existence of a local time effect was studied for different distances between places of measurement, from a hundred kilometres up to the largest distance possible on the Earth (~ 15000 km). The goal of the present work is an investigation of the existence of the effect for distances between places of measurements ranging from one metre up to tens of metres. Such distances we call “laboratory scale”.

2 Experimental investigations of the existence of a local-time effect for longitudinal distances between places of measurements from 500 m to 15 km

The main problem of experimental investigations of a local-time effect at small distances is resolution enhancement of the macroscopic fluctuations method, which is defined by histogram duration. All investigations of a local-time effect were carried out by using α -decay rate fluctuations of ^{239}Pu sources. Histogram durations in this case are one minute. But such sources of fluctuations become uselessness for distances in tens of kilometres or less when histogram durations must be about one second or less. For this reason in work [7–8] we rejected α -decay sources of fluctuations and instead used as a source, noise generated by a semiconductor diode. Diodes give a noise signal with a frequency band of up to tens of megahertz and because of this satisfy the requirements of the present investigations.

To check the suitability of the selected diode noise source for local-time effect investigations, comparative tests were made at distances for which existence of the effect was proved by using α -decay sources of fluctuations [7]. This

work confirmed the suitability of diode semiconductor noise for studies of the local-time effect.

Below we present a short description of our experiments for investigation of a local-time effect for longitudinal distances of 500 m up to 15 km between locations of measurements. The first experiment studied the local-time effect for a longitudinal distance of 15 km between locations of measurements, the second one for a set of longitudinal distances from 500 m to 6 km. A more detailed description of these experiments is given in [8].

In the first experiment a series of synchronous measurements were carried out in Pushchino (Lat. $54^{\circ}50.037'$ North, Lon. $37^{\circ}37.589'$ East) and Bolshevik (Lat. $54^{\circ}54.165'$ North, Lon. $37^{\circ}21.910'$ East). The longitudinal difference α between places of measurements was $\alpha = 15.679'$. This value of α corresponds to a difference of local time $\Delta t = 62.7$ sec and longitudinal distance $\Delta l = 15$ km.

To study the local-time effect in Pushchino and Bolshevik, we obtained 10-minute time series by digitizing fluctuations from noise generators with a sampling frequency of 44100 Hz. From this initial time series with three different steps of 735, 147 and 14 points, we extracted single measurements and obtained three time series with equivalent frequency equal 60 Hz, 300 Hz and 3150 Hz. On the basis of this time series, in a standard way [1–3] using a 60-point sample length for the first and second time series and a 63-point sample length for third time series, we constructed three sets consisting of histograms with duration 1 sec, 0.2 sec and 0.02 sec.

Fig. 1a depicts the intervals distribution obtained after comparisons of the 1-sec histogram sets. The distribution has a peak, which corresponds to a time interval of 63 ± 1 sec, and which accurately corresponds to a local time difference $\Delta t = 62.7$ sec between places of measurements.

Local time peaks ordinarily obtained on the interval distributions are very sharp and consist of 1–2 histograms [1–3] i.e. are practically structureless. The peak in Fig. 1a can also be considered as structureless. This leads us to the further investigation of its structure.

The fact that all sets of histograms were obtained on the basis of the same initial time series on the one hand, enables enhancement of time resolution of the method of investigation, and on the other hand, eliminates necessity of very precise and expensive synchronization of spaced measurements. The intervals distribution obtained for the 1-sec histograms set allows the use of information about the location of a local-time peak alignment of time series. The alignment makes possible the use of the set of histograms of the next order of smallness.

Using the 0.2-sec histograms set increased resolution five times and allowed more detailed investigations of local-time peak structure and its position on the time axis. Since the positions of the peak on the 1-sec intervals distribution (Fig. 1a) are known, it is possible to select their neighbour-

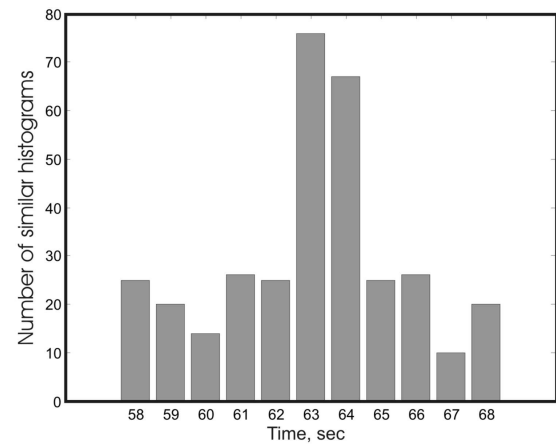


Figure 1a

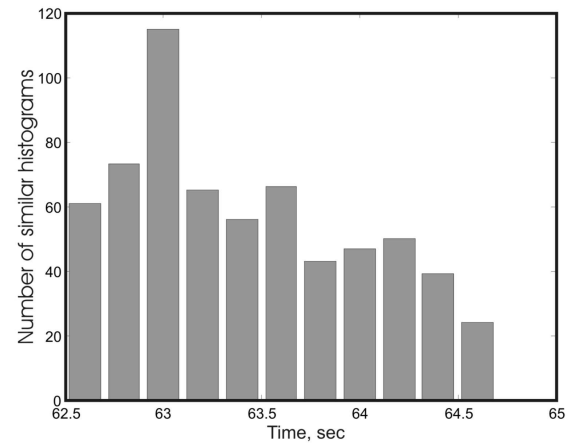


Figure 1b

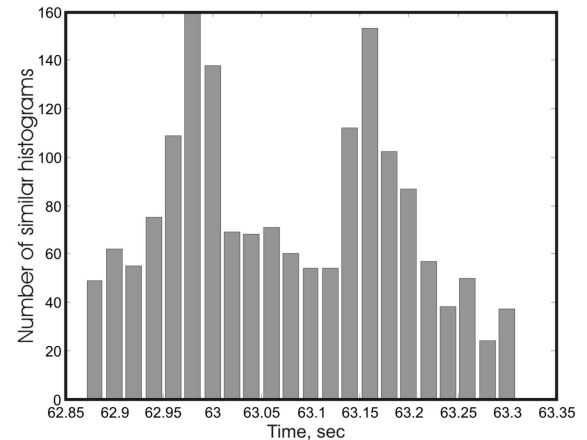


Figure 1c

Fig. 1: Intervals distributions obtained after comparisons of 1-sec (a), 0.2-sec (b), and 0.02-sec (c) histogram sets. The Y-axis depicts the number of histograms, which were found to be similar; the X-axis — time interval between pairs of histograms, sec.

hood by means of 60 sec relative shift of initial time series and prepare after this a 0.2-sec histograms set for further comparison.

The intervals distribution obtained from comparisons for the 0.2-sec histograms set is presented in Fig. 1b. One can see that maximum similarity of histogram shape occurs for pairs of histograms separated by an interval of 63 ± 0.2 sec. This value is the same as for the 1-sec histogram intervals distribution, but in the latter case it is defined with an accuracy of 0.2 sec.

It's easy to see from the intervals distribution, Fig. 1b, that after fivefold enhancement of resolution, the distribution has a single sharp peak again. So a change of time scale in this case doesn't lead to a change of intervals distribution. This means that we must enhance the time resolution yet again to study the local time peak structure. We can do this by using the 0.02-sec histograms set.

The intervals distribution for the case of 0.02-sec histograms is presented in Fig. 1c. Unlike the intervals distributions in Fig. 1a and in Fig. 1b, distribution in Fig. 1c consists of two distinct peaks. The first peak corresponds to a local time difference of 62.98 ± 0.02 sec, the second one to 63.16 ± 0.02 sec. The difference between the peaks is $\Delta t' = 0.18 \pm 0.02$ sec.

Splitting of the local-time peak in Fig 1c is similar to splitting of the daily period in two peaks with periods equal to solar and sidereal days [9–11]. This result will be considered in the next section.

The experiment described above demonstrates the existence of a local-time effect for longitudinal distance between locations of measurements at 15 km, and splitting of the local-time peak corresponding to that distance. It is natural to inquire as to what is the minimum distance for the existence of a local time effect. The next step in this direction is the second experiment presented below.

In this experiment two measurement systems were used: stationary and mobile. Four series of measurements were carried out. The longitudinal differences of locations of stationary and mobile measurement systems was 6 km, 3.9 km, 1.6 km and 500 m. The method of experimental data processing used was the same as for first experiment. It was found that for each of foregoing distances, a local-time effect exists and the local-time peak splitting can be observed.

3 Second-order splitting of the local-time peak. Preliminary results

Four-minute splitting of the daily period of repetition of histogram shape on solar and stellar sub-periods was reported in [3]. In that paper the phenomenon is considered as evidence of existence of two preferential directions: towards the Sun and towards the coelosphere. After a time interval of 1436 min the Earth makes one complete revolution and the measurement system plane has the same direction in space as one

stellar day before. After four minutes from this moment, the measurement system plane will be directed towards the Sun. This is the cause of a solar-day period — 1440 min.

Let us suppose that the splitting described in the present paper has the same nature as splitting of the daily period. Then from the daily period splitting $\Delta T = 4$ min it is possible to obtain a constant of proportionality k :

$$k = \frac{240 \text{ sec}}{86400 \text{ sec}} \approx 2.78 \times 10^{-3}. \quad (1)$$

The longitudinal difference between places of measurements presented in the second section is $\Delta t = 62.7$ sec and we can calculate splitting of the local-time peak for this value of Δt :

$$\Delta t' = k \Delta t = 62.7 \times 2.78 \times 10^{-3} \approx 0.17 \text{ sec}. \quad (2)$$

It is easy to see from Fig. 1c that splitting of the local-time peak is amounts to 0.18 ± 0.02 sec. This value agrees with estimation (2). Values of splitting of the local-time peak, which were obtained for the mobile experiment, are also in good agreement with values obtained by the help of formula (2).

This result allows us to consider sub-peaks of local-time peak as stellar and solar and suppose that in this case the cause of splitting is the same as for daily-period splitting. But the question about local-time peak structure remains open.

In order to further investigations of the local-time peak structure an experiment was carried out using synchronous measurements in Rostov-on-Don (Lat. $47^{\circ}13.85'$ North, Lon. $39^{\circ}44.05'$ East) and Bolshevik (Lat. $54^{\circ}54.16'$ North, Lon. $37^{\circ}21.91'$ East). The local-time difference for these locations of measurements is $\Delta t = 568.56$ sec. The value of the local-time peak splitting, according to (2), is $\Delta t' = 1.58$ sec. The method of experimental data processing was the same as described in section 2.

In Fig. 2, a summation of all results of expert comparison is presented. For the considered case we omit presentation of our results in the form of interval distributions, like those in Fig 1, because it involves multiplicity graphs.

Fig. 2 consists of four lines. At the leftmost side of each line is the duration of a single histogram in the four sets of histograms, which were prepared for comparison. So we have four sets consisting of 1-sec, 0.2-sec, 0.0286-sec and 1.36 ms histograms. The rectangle in the first line schematically shows a local-time peak, obtained as a result of comparisons for the 1-sec histograms set. Taking into account synchronization error (about one second), the result is 567 ± 2 sec. This value is in agreement with the calculated longitudinal difference of local time $\Delta t = 568.56$ sec (throughout Fig. 2, calculated values are given in parentheses).

The second line in Fig. 2 presents results for the 0.2-sec histograms set. The values in the rectangles show sidereal and solar sub-peaks of the local-time peak. The value between

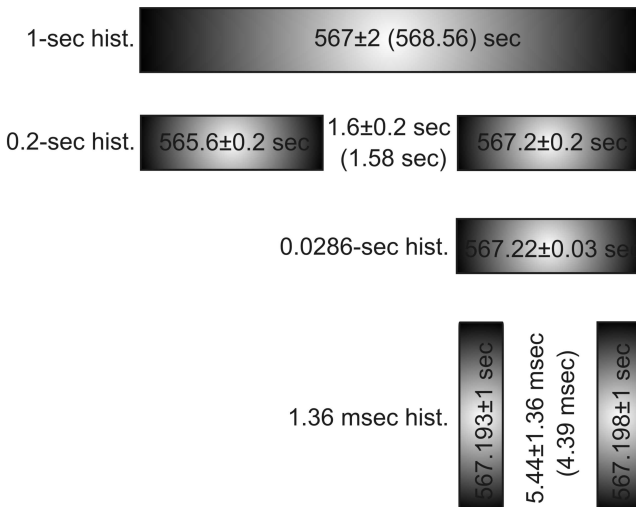


Fig. 2: Local-time peak splitting obtained in the experiment with synchronous measurements of fluctuations of a pair of semiconductor noise generators, carried out in Rostov-on-Don and Bol'shevsk.

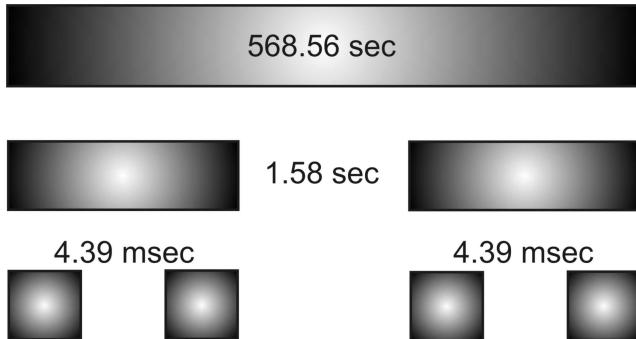


Fig. 3: Expected structure of local-time peak splitting for experiment with synchronous measurements in Rostov-on-Don and Bol'shevsk, calculated on the base of formula (4).

the rectangles give the splitting of the local-time peak. The experimentally obtained splitting value is 1.6 ± 0.2 sec, which is in good agreement with the value calculated on the basis of formula (2).

The third and fourth lines of Fig. 2 present the results of additional investigations of local-time peak structure. In the third line is the result of comparisons of the 0.0286-sec histograms set for intervals, which constitute the closest neighbourhood of 567.2 ± 0.2 -sec peak. Using the 0.0286-sec histograms set increased resolution almost ten times and defines peak position on the intervals distribution at 567.22 ± 0.03 sec. The obtained peak is structureless. Further increase of resolution moves to the 1.36-ms histograms set, presented in fourth line. In this case resolution enhancement revealed splitting of 567.22 ± 0.03 sec peak.

The splitting presented in last line of the diagram, can be regarded as second-order splitting. It can be calculated

using first-order splitting $\Delta t' = 1.58$ sec by the analogue of formula (2):

$$\Delta t'' = k\Delta t'. \quad (3)$$

It is easy to see from (3) and from Fig. 2, for second-order splitting $\Delta t''$ the value of first-order splitting $\Delta t'$ plays the same rôle as the local-time value Δt for $\Delta t'$. Numerical calculations using (3) gives $\Delta t'' = 4.39$ ms, which is in good agreement with the experimentally obtained splitting value 5.44 ± 1.36 ms.

Experimental evidence for the existence of second-order splitting leads us to conjecture the possibility of n -order splitting. It is easy to see from (2) and (3) that the n -order splitting value Δt^n can be obtained in the following way:

$$\Delta t^n = k^n \Delta t. \quad (4)$$

Fig. 3 presents an idealized structure of local-time peak splitting for the considered experiment, which was calculated on the base of formula (4). Unlike Fig. 2, the structure of local-time peak splitting in Fig. 3 is symmetrical. Studies of a possible splitting of 565.6 ± 0.2 sec peak is our immediate task. At this time the results presented in the Fig. 2 can be considered as preliminary.

4 Experimental investigations of the existence of a local-time effect for longitudinal distances between places of measurements from 1 m to 12 m

The experiments described in two previous sections demonstrate the existence of a local-time effect for a longitudinal distance of 500 m between locations of measurements, and the existence of second-order splitting of the local-time peak. The next step in our investigations is a study of the local-time effect on the laboratory scale.

The main difference between local-time effect investigations on the laboratory scale and the experiments described above is an absence of a special synchronization system. In the laboratory case the experimental setup consists of two synchronous data acquisition channels and two spaced noise generators, which are symmetrically connected to it. A LeCroy WJ322 digital storage oscilloscope was used for data acquisition. Standard record length of the oscilloscope consists of 500 kpts per channel. This allowed obtaining of two synchronous sets of 50-point histograms. The maximum length of every set is 10000 histograms.

Fig. 4 presents values of local time shift as a function of distance between two noise generators. The graph presents the results of investigations of a local-time effect for distances of 1 m, 2 m, 3 m, and 12 m. Local-time values were found with an accuracy of 9.52 ms for the 12 m experiments and with an accuracy of 1.36 ms for the 1 m, 2 m, and 3 m experiments.

An example of an intervals distribution for 1 m longitudinal distance between two noise generators is presented in

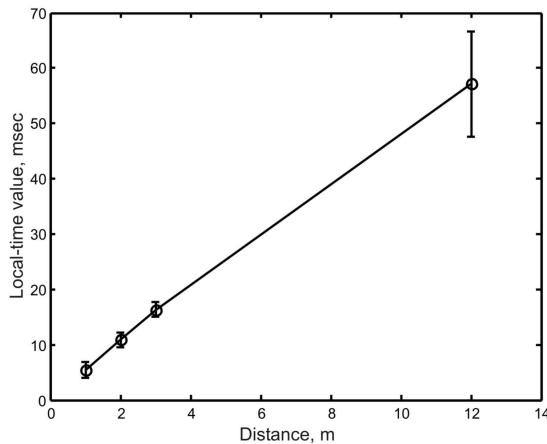


Fig. 4: Values of local time shift as a function of distance between two sources of fluctuations. The graph presents investigations of the local-time effect for distances 1 m, 2 m, 3 m, and 12 m.

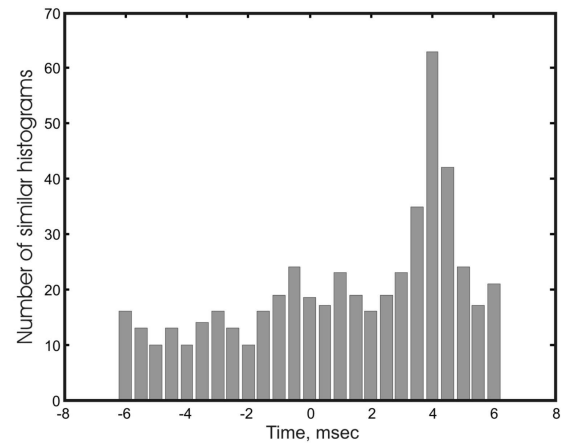


Fig. 5: Example of intervals distribution for longitudinal distance between two sources of fluctuations at one metre separation. Single histogram duration — 0.5 ms.

Fig. 5. The intervals distribution was obtained on the basis of the 0.5-ms histograms set. Using the Earth's equatorial radius value (6378245 m) and the latitude of the place of measurements ($54^{\circ}50'0.37'$), it is possible to estimate the local-time difference for a 1m longitudinal distance. The estimated value is 3.7 ms. It is easy to see from Fig. 5 that the experimentally obtained value of local-time peak is 4 ± 0.5 ms, which is in good agreement with the theoretical value.

The results of our investigations for the laboratory scale, which are presented in this section, confirm a local-time effect for distances up to one metre. So we can state that a local-time effect exists for distances from one metre up to thousands of kilometers. This is equivalent to the statement that space heterogeneity can be observed down to the 1m scale.

5 Discussion

Local-time effect, as pointed out in [1], is linked to rotational motion of the Earth. The simplest explanation of this fact is that, due to the rotational motion of the Earth, after time Δt , measurement system No. 2 appears in the same place where system No. 1 was before. The same places cause the same shape of fine structure of histograms. Actually such an explanation is not sufficient because of the orbital motion of the Earth, which noticeably exceeds axial rotational motion. Therefore measurement system No. 2 cannot appear in the same places where system No. 1 was. But if we consider two directions defined by the centre of the Earth and two points were we conduct spaced measurement, then after time Δt measurement system No. 2 takes the same directions in space as system No. 1 before. From this it follows that similarity of histogram shapes is in some way connected

with the same space directions. This conclusion also agrees with experimental results presented in [12–13].

In speaking of preferential directions we implicitly supposed that the measurement system is directional and because of this can resolve these directions. Such a supposition is quite reasonable for the case of daily period splitting, but for splitting of the local-time peak observed on the 1m scale it becomes very problematic because an angle, which must be resolved by the measurement system, is negligible. It is most likely that in this case we are dealing with space-time structure, which are in some way connected with preferential directions towards the Sun and the coelosphere. Second-order splitting of local-time peaks can also be considered as an argument confirming this supposition. Apparently we can speak of a sharp anisotropy of near-earth space-time. Existence of a local-time effect leads us to conclude that this anisotropy is axially symmetric.

The Authors are grateful to Dr. Hartmut Muller, V. P. Tikhonov and M. N. Kondrashova for valuable discussions and financial support. Special thanks go to our colleagues O. A. Mornev, R. V. Polozov, T. A. Zenchenko, K. I. Zenchenko and D. P. Kharakoz.

References

- Shnoll S.E., Kolombet V.A., Pozharskii E.V., Zenchenko T.A., Zvereva I.M. and Konradov A.A. Realization of discrete states during fluctuations in macroscopic processes. *Physics-Uspekhi*, 1998, v. 41(10), 1025–1035.
- Shnoll S.E., Zenchenko T.A., Zenchenko K.I., Pozharskii E.V., Kolombet V.A. and Konradov A.A. Regular variation of the fine structure of statistical distributions as a consequence of cosmophysical agents. *Physics-Uspekhi*, v. 43(2), 205–209.

3. Shnoll S.E. Periodical changes in the fine structure of statistic distributions in stochastic processes as a result of arithmetic and cosmophysical reasons. *Time, Chaos, and Math. Problems*, No. 3, University Publ. House, Moscow, 2004, 121–154.
 4. Shnoll S.E. Changes in the fine structure of stochastic distributions as consequence of space-time fluctuations. *Progress in Physics*, 2006, v. 6, 39–45.
 5. Panchelyuga V.A. and Shnoll S.E. Experimental investigations of gravitational-wave influence on the form of distribution function of alpha-decay rate. Abstracts of VI International Crimean Conference “Cosmos and Biosphere”, Partenit, Crimea, Ukraine, September 26 – October 1, 2005, 50–51.
 6. Panchelyuga V.A. and Shnoll S.E. Experimental investigation of spinning massive body influence on fine structure of distribution functions of alpha-decay rate fluctuations. In: *Space-Time Structure*, Moscow, TETRU, 2006, 328–343.
 7. Panchelyuga V.A., Kolombet V.A., Kaminsky A.V., Panchelyuga M.S. and Shnoll S.E. The local time effect observed in noise processes. *Bull. of Kaluga University*, 2006, No. 2, 3–8.
 8. Panchelyuga V.A., Kolombet V.A., Panchelyuga M.S. and Shnoll S.E. Local-time effect on small space-time scale. In: *Space-Time Structure*, Moscow, TETRU, 2006, 344–350.
 9. Shnoll S.E. Discrete distribution patterns: arithmetic and cosmophysical origins of their macroscopic fluctuations. *Biophysics*, 2001, v. 46(5), 733–741.
 10. Shnoll S.E., Zenchenko K.I. and Udaltsova N.V. Cosmophysical Effects in the structure of daily and yearly periods of changes in the shape of histograms constructed from the measurements of ^{239}Pu alpha-activity. *Biophysics*, 2004, v. 49, Suppl. 1, 155.
 11. Shnoll S.E., Zenchenko K.I. and Udaltsova N.V. Cosmophysical effects in structure of the daily and yearly periods of change in the shape of the histograms constructed by results of measurements of alpha-activity Pu-239. arXiv: physics/0504092.
 12. Shnoll S.E., Zenchenko K.I., Berulis I.I., Udaltsova N.V. and Rubinstein I.A. Fine structure of histograms of alpha-activity measurements depends on direction of alpha particles flow and the Earth rotation: experiments with collimators. arXiv: physics/0412007.
 13. Shnoll S.E., Rubinshtejn I.A., Zenchenko K.I., Shlektarev V.A., Kaminsky A.V., Konradov A.A. and Udaltsova N.V. Experiments with rotating collimators cutting out pencil of alpha-particles at radioactive decay of ^{239}Pu evidence sharp anisotropy of space. *Progress in Physics*, 2005, v. 1, 81–84; arxiv: physics/0501004.
-

SPECIAL REPORT**A High Temperature Liquid Plasma Model of the Sun***

Pierre-Marie Robitaille

Dept. of Radiology, The Ohio State University, 130 Means Hall, 1654 Upham Drive, Columbus, Ohio 43210, USA

E-mail: robitaille.1@osu.edu

In this work, a liquid model of the Sun is presented wherein the entire solar mass is viewed as a high density/high energy plasma. This model challenges our current understanding of the densities associated with the internal layers of the Sun, advocating a relatively constant density, almost independent of radial position. The incompressible nature of liquids is advanced to prevent solar collapse from gravitational forces. The liquid plasma model of the Sun is a non-equilibrium approach, where nuclear reactions occur throughout the solar mass. The primary means of addressing internal heat transfer are convection and conduction. As a result of the convective processes on the solar surface, the liquid model brings into question the established temperature of the solar photosphere by highlighting a violation of Kirchhoff's law of thermal emission. Along these lines, the model also emphasizes that radiative emission is a surface phenomenon. Evidence that the Sun is a high density/high energy plasma is based on our knowledge of Planckian thermal emission and condensed matter, including the existence of pressure ionization and liquid metallic hydrogen at high temperatures and pressures. Prior to introducing the liquid plasma model, the historic and scientific justifications for the gaseous model of the Sun are reviewed and the gaseous equations of state are also discussed.

1 Introduction**1.1 Historical perspective**

The modern theory of the Sun [1–5] can be traced back to 1870 when Lane published his discussion of the gaseous nature of this sphere [6]. At the time, of course, one could have had little idea about whether or not the Sun was really a gas. Nonetheless, Eddington [7, 8] would build on these early ideas. He believed that the laws of physics and thermodynamics could be used to deduce the internal structure of the Sun without any experimental verification [7, 8]. In 1926, he would speak hypothetically about being able to live on an isolated planet completely surrounded by clouds. Under these conditions, he still thought he could analyze the Sun without any further knowledge than its mass, its size, and the laws of physics [7, 8]. It was in this spirit that Eddington set out to expand on Lane's model of the Sun.

Eddington, more than any other person, has shaped our current understanding of the Sun. Consequently, it is fitting that a review of the current model be centered on his contributions. Some may argue that we have moved well beyond Eddington in our reasoning. However, Eddington has set a scientific course for the study of the Sun which has remained

essentially unchallenged for nearly eighty years. Every new finding has been rationalized within the context of the gaseous model and no alternative starting point exists. Yet, the gaseous model is characterized by inconsistencies and physical interpretations which cannot be easily explained based on laboratory findings.

As such, the hot liquid plasma model is presented herein. The new model provides a scientific alternative in solar analysis. It is based on a reevaluation of the internal processes and structures associated with the gaseous model. The liquid model advocates a much higher photospheric density and temperature, thereby directly invoking the physics associated with high energy/high density plasmas. In addition, it completely eliminates Eddington's radiative zone and brings into question the existence of the current very high density (150 g/cm^3) core.

1.2 Eddington's polytrope and solar collapse

Eddington began his analysis of the Sun by assuming that Lane's gaseous model was correct [6]. The Sun was treated as a simple polytrope [3], wherein a direct relationship existed between pressure, P , and density, ρ [9]. Eddington's polytrope was of the form $\rho = K_1 P^{1/\gamma}$, where K_1 is a constant and the polytrope exponent, γ , was set to $\frac{4}{3}$. Under these conditions, the central density of the Sun was ~ 54 times the average density and the central pressure was $1.24 \times 10^7 \text{ dyn/cm}^2$ [3]. By having recourse to the ideal gas law and fully radiative heat transfer, Eddington deduced a central core temperature of 1.2×10^7 [3, 7, 8]. Today, this remains the range for

*This work was posted as arXiv: astro-ph/0410075, October 4, 2004. The discussion relative to the internal constitution of the stars in the introduction places a heavy emphasis on the writings of A. S. Eddington. The author wishes to also highlight the work of Nikolai Kozyrev on "Sources of Stellar Energy and the Theory of Internal Constitution of Stars" translated from the original Russian dissertation in Progress in Physics 2005, v. 3, 61–99. Kozyrev's excellent work provides additional important contributions and insight relative to the gaseous models of the stars.

the internal temperature of the Sun $\sim 1.5 \times 10^7$ K (e.g., [2–5]).

At the same time, Eddington realized that a gaseous Sun should collapse on itself [7, 8]. Specifically, the great forces of gravity should compress the mass into a much smaller sphere. Like his predecessors, Eddington pondered on why the gaseous Sun did not collapse. He solved the problem by invoking outward radiation pressure originating from the central core. Reasoning that the inside of the Sun was generating light, Eddington thought that these photons could produce the outward pressure sought. Since light quanta clearly possessed momentum, this “light pressure” kept the gaseous Sun from collapsing [7, 8]. Consequently, Eddington postulated that the inner portion of the Sun produced photons. He then deduced that these individual light quanta would sooner or later collide with a gas ion or atom and propel it against the forces of the Sun’s gravity. The region of the Sun where this occurs was called the radiative zone. It remains a central portion of solar theory to this day. Importantly, however, this zone exists primarily as a result of Eddington’s reasoning. For stars on the order of the solar mass, it is currently held that internal radiation pressure is not as significant as Eddington had advanced. A radiative zone is still present, but the effects of radiation pressure are downplayed. Rather, modern theory holds that the Sun is prevented from collapse due to electron gas pressure [3]. The radiation zone is still present in the Sun, but radiation pressure becomes dominating only for heavy stars on the order of 10 solar masses [3].

The modern theory of the Sun also makes use of a significant convective zone, which extends throughout the outer envelope. Convective zones extend to deeper levels as stellar masses decrease, such that small stars can be viewed as fully convective. Conversely, for stars with masses larger than the Sun, it is the core of the star which is convective [3]. The extent of the convective zone then grows towards the envelope of the star, as mass increases. Eventually, the convective zone extends to 70% of the stellar radius in stars on the order of 50 solar masses. In this case, the envelope is radiative in nature. Supermassive stars, like the smallest stars, finally become fully convective [3].

1.3 Photon shifts and opacity considerations

While Eddington believed that he properly understood a key aspect of solar structure with the creation of the radiative zone, he also wanted to know exactly how many photons the Sun could produce to support this hypothesis. Not sufficiently considering Kirchhoff’s work [10], Eddington incorrectly believed that Stefan’s law was universal [11]. He then applied this law to estimating the amount of photons produced. Given the dimensions involved, and the temperatures hypothesized for the solar interior, this photon output would have been tremendous. Eddington also recognized that a blackbody at millions of degrees should produce its photons at

X-ray frequencies [12].

Thus, Eddington had deduced that the internal portion of the Sun was at 1.2×10^7 K. This resulted in the generation of photons at X-ray frequencies. At the same time, Langley had previously measured the solar spectrum and was setting the temperature of the photosphere at $\sim 6,000$ K. In order to resolve this dilemma, Eddington simply stated that when photons are emitted, they are initially produced at X-ray frequencies [7, 8]. However, as these photons are scattered or absorbed in the collisions associated with radiation pressure, they slowly lose some of their energy. In this manner, after millions of years and many collisions, the photons emerge from the Sun’s photosphere shifted to the visible region. Only a very small fraction of the total photons in the radiative zone manage to escape at any time. According to Eddington, the radiative zone is acting as a very slowly-leaking “sieve” [7, 8]. The photons traveling through this zone were thought to experience free-free, bound-free, and bound-bound absorptions along with scattering [2, 3]. The entire process would result in producing a certain opacity in the solar interior.

Eddington’s model requires that these processes (scattering and free-free, bound-free, and bound-bound transitions) result in a final opacity which becomes Planckian in appearance. This was needed in order to permit the proper absorption and reemission of all photons, at all frequencies, and at all levels of the solar interior. In fact, the “opacity problem” constitutes one of the great weaknesses in a model of an interiorly radiating object. The issue is so complex that Rosseland mean opacities [2, 3], which are frequency independent, are often utilized. Such a procedure completely sidesteps the central issue. It is always possible to build an absorption or opacity profile given enough elements and weighted physical mechanisms (scattering and free-free, bound-free, and bound-bound transitions). However, the requirement that these profiles continually and systematically change throughout the interior of the Sun, while remaining blackbody in nature and yielding the proper frequency dependence, does not appeal either to simplicity or objective reality. In fact, the generation of a Planckian spectrum requires a Planckian process [10]. Such a spectrum can never be generated from the sum of many non-Planckian processes. Once again, the current gaseous model has serious shortcomings in the manner in which solar thermal emission is explained.

Unfortunately, for Langley and Eddington, the situation is even more complex than they initially believed [10]. The Sun is not in thermal equilibrium with an enclosure. In reality, enormous convection currents are present both on the solar surface and within the solar interior. These convection currents can easily act to violate the integrity of Eddington’s layers. Therefore, the interior of the Sun represents a significant deviation of the requirements set forth in Kirchhoff’s law (equilibrium with a perfectly absorbing enclosure [10]).

The application of the laws of thermal emission [11–13] to the Sun constitutes a violation of thermodynamic principles.

1.4 Coronal heating

Beyond Eddington, the next big step in solar theory came in the 1950's when scientists were beginning to obtain interesting data from the solar corona. It was observed that the corona possessed, within it, highly ionized ions produced at temperatures well in excess of 1.0×10^6 K [14]. The width of Lyman- α lines further demonstrates that temperatures in the corona ranged from 2.6×10^6 to 1.2×10^6 K at 1.5 and 4 solar radii, respectively [14]. These findings of very hot temperatures in the corona presented a problem for solar theory. A temperature within the corona ($>1.0 \times 10^6$ K) which exceeded that of the photosphere ($\sim 6,000$ K) indicated a violation of the 2nd law of thermodynamics. That is, heat could not be coming from inside the Sun to heat the corona, while remaining incapable of heating the photosphere. Thus, if the photosphere was really at $\sim 6,000$ K, there must be found an alternative means to heat the corona. It has now been widely accepted that the local heating in the corona occurs as a result of a process involving the flow of ions through the magnetic fields of the Sun [5].

1.5 Helioseismology

Currently, much of the support for the gaseous models of the Sun arises from helioseismology [15] or the study of solar quakes on the surface of the Sun. It is claimed that excellent agreement exists between the theoretical models and the actual seismological data. In large part, this is a direct measure of the gaseous model's ability to permit variations in density, pressure, temperature, composition, depth and opacity values throughout the solar interior. Given enough variables, good agreement with experimental data can be achieved. Nonetheless, it is interesting that despite phenomenal agreement between theory and experiment, the theoretical fits completely break down in the outer 5% of the solar disk [16]. This is not surprising since the solar photosphere currently has a hypothetical density which is lower than that present within the best vacuums achieved on earth. Since acoustic waves cannot propagate in a vacuum, it is not surprising that the theorists are unable to fit the exterior the Sun [16]. Yet, this is precisely that region of the Sun from which all the data is being collected.

1.6 Summary of the gaseous models

Eddington was concerned with the great problems of solar theory: (1) how to prevent the gaseous Sun from collapsing on itself, (2) how to set the internal temperature, and finally, (3) how to shift the frequency of photons produced at X-ray frequencies to the observed visible region. He solved these problems by invoking radiation pressure and the laws of thermal radiation. The creation of the radiative zone resulted

in tremendous radiation pressure within the Sun. For Eddington, this radiation pressure exactly balanced with the gravitational forces and resulted in one of the earliest gaseous models of the Sun. The gaseous Sun had been prevented from collapsing and photons were produced appropriately in the visible range. The interior of Eddington's gaseous Sun was at very high temperatures estimated at millions of degrees. Yet, this extremely hot object was surrounded by a very cool photosphere, only $\sim 1,000$ kilometers thick and at a temperature of just $\sim 6,000$ K.

Regrettably, the idea that photons become the primary means of striving for internal thermal equilibrium in a star is not in accordance with our knowledge of the thermal behavior of objects [17, 18]. Rather, for all other objects, internal thermal equilibrium is achieved through thermal convection and conduction [17, 18]. In contrast, radiative heat transfer enables an object to dissipate heat and reach thermal equilibrium with the outside world (e.g., [17–20]). Astrophysical treatments of thermal radiation [21–23] minimize these arguments and, like all other textbooks, fail to state the underlying cause of the radiation [10].

Under the gaseous model, the internal temperature of the stars continues to rise, despite the fact that photons are being emitted. Stellar compression becomes an uncontrollable process. In order to cool the stars, photons must be injected into their interior. Eddington best summarizes this violation of thermodynamics and the dilemma it creates for all gaseous models [2]: "I do not see how a star which has once got into this compressed condition is ever going to get out of it. So far as we know, the close packing of matter is only possible so long as the temperature is great enough to ionize the material. When a star cools down and regains the normal density ordinarily associated with solids, it must expand and do work against gravity... Imagine a body continually losing heat but with insufficient energy to grow cold!"

Note that the second sentence in this quote is the essence of the problem. Eddington has ignored the consequences of van der Waals' equation and the incompressibility of the liquid state. He constructs a model wherein the known behavior of the condensed states of matter on Earth is discarded. The gaseous model requires production of photons at high frequency (X-ray, gamma) within the core of the Sun, which are then shifted to the visible region [7, 8]. However, the shifting of a blackbody radiation spectrum produced at one Wien's displacement temperature to another is without experimental verification. The current complexity associated with the calculations of stellar opacities hint at the unreasonableness of such conjectures. A Planckian process is required to generate a Planckian spectrum [10]. However, the gaseous stellar models are incapable of yielding a Planckian process, since they "a priori" exclude the existence of condensed matter and of a photospheric lattice.

Since modern stellar theory remains based on gaseous models, the analytical equations of state [24, 25] are founded

on the assumption that the Sun can be treated as a compressible gas. The emergence of numerical solutions [24, 25], including such refinements as the addition of partial ionization and Debye-Hückel theory, alters nothing of the underlying framework. Currently, the density of the central core is thought to be $\sim 150 \text{ g/cm}^3$, while that of the lower photosphere is on the order of 10^{-7} g/cm^3 [26]. Neither of the numbers, of course, can be verified by direct experimentation. The modern Sun and all of the main sequence stars remain viewed as compressible gases without lattice structure. Only the details of the local densities, temperatures, composition, opacities, radiative emission, and convection currents, are altered. For stars near the solar mass, it is advanced that electron gas pressure now acts to prevent solar collapse [2, 3]. This is true even though the mathematical analysis of electron gas pressure relies on the use of real or imaginary rigid surfaces [2] which can never exist within the stars. The stars are quite unlike the Earth's atmosphere, since the latter is resting on a distinct surface. As a result, electron gas pressure is unlikely to prevent solar collapse since the gaseous models cannot invoke rigid surfaces while maintaining the integrity of the gaseous state. Irrespective of such arguments, one cannot discount that Eddington's radiative pressure remains extremely important for the gaseous theories, especially in the more massive stars.

2 Liquids and gases

The flow of material on the surface of the Sun (e.g., [2, 3, 5, 27]) makes both the gaseous and liquid states prime candidates for discussing the nature of the photosphere. Unfortunately, the distinction between the gaseous and liquid state is often difficult to establish. Gases and liquids are often viewed simply as fluids with no further distinction, but differences do exist. Liquids are characterized by their relatively high densities and by their surface tensions [28–31]. They also have real internal structure and can be seen as possessing “fleeting lattices” with short range order [28–31]. Gases, on the other hand, fail to display a surface and have no internal structure. Liquids can boil and thereby produce the gaseous state. Gases cannot boil. Liquids, unlike gases, are essentially incompressible [28–31]. In conjunction with solids, liquids correspond to the densest form of matter detected in the laboratory. In this regard, a significant increase in the density of the liquid state would require changes within the atomic nucleus itself, as the atomic number is increased. Large changes in pressure, by themselves, are incapable of significantly altering, by orders of magnitude, the density of the liquid state [28–32]. This is quite unlike the behavior of highly compressible gases, as reflected in the ideal gas law [28, 32].

Although their exact thermal behavior remains extremely poorly documented [20], liquids can also emit continuous radiation by virtue of their continuous physical nature. Most-

ly liquid metals have been studied [20], and little is known about the thermal properties of nonmetallic liquids. Studies with water at microwave frequencies only add to the complexity of the problem. For instance, it is easy to establish that the oceans are not blackbody in nature. At the Nadir angle (view is normal to the water surface), the sea surface appears with a brightness temperature of less than 100 K at 1.4 GHz [33]. In addition, the brightness temperature of salt water can be relatively independent of actual temperature [33]. When larger observation angles are used, the brightness temperature of sea water rapidly rises [33], although it is always short of the correct value. Since the brightness temperature of salt water is so highly dependent on salinity, it is clear that an understanding of thermal emission processes in liquids is complex [33].

Liquids unlike gases, can support transverse wave propagation as reflected by the presence of weak phonons. The behavior of phonons has been examined in liquid helium [34]. Phonons have also been studied in superionic conductors which are characterized by liquid-like mobility of one of the ionic species [35]. The study of phonons in solids and liquids usually involves neutron scattering experiments (e.g., [34–38]). As for gases, they are unable to support transverse phonons. Neutron scattering experiments, aimed at determining structure in solids and liquids, do not exist as related to gases. Acoustic experiments with gases involve the study of longitudinal waves.

Differences clearly exist between the liquid and gaseous states [28–32]. As such, these two phases are not simply a continuum of one another, as is often assumed. Unlike the ideal gas law, the equations used in the analysis of liquids tend to be complex. Herein lies a major difficulty in advancing a liquid model of the Sun. Nonetheless, in order to discern the relative merits of a gaseous versus a liquid model, solar observations themselves, not mathematical simplicity, must guide the theorist. Thus, solar behavior must be re-examined and the most critical data remains the nature of the solar spectrum.

3 Thermal emission

3.1 Local thermal equilibrium

Modern solar models make extensive use of local thermal equilibrium in order to simplify the analysis of stellar structure [1–3]. Nonetheless, plasmas are well-known to support electronic and ionic temperatures which are not at equilibrium. Recent work [10] highlights that the Sun cannot meet the requirements for a blackbody, as set down by Kirchhoff, for the simple reason that it is not in thermal equilibrium with a perfectly absorbing enclosure [9, 19]. The analysis of the Sun is a non equilibrium problem, as manifested by the presence of convection currents, solar eruptions, solar wind, and emission of light without confinement. All transport processes, including convection, are non equilibrium pro-

cesses [29]. Planck has previously warned that the presence of convection currents is sufficient to completely destroy local thermal equilibrium arguments [39]. That local thermal equilibrium does not exist is of profound consequence to any theorist, since simplifying assumptions are removed. Despite this complication, the lack of local thermal equilibrium for the interior of the Sun is consistent with observations of non-equilibrium in the solar corona, where significantly different electronic and ionic temperatures have been detected [40]. Nonequilibrium within the corona may well be a manifestation of the state of the entire star. The photosphere is clearly not in thermal equilibrium with an enclosure (e.g., [9, 19]). Furthermore, it possesses convection currents rendering it unsuitable as a candidate in blackbody radiation [10, 39].

As such, it was improper for Langley [41, 42] to set a temperature of the photosphere at $\sim 6,000$ K, simply because a thermal emission spectrum was present. The proper assignment of a temperature based on thermal arguments depends on the known presence of a perfectly absorbing enclosure, namely a solid graphite box [10]. Langley's use of Planckian arguments [11–13, 39, 41, 42] to set a temperature for the photosphere constitutes a violation of Kirchhoff's law of thermal emission [10, 43, 44]. The presence of local thermal equilibrium is central to the assignment of any temperature based on thermodynamic arguments [10, 39].

Eddington's need to shift the solar spectrum to lower frequencies requires that gaseous atom or ionic hydrogen or helium be able to both absorb and re-emit a blackbody spectrum. This creates essentially impossible constraints on the opacities needed inside the Sun, especially given that only scattering and free-free, bound-free, and bound-bound transitions can be considered. None of these processes are individually capable of providing the proper Planckian behavior. Only complex summations, involving many discontinuous phenomena, can lead to the required continuous opacities. The problem is so complicated that the entire task is often sidestepped. Rosseland mean opacities, which are frequency independent, are often used to deal with this issue [2, 3]. However, the use of Rosseland mean opacities is unsatisfactory. The requirements set on opacity by Eddington for the radiative zone are contrary to our knowledge of thermal emission spectra in either gases or plasmas (e.g., [45, 46]). As mentioned above, the production of a Planckian spectrum must involve a Planckian process and not the summation of many non-Planckian spectra. The "opacity problem" represents the greatest single warning sign that a gaseous model of the stars cannot be correct.

3.2 Thermal emission in liquids

Like solids, liquids possess a lattice, although this structure is often fleeting (e.g., [29–31]). This is manifested in the presence of Brownian motion within the liquid. Thus, in a liquid, not all of the energy is contained within the vibration-

al degrees of freedom of the lattice. This directly accounts for the inability to obtain a complete monitoring of the energy distribution within a liquid based only on its thermal emission. Indeed, most of the nonnuclear energy in a liquid may well be contained in the translational and rotational degrees of freedom. The ability of a liquid to store energy in translational degrees of freedom certainly leaves less energy than expected at a given temperature in the vibrational degrees of freedom. This is a problem for a Planckian oscillator model which does not consider translational and rotational energy [13]. As a result, it is hypothesized that the presence of translational and rotation degrees of freedom can cause a liquid to report a much lower temperature than its real temperature, when the laws of thermal emission [11–13] are utilized to monitor its emission spectrum. As mentioned above, the idea that radiation pressure is present within the Sun is not in accordance with the known mechanisms of heat transfer within objects [17]. There is no experimental basis on Earth for invoking that an object can strive for internal thermal equilibrium using thermal radiation. Conduction and convection dominate heat transfer within objects [17]. A liquid model is more apt to deal with heat transfer through these two mechanisms, since it provides increased density, facilitating both more efficient conduction and convection.

4 The liquid model of the Sun

A central tenant of the liquid plasma model is that the density within the solar interior is nearly constant. It has been well established that liquids are essentially incompressible and that their compressibility decreases quite dramatically as pressure is increased [28–31]. Therefore, in the liquid plasma model, the liquid framework is regarded as incompressible and the issue of solar collapse never arises.

There are numerous arguments supporting a liquid plasma model. These include: (1) the continuous nature of the emission spectrum, (2) the average density of the solar mass, (3) the gentle oblateness of the solar sphere, (4) the presence of a distinct solar surface, (5) the presence of surface gravity waves and helioseismology studies, (6) the known existence of hydrogen on Earth in the liquid metallic plasma state at high pressures and temperatures, (7) the existence of solar boiling, and (8) the presence of the corona, transition zone, and chromosphere. In addition, the liquid plasma model provides for the mixing of solar materials, resulting in important evolutionary consequences for the stars. At the same time, the liquid plasma model addresses the issue of coronal heating and helps to resolve the thermodynamic problems in this area.

4.1 Solar emission

The solar spectrum deviates from a blackbody in appearance in that the high frequency region is distorted. This finding

urges caution in setting a temperature to the photosphere using Planckian arguments. Based on experimental work in thermal emission, the photosphere cannot be a low density gas or plasma. Gases and plasmas, outside the confines of an enclosure, simply cannot produce a Planckian-shaped thermal emission profile as seen in the visible light of the photosphere. These issues have previously been discussed in detail [10]. The production of a continuous blackbody spectrum is incongruent with an origin from a low density source. Experimental blackbodies are exclusively solids (e.g., [47–51]).

The concept that the photosphere, as an “opaque gas”, is able to emit as a blackbody is not supportable. Without exception, the approach to opaque behavior by gases or plasmas is accompanied by an increase in density and pressure. In contrast, the density advanced for the photosphere is on the order of 10^{-7} g/cm^3 [26]. No gas has been demonstrated to approach optically opaque behavior at such densities. Thus, while it is believed that, in the limit of high pressures, some gases can become opaque, it is more likely that they simply become liquids. The idea, that free gases or plasmas can become optically opaque [45, 46] and can follow Kirchhoff’s law, ignores the known observation that such behavior cannot be produced outside the confines of a solid enclosure [10]. Studies in which gases or plasmas approach optically opaque behavior are always confined to enclosures at high pressure. For instance, note that the Tokamak reactors used in plasma physics are often lined with graphite [52]. This situation is exactly analogous to the experimental conditions under which Kirchhoff’s law was developed [10]. Real blackbodies always involve enclosures which are either made from graphite [49, 50] or lined with soot (graphite) containing paints [47, 48, 51]. As a result, it is not surprising that, in the limit of high pressure within the confines of a Tokamak, the approach to blackbody behavior can be reached [10, 45, 52]. In any case, such a setting is completely unlike the surface of the Sun, wherein a solid enclosure is not present.

Unfortunately, it appears that the exact physical mechanism for producing a blackbody radiation spectrum has not been defined by the scientific community [10]. Nonetheless, thermal radiation must be linked to one of the simplest processes within matter, namely atomic or nuclear vibrations within the confines of a lattice structure [10]. This is reminiscent of Planck and his oscillators [13, 39]. In the final analysis, whatever physical mechanism is invoked for blackbody radiation, it should be independent of nuclear reactions, since all solids are able to emit some form of continuous thermal radiation [20].

If it is true that the frequency and amount of photons released by an object is related only to the amount of energy in the vibrational degrees of freedom of the lattice [10], it is easy to see why Langley believed that the photosphere was at a temperature of only $\sim 6,000 \text{ K}$. Note the well established convection currents on the surface of the Sun (e.g., [4, 5, 27]).

These currents contain translational energy which is not readily available for thermal emission. However, during flares and other eruptions, it is well-known that X-rays can be released from the solar surface. These X-rays reveal brightness temperatures of millions of degrees (e.g., [4, 5, 27]). In this case, the translational energy of the liquid envelope is being converted to thermal photons in a manner revealing a stored energy bath with temperatures well in excess of 6,000 K. Such X-ray findings from the solar surface were not at the disposal of Langley when he set the photospheric temperature in the mid-1800’s [41, 42].

It is therefore hypothesized that a liquid can instantaneously lower the total output of photons, at a given temperature, and release them at a frequency significantly lower than what would be predicted from their real energy content and temperature. This is simply an energy partition problem which arises in the presence of convection currents. The sea surface temperature at microwave frequencies discussed above hints to this behavior.

A liquid photosphere with a temperature of $\sim 7.0 \times 10^6 \text{ K}$ could be generating photons not at X-ray frequencies, as expected, but rather in the visible range. This occurs because the photosphere has convection. Since most of the energy of the photosphere is tied up in the translational (or rotational) degrees of freedom and its associated convection, it is simply not available for the generation of thermal photons. However, this energy can become available during a solar eruption which reveals that the real temperatures of the solar photosphere are well in excess of 6,000 K. The liquid phase provides a means of producing a thermal radiation curve for the Sun at a lower apparent temperature than its real temperature. All that is required is to lower the force constant in Planck’s oscillators. In this regard, note that an oscillator representing a van der Waals interaction would have a much weaker force constant than one representing covalent bonds.

This hypothesis remedies the problem with Langley’s temperature for the photosphere. Setting a real temperature of the photosphere at $\sim 7.0 \times 10^6 \text{ K}$ permits the free flow of heat throughout the outer layers of the Sun. The 2nd law of thermodynamics is no longer violated. Photons do not take millions of years to leave the Sun [7, 8]. Rather, they are solely produced and released at the photosphere using a mechanism common to all condensed objects on Earth. The radiative zone is eliminated and the need to shift high energy photons removed.

4.2 Solar densities

The Sun has an average density ($\sim 1.4 \text{ g/cm}^3$) which can easily support the liquid plasma model. Indeed, the gaseous model applies extremes of density which are not easily justified (150 g/cm^3 for the core and 10^{-7} g/cm^3 for the photosphere [26]). Instead, the liquid plasma model simply requires a very ordinary density throughout the body of the Sun.

The presence of a liquid structure eliminates the need for radiation pressure to prevent the Sun from collapsing on itself. The liquid alone can support the upper layers. For the gaseous models, solar collapse is prevented by having recourse to internal radiation and electron gas pressure both of which are without sound experimental justification. In a liquid model, the problem of solar collapse is simply addressed by invoking the incompressibility of liquids. Interestingly, the Jovian planets all have densities consistent with the liquid state (Jupiter: $\sim 1.33 \text{ g/cm}^3$; Saturn: 0.7 g/cm^3 , Uranus: 1.30 g/cm^3 , and Neptune 1.76 g/cm^3). For a gaseous model of the Sun, it would have been convenient if at least one of these planets had an average density consistent with the sparse gaseous states (e.g., 10^{-4} – 10^{-7} g/cm^3) currently proposed for the convective zone and the photosphere (10^{-7} g/cm^3) [26]. Note that the latter density approaches the value of a reasonably good vacuum in the laboratory. The Jovian planets have high average densities (0.7 – 1.76 g/cm^3) despite their small size and masses relative to the Sun. As such, the sparse densities currently assigned to the outer layers of the Sun are incongruent with the high average densities of the Jovian planets, especially given that these are also constituted primarily of hydrogen and helium. This leads us to deduce that the Jovian planets are also condensed in nature and that they may have significant liquid components, both on their surface or in their interior.

The densities of materials on Earth is determined primarily by the atomic number and by the packing of the crystal lattice. As far as the existence of a solar core is concerned, there is no experimental evidence for reaching densities of $\sim 150 \text{ g/cm}^3$ using a hydrogen and helium framework. Without exception, high densities involve high atomic numbers. Mathematical arguments to the contrary are based exclusively on the collapse of a gaseous model of the Sun and are without experimental justification in the laboratory. Once again, the Jovian planets do not support the idea of a dense core given that they, like the Sun, possess average densities on the order of 1 g/cm^3 . Unlike the gaseous model, which must have a dense core to compensate for its sparse convective zone and photosphere, the liquid model does not necessitate the presence of a dense core. Such a core may or may not be present. However, laboratory observations, with the densities achievable using helium and hydrogen, suggest that it cannot exist.

4.3 The solar surface

The Sun has a reasonably distinct surface. This point has recently been emphasized by images obtained with the Swedish Solar Telescope [53, 54]. These images reveal that the solar surface is not simply composed of clouds hovering about, but has a clear three-dimensional appearance which evolves in a manner reflecting “solar hills, valleys, and canyons” [53, 54]. Solar granulations appear to be “puffy hills

billowing upwards” [53, 54]. This represents strong evidence that the solar surface is dense and has surface tension, a clear property of the liquid state.

Gases are not characterized as possessing surfaces. This accounts for the extension of the corona (which is a gaseous plasma) for millions of miles beyond the Sun without a distinct boundary. The hot liquid plasma model of the Sun helps to explain the distinct nature of the solar surface, wherein a transition is observed between the photospheric density and that of the solar atmosphere. The chromosphere is reminiscent of the critical opalescence of a gas in the vicinity of criticality [30], and the existence of such a zone is highly supportive of a liquid model. Furthermore, the surface nature of the Sun is well visualized using imaging methods, including Doppler techniques [40, 53–55]. The surface tension of a liquid provides an elegant explanation for the distinct nature of the solar surface, which is not easily available within the context of a gaseous model.

4.4 The solar oblateness

Solar oblateness, ε is a dimensionless quantity

$$\varepsilon = (R_E - R_P)/R_E$$

obtained by comparing the values of the equatorial (R_E) and the polar radii (R_P). The existence of gentle solar oblateness has been recognized for nearly thirty years. Initial values measured by Dicke and Goldberg [56] were as large as $4.51 \pm 0.34 \times 10^{-5}$. More modern values are slightly less pronounced at 8.77×10^{-6} [57]. While such oblateness appears extremely small and negligible at first glance, it provides a dilemma for the gaseous models.

In order to properly analyze solar oblateness, it is necessary to have recourse to models of rigid body rotation [57]. In this regard, the theory of rotating liquid masses is well developed and extensive discussions can be found in Littleton’s classic text [58]. In addressing the oblateness of the Sun [56, 57], the density of this rotating sphere is maintained as essentially constant throughout the solar radius [57]. The model used is described by an analytical form and is able to account both for the rotation of the convective zone and for the differential rotation of the inner Sun [57]. Importantly, the rigid body model [57, 58] is not dependent on the solar density. This is in sharp contrast with the well-known equations of state for stellar structure [2, 3, 24, 25]. The latter, of course, possess a strong interdependence of density and pressure with radial distance.

Beyond the Sun, other stars also possess varying degrees of oblateness. The most significant of these, at present, appears to be the southern star Achernar, a hot B-type star with a mass currently estimated at six times the mass of the Sun. The oblateness of this star is caused by rapid rotation and is a stunning 1.56 ± 0.05 [59]. Achernar’s oblateness is so severe that it is completely incompatible with the Roche model,

wherein the mass of a star is concentrated near the stellar interior [3, 59]. The oblateness of the Sun and some stars provides significant support for the liquid plasma model of the Sun and a tremendous hurdle for the gaseous models.

4.5 Surface gravity waves and helioseismology

A liquid plasma model of the Sun is also best suited to the study of helioseismology (e.g., [15]). This is because terrestrial observations of this nature are exclusively limited to the oceans and continents, materials with high densities. It would be incongruent to advance such studies for the terrestrial atmosphere. Yet, the density of the terrestrial atmosphere at sea level is $\sim 1,000$ times greater than the density proposed by the gaseous models for the solar surface.

A solar seismic wave [55] was produced in association with a flare on the surface of the Sun on 9 July 1996 [40]. Such a Sun quake demonstrates that the solar surface is fully able to sustain a surface gravity (or transverse) wave extending over millions of meters. These are described as “resembling ripples from a pebble thrown on a pond” [40, 55]. The ability to sustain such a wave requires the presence of very dense materials. Indeed, sparse gases are completely unable to sustain surface gravity waves as these require the presence of condensed matter. Such Sun quakes provide powerful evidence that the solar surface is comprised of a material attaining a very high density. While a gaseous model can easily deal with longitudinal acoustic waves within the solar interior, the same cannot be said for its ability to deal with the presence of a surface gravity (or transverse) seismic wave on the surface. Once again, it is clear that the current theoretical fits fail at the solar surface [16].

The ability to conduct helioseismology studies on the Sun (e.g., [15, 40, 55]) is incongruent with a true gaseous nature. While sparse gases and plasmas are able to sustain longitudinal acoustic waves, they are unable to support transverse seismic waves. Terrestrial seismology is limited to the study of the oceans and the continents. The Earth’s atmosphere is much too thin to enable such studies. The liquid plasma model of the Sun is better suited to explain the presence of seismologic activity on the surface of the Sun.

4.6 Hydrogen as a liquid metal plasma

At atmospheric temperatures and pressures, hydrogen exists as a diatomic molecular gas. At low temperatures, condensed molecular hydrogen is an insulator with a relatively wide band gap ($Eg = 15$ eV). It is noteworthy that when hydrogen is shock-compressed, and thereby submitted to extreme pressures (>140 GPa) and temperatures (3000 K), it is able to undergo pressure ionization [60]. In so doing, hydrogen assumes a liquid metallic state, as revealed by its greatly increased conductivity [60]. Similar results hold for deuterium, although the insulator to metal transition occurs under less

intense conditions [61]. The existence of liquid metallic hydrogen plasmas is of tremendous importance in astrophysics and has direct consequences on the structures of Jupiter and Saturn [30, 60]. However, these findings have not been extended to the Sun, even though the Sun is able to subject hydrogen to higher temperatures and pressures.

In any case, dense liquid metallic plasmas of hydrogen provide very interesting possibilities in stellar structure which should be considered by the plasma physicist. That liquid metallic hydrogen is known to exist, directly implies that the Sun can be treated as a liquid metal plasma. The equations of magnetohydrodynamics [62] become relevant not only in the corona, but also within the entire Sun. This has tremendous consequences for stellar and plasma physics, further implying that the gaseous equations of state must be abandoned. A liquid metal plasma model of the Sun implies (1) high, nearly constant, densities, (2) a rigid body problem, and (3) the use of continuous equations of state and magnetohydrodynamics [45, 62, 63].

Liquid metallic hydrogen may also present interesting lattice characteristics to the theorist. Calculations reveal that metallic hydrogen displays an important dependence of potential energy and interatomic distance [63]. For instance, in liquid sodium, the potential well for interionic bonding has a single minimum. In contrast, for metallic hydrogen, the spatial inhomogeneity of the electron density is so important that higher order perturbations must be considered. This leads to potential functions with groups of minima rather than a single minimum [63]. These potential energy functions have important pressure dependences [63]. As a result, metallic hydrogen should be able to assume a variety of lattice structures, with varying interatomic distances, in a manner which depends primarily on temperature and pressure. It is likely that future extensions of these findings to liquid metallic hydrogen will enable the calculation of various possible structures within the liquid phase itself. This may be important in helping us understand the nature of Sunspots and stellar luminosities, particularly when magnetic field effects are added to the problem.

4.7 The displacement of solar mass

All current gaseous models of the Sun make the assumption that densities are gradually changing between the convection zone, photosphere, chromosphere, transition zone, and corona. In these models, only the opacity changes at the photosphere, in order to create the “illusion” of a surface. Nonetheless, it is clear that a phase transition is occurring between the photosphere and the chromosphere/transition zone/corona.

In the photosphere, both upward and downward radial flows are observed. These are also associated with transverse flows parallel to the surface itself. The motion of Sunspots also reminds us that transverse flows are an important com-

ponent of mass displacement in the photosphere. In sharp contrast, flows in the corona are clearly radial in nature (ignoring the effects of solar eruptions and flares). The solar wind is a manifestation of these radially pronounced flows. Consequently, the analysis of solar mass displacement, at the surface and in the corona, clearly reveals that we are dealing with an important phase transition at the photosphere. The solar corona is a gaseous plasma. Note that it has all the characteristics of a true sparse state (no surface, no continuous spectrum, not subject to seismological studies, unable to boil). It is proper to think of the corona as representing the vapor surrounding the condensed photosphere. This is typical of every liquid-gas equilibrium observed on Earth. The corona has no distinct boundary, reflecting once again that it is the true gaseous plasma, not the photosphere. As previously noted, the chromosphere is reminiscent of the critical opalescence at the gas/liquid interface near criticality [30]. This is an important observation which should not be dismissed.

4.8 The boiling action of the solar surface

Solar boiling is a well established occurrence. Indeed, it is commonplace to refer to the Sun as a “boiling gas”. Gases, however, cannot boil. They are the result of such action. The act of boiling is a property of the liquid state and is directly associated with the presence of a distinct surface. To speak of the Sun as “a boiling gas”, as is done in so many astrophysical texts, is an unintended contradiction relative to the current gaseous model of the Sun.

5 Advantages of the liquid plasma model

5.1 Solar mixing and nuclear reaction processes

The presence of a liquid state provides an opportunity for mixing of nuclear species within the solar sphere. The liquid state can maintain the nuclei involved in nuclear reactions in close proximity with constant mixing, thereby providing a significant advantage in achieving efficient nuclear burning. Conversely, within a solid core, the flow of reacting nuclei is greatly hindered. All solar models advocate that the bulk of the nuclear reactions in the Sun occur in the core. As the Sun evolves, it is said that the hydrogen core will slowly burn out [2, 3]. The Sun will then move to helium burning, and later to the burning of the heavier elements. In contrast, in the liquid plasma model, nuclear reactions are free to occur throughout the solar body, as a result of the nearly uniform solar density.

The energy produced in this fashion, within the solar interior, would be brought to the surface by conduction and convection. When nuclear reactions occur on the surface of the Sun, energy could be directly emitted in the form of gamma rays. That nuclear reactions can be distributed throughout the solar interior has dramatic implications for

the lifetime of our Sun, since the burning out of a nuclear core would not occur. A liquid model could extend the life of our star more than 10 fold, relative to the current expectancy. This is because only 10% of the hydrogen fuel is hypothesized to be burned, in the core of the present gaseous model, before the Sun is forced to switch to helium [3]. The liquid model elegantly overcomes such limitations, by enabling the continuous free flow of reactants in nuclear processes. As a result, the composition of the photosphere becomes an important indicator of the composition of the entire star, since convection now acts to equilibrate the entire solar interior. The determination of stellar compositions is subject only to the timescale of mixing. Such reevaluations have profound implications for stellar evolution and cosmology.

5.2 Coronal heating

The eruption of solar flares and prominences are associated with the displacement of material from the solar surface. Such events often occur in conjunction with the release of strong X-ray and gamma ray flashes. These flashes point to an underlying thermal potential in the photosphere which is not expressed under normal circumstances. This provides secondary evidence for the hot photospheric liquid plasma model. In this model, the heating of the corona, by complex magnetic field interactions is still permitted, but no longer required. The primary means of internal heat transfer within the Sun once again becomes convection and conduction [17]. Since energy transfer through convection is only proportional to T and not T^4 (as was the case for thermal radiation), it can be expected that regions of non-equilibrium superheated fluid exist within the Sun. A theory based on the release of superheated fluid from the interior could help explain much of the solar activity found on the surface, including flares and prominences.

In order to simultaneously preserve Langley’s temperature and respect the 2nd law of thermodynamics, the gaseous model provides two means of generating heat (e.g., [4, 5, 27]). The first of these occurs within the Sun and is thought to be thermonuclear in origin. The second occurs in the corona and is thought to be of magnetic origin. Particles moving at enormous speeds are also involved to ensure this second temperature. Furthermore, something strange must be happening relative to the photosphere. The gaseous model advances that this layer cannot be heated either by the interior of the Sun or by the corona, both of which are at much higher temperatures. This problem is overcome in the liquid plasma model by raising the true temperature of the photosphere itself, based on energy partition in liquids and on the known production of hard X-rays at the solar surface during eruptive events.

At the same time, the liquid model is quite easily extended to include the presence of Alfvén waves in the chromosphere, transition zone, and corona, much in the same way

as the current gaseous model (e.g., [4, 5, 27]). In this regard, the increased density of the photosphere in the liquid model may well help to better explain the origin and behavior of the magnetic field lines located at the surface of the Sun.

5.3 The evolution of the stars

It is clear that adopting a liquid plasma model of the Sun constitutes a significant reshaping of astrophysics with important evolutionary and cosmological consequences. These are too broad to discuss in this work. The issue at hand is simply the assignment of the proper state of matter for the Sun.

5.4 The birth of a star

Current stellar evolution theory holds that the stars are initially formed as a result of the free fall gravitational collapse of interstellar clouds [3]. A significant weakness of these models is the need for a disturbance initiating the collapse [3]. It is also difficult to conceive how many stars can form from a single cloud in such models. Nonetheless, as the collapse proceeds, the process rapidly accelerates until a quasi-steady state is reached with the ignition of nuclear reactions [3].

Relative to the formation of a liquid plasma Sun, it may be important to reconsider this question. What if stellar formation is initiated not by gravitational collapse, but rather by the slow condensation and growth of a star? Star formation would be initiated in extremely cold matter, wherein two atoms first make van der Waals contact [28]. Given the low temperatures, if their combined kinetic energy is not sufficient to overcome the force associated with the van der Waals attraction, a two-atom system is created. A third atom would then join the first two and so on, until a larger and larger mass is created.

The latent heat of condensation could be dissipated by radiative emission. Initially, of course, such seeds of stellar formation would be very subject to destruction, because a high energy atom could always come and break up the process. However, a mass could grow large enough that its van der Waals forces, and its energy of cohesion, are sufficient to deal with the kinetic energy of any single noncondensed atom. When this occurs, condensation would increase rapidly. Again, the important interaction is the van der Waals force. Eventually, a large body could be formed and gravitational forces would become important. The stellar mass would continue to grow. Hydrogen would be converted to a liquid metal plasma, when a critical value for the mass and pressure is achieved. This would correspond to a mass on the order of the Jovian planets (since they are currently theorized to be liquid metal plasmas [60]). As the forces of gravity begin to dominate, the mass of the star would grow until the internal pressure and temperatures become

high enough to provoke nuclear ignition and the birth of a new star.

A significant advantage of this approach is that stellar formation takes place at low temperatures. Cold hydrogen is permitted to condense and ignition occurs only once a given stellar mass is reached.

6 Conclusions

For over one hundred years now, the gaseous model of the Sun has dominated scientific thought in solar research. Yet, the model is complex and not easily supported by scientific experimentation. Sufficient evidence is presented herein that the Sun is truly a liquid plasma. In contrast, not a single reason can be provided supporting the idea that the Sun is a gas. The argument made in advance textbooks and coursework simply rests on the observation that the Sun is “hot”. The assumption then follows that it cannot be a liquid. Such arguments completely ignore the nature of liquids and gases.

Simple extensions of the Clausius-Clapeyron equation, neglect fact that the Sun is not in a closed system. Furthermore, the gaseous model ignores the existence of liquid metallic hydrogen plasmas in the laboratory.

In reality, we have very little understanding of the pressures and temperatures associated with the Sun. As a result, the “proofs of the gaseous model” tend to be mathematical and theoretical, not experimental. That is because of the mathematical simplicity and elegance of the current equations of state [1–3]. However, as Michelson reminds us: “Everything depends on the insight with which ideas are handled before they reach the mathematical stage [32].”

It is not prudent to apply gaseous equations of state to the Sun, without allowing for experimental guidance. Current solutions relative to solar collapse, temperature, density, internal radiative emission, photon shifting, and seismology, are significant issues for which little more than theoretical arguments are advanced. In addition, all the gaseous models ignore that atoms have size. The possibility that the condensed state needs to be considered is being ignored, precisely because van der Waals’ contributions to physical phenomena have been dismissed. Real gases are not infinitely compressible. Yet, the Sun is being described as an ideal gas in many solar models, despite the fact that the ideal gas law from the onset violates van der Waals’ findings. Furthermore, the gaseous model is counter to many experimental results in the laboratory, relative to the thermal and physical behavior of gases. Unfortunately, no alternative model currently exists as a point of discussion.

In contrast to the gaseous model of the Sun, the hot liquid plasma model is extremely simple; requiring no theoretical arguments beyond those provided by the liquid state itself, even in the area of energy partition. The hot liquid plasma model addresses the problems of solar collapse and seismology with simplicity. It reconciles the violation of the 2nd

law of thermodynamics and the heating of the corona, by invoking the simple release of stored energy from the convection currents of the photosphere. It dismisses extreme densities with hydrogen and helium, by having recourse to the incompressibility of the liquid state. The liquid model eliminates radiative heat transfer as a means of striving for internal thermal equilibrium, as contrary to established thermodynamic principles. Internal thermal equilibrium within the Sun must be achieved using convection and conduction, as is the case for every other object.

The liquid plasma model also provides an alternative explanation for “photon shifting”. The visible light of the photosphere is simply produced instantly as a direct manifestation of the vibrational energy contained within the liquid lattice of the solar surface. The problem of calculating internal solar opacities, which must be continually adjusted for frequency and temperature, is removed. Rather, it is argued that not a single photon is being produced within the Sun. Radiative emission remains a surface phenomenon for the Sun, as it is for every other object known to man.

As with any new model, it is clear that a great deal of effort will be required to place each solar finding in the context of a liquid framework. The gaseous equations of state had provided a mathematically elegant approach to stellar structure. In the liquid plasma model, the equations associated with magnetohydrodynamics move to the forefront. This implies that, rather than concentrate on pressure and density, we must turn our attention to thermal conductivity and viscosity. This is far from being a simple problem. Pressure and density changes can be relatively easily addressed, in the liquid plasma model, based on known rigid body solutions [58]. However, the determination of solar conductivities and viscosities poses a daunting task for plasma physics. This is especially true since thermal conductivities and viscosities are often viewed as second and fourth-order tensors, respectively.

Nonetheless, the plasma physicist may eventually gain a better understanding of these quantities as related to stellar interiors, particularly as our efforts are focused on the nature and properties of liquid metallic hydrogen.

It is certainly true that the reevaluation of stellar structure will be difficult. As the same time, the introduction of the liquid plasma model brings new and exciting dimensions in our quest to characterize the physics associated with the Sun. Prudence dictates that we consider every possibility, as we continue to explore this still mystical object in our sky.

Dedication: This work is dedicated to the memory of Jacqueline Alice Roy.

References

1. Chandrasekhar S. An introduction to the study of stellar interiors. New York, Dover Publications, 1957.
2. Clayton D. D. Principles of stellar evolution and nucleosynthesis. New York, McGraw-Hill Book Company, 1968.
3. Kippenhahn R. and Weigert A. Stellar structure and evolution. 3rd ed., Berlin, Springer-Verlag, 1994.
4. Stix M. The Sun: an introduction. Berlin, Springer-Verlag, 1989.
5. Zirin H. Astrophysics of the Sun. Cambridge, Cambridge University Press, 1988.
6. Lane L. H. On the theoretical temperature of the Sun, under the hypothesis of a gaseous mass maintaining its volume by its internal heat, and depending on the laws of gases as known to terrestrial experiments. *Am. J. Sci. Arts*, 1870, Ser. 2, v. 50, 57–74.
7. Eddington A. S. The internal constitution of the stars. New York, Dover Publications, 1959.
8. Eddington A. S. Stars and atoms. New Haven, Yale University Press, 1927.
9. Landsberg P. T. Thermodynamics with quantum statistical illustrations. New York, Interscience, 1961, 250–291.
10. Robitaille P. M. L. On the validity of Kirchhoff's law of thermal emission. *IEEE Trans. Plasma Science*, 2003, v. 31(6), 1263–1267.
11. Stefan J. Ueber die Beziehung zwischen der Wärmestrahlung und der Temperatur. *Sitzungsberichte der mathematisch-naturwissenschaftlichen Classe der kaiserlichen Akademie der Wissenschaften*, Wien 1879, v. 79, 391–428.
12. Wien W. Ueber die Energieverteilung in Emissionspektrum eines schwarzen Körpers. *Ann. Phys.*, 1896, v. 58, 662–669.
13. Planck M. Ueber das Gesetz der energieverteilung in Normalspectrum. *Annalen der Physik*, 1901, v. 4, 553–563.
14. Livingston W. and Koutchmy S. Eclipse science results: past and present. *ASP Conference Series*, 2000, v. 205, 3–10.
15. Gough D. O. Seismology of the Sun and the distant stars. Dordrecht, D. Reidel Publishing Company, 1986.
16. Bahcall J. N., Pinsonneault M. H. and Basu S. Solar models: current epoch and time dependences, neutrinos, and helioseismological properties. *Astrophys. J.*, 2001, v. 555, 990–1012.
17. Knudsen J. G., Hottel H. C., Sarofim A. F., Wankat P. C. and Knaebel K. S. Heat transmission. In: *Perry's Chemical Engineers' Handbook*, 7th ed., New York, The McGraw-Hill Book Company, 1997, 5:23–42.
18. Touloukian Y. S. and Ho C. Y. Thermophysical properties of matter. New York, Plenum, v. 1–8, 1970.
19. Chapman A. J. Heat transfer. New York, The Macmillan Company, 1967, 413.
20. Siegel R. and Howell J. Thermal radiation heat transfer. 4th ed., New York, Taylor and Francis, 2002.
21. Peraiah A. An introduction to radiative transfer. Cambridge, Cambridge University Press, 2002.
22. Rybicki G. B. and Lightman A. P. Radiative processes in astrophysics. New York, John Wiley and Sons, 1979.
23. Shu F. H. The physics of astrophysics: radiation. Mill Valley (CA), University Science Books, 1991.

24. Rogers F. J., Swenson F. J. and Iglesias C. A. OPAL equation-of-state tables for astrophysical applications. *Astrophys. J.*, 1996, v. 456, 902–908.
25. Saumon D., Chabrier G. and Van Horn H. M. An equation of state for low-mass stars and giant planets. *Astrophys. J. Suppl. Ser.*, 1995, v. 99, 713–741.
26. Gray D. F. The observation and analysis of stellar photospheres. 2nd ed., Cambridge, Cambridge University Press, 1992, 124.
27. Cortes T. R. and Sanchez F. The structure of the Sun. Cambridge, Cambridge University Press, 1996.
28. Atkins P. W. Physical chemistry. New York, W. H. Freeman and Company, 1990, 668–671.
29. Croxton C. A. Progress in liquid physics. Chichester (UK), John Wiley & Sons, 1978, 1–592.
30. March N. H. and Tosi M. P. Introduction to liquid state physics. New Jersey, World Scientific, 2002.
31. Mortimer R. G. Physical chemistry. New York, Harcourt Academic Press, 2000, 25–26.
32. Michelson I. The science of fluids. Van Nostrand Reinhold Company, 1970.
33. Ulaby F. T., Moore R. K. and Fung A. K. Microwave remote sensing active and passive: radar remote sensing and surface scattering and emission theory. Vol. 2, London, Addison-Wesley Publishing Company, 1982, 880–884.
34. Srivastava G. P. The physics of phonons. New York, Adam Hilger, 1990, 360–370.
35. Bruesch P. Phonons: theory and experiments. New York, Springer-Verlag, 1982, 167–199.
36. Kittel C. Introduction to solid state physics. New York, John Wiley and Sons, 1986, 83–124.
37. Palmer D. W., Thompson M. W. and Townsend P. D. Atomic collision phenomena in solids. Amsterdam, North-Holland Publishing Company, 1970.
38. Reissland J. A. The physics of phonons. London, John Wiley and Sons, 1973.
39. Planck M. The theory of heat radiation. Philadelphia, P. Blakiston's Sons & Co., 1914.
40. Fleck B., Brekke P., Haugan S., Duarte L. S., Domingo V., Gurman J. B. and Poland A. I. Four years of SOHO discoveries – Some Highlights. *ESA Bulletin*, 2000, v. 102, 68–86.
41. Langley S. P. Experimental determination of wave-lengths in the invisible spectrum. *Mem. Natl. Acad. Sci.*, 1883, v. 2, 147–162.
42. Langley S. P. On hitherto unrecognized wave-lengths. *Phil. Mag.*, 1886, v. 22, 149–173.
43. Kirchhoff G. Ueber den Zusammenhang von Emission und Absorption von Licht und Wärme. *Monatsberichte der Akademie der Wissenschaften zu Berlin*, 1860, Sessions of Dec. 1859, 783–787.
44. Kirchhoff G. Ueber das Verhältnis zwischen dem Emissionsvermögen und dem absorptionsvermögen der Körper für Wärme und Licht. *Annalen der Physik*, 1860, v. 109, 275–301.
45. Boulos M. I., Fauchais P. and Pfender E. Thermal plasmas: fundamentals and applications. New York, Plenum Press, 1994, 377.
46. Penner S. S. Quantitative molecular spectroscopy and gas emissivities. Reading (MA), Addison-Wesley Publ. Co., 1959.
47. Fowler J. B. A third generation water bath based blackbody source. *J. Res. Natl. Inst. Stand. Technol.*, 1995, v. 100, 591–599.
48. Fowler J. B. An oil-based 293 K to 473 K blackbody source. *J. Res. Natl. Inst. Stand. Technol.*, 1996, v. 101, 629–637.
49. Murphy A. V., Tsai B. K. and Saunders R. D. Comparative calibration of heat flux sensors in two blackbody facilities. *J. Res. Natl. Inst. Stand. Technol.*, 1999, v. 104, 487–494.
50. Murphy A. V., Tsai B. K. and Saunders R. D. Transfer calibration validation tests on a heat flux sensor in the 51 mm high-temperature blackbody. *J. Res. Natl. Inst. Stand. Technol.*, 2001, v. 106, 823–831.
51. Navarro M., Bruce S. S., Johnson B. C., Murphy A. V. and Saunders R. D. Vacuum processing technique for development of primary standard blackbodies. *J. Res. Natl. Inst. Stand. Technol.*, 1999, v. 104, 253–259.
52. Burchell T. D. Thermal properties and nuclear energy applications. In: *Graphite and Its Precursors*, Sydney, Australia, Gordon and Breach Science Publishers, 2001, 87–110.
53. Roberts A. M. Solar faculae stand exposed. *Sky and Telescope*, 2003, v. 106(4), 26.
54. Scharmer G. B., Gudiksen B. V., Kiselman D., Lfdahl M. G., Rouppe van der Voort L. H. M. Dark cores in sunspot pernumbral filaments. *Nature*, 2002, v. 420, 151–153.
55. Kosovichev A. G. and Zharkova V. V. X-ray flare sparks quake inside the Sun. *Nature*, 1998, v. 393, 28.
56. Dicke R. H. and Goldenberg H. M. Solar oblateness and General Relativity. *Phys. Rev. Lett.*, 1967, v. 18(9), 313–316.
57. Godier S. and Rozelot J. P. The solar oblateness and its relationship with the structure of the tacholine and the Sun's subsurface. *Astron. & Astrophys.*, 2000, v. 355, 365–374.
58. Littleton R. A. The stability of rotating liquid masses. Cambridge, Cambridge University Press, 1953.
59. Domiciana de Souza A., Kervella P., Jankov S., Abe L., Vakili F., diFolco E. and Paresce F. The spinning-top be star achernar from VLTI-VINCI. *Astron. & Astrophys.*, 2003, v. 407, L47–L50.
60. Weir S. T., Mitchell A. C and Nellis W. J. Metallization of fluid molecular hydrogen at 140 Gpa (1.4 Mbar). *Phys. Rev. Lett.*, 1996, v. 76, 1860–1863.
61. Collins G. W., DaSilva L. B., Celliers P., Gold D. M., Foord M. E., Wallace R. G., Ng A., Weber S. V., Budil K. S. and Cauble R. Measurements of the equation of state of deuterium at the fluid-insulator-metal transition. *Science*, 1998, v. 281, 1178–1181.
62. Woods L. C. Principles of magnetoplasma dynamics. Oxford, Clarendon Press, 1987.
63. Kowalenko N. P. and Krasny Y. P. Theory of equilibrium and kinetic properties of liquid metal. In: *Transport Properties in Dense Plasmas*, Basel, Birkhauser Verlag, 1984, 127–155.

Progress in Physics is a quarterly issue scientific journal, registered with the Library of Congress (DC).

This is a journal for scientific publications on advanced studies in theoretical and experimental physics, including related themes from mathematics.

Electronic version of this journal:
<http://www.ptep-online.com>

Editor in Chief

Dmitri Rabounski  rabounski@ptep-online.com

Associate Editors

Florentin Smarandache	 smarandache@ptep-online.com
Larissa Borissova	 borissova@ptep-online.com
Stephen J. Crothers	 crothers@ptep-online.com

Progress in Physics is peer reviewed and included in the abstracting and indexing coverage of: Mathematical Reviews and MathSciNet of AMS (USA), DOAJ of Lund University (Sweden), Zentralblatt MATH (Germany), Referativnyi Zhurnal VINITI (Russia), etc.

Department of Mathematics, University of New Mexico,
200 College Road, Gallup, NM 87301, USA

Printed in the United States of America

Issue 2007, Volume 1
US \$ 20.00

